Title
Investigating Gas Migration in Enzymes: Dioxygen Channels inside of Soybean Lipoxygenase 1

Author
Collazo, Lara Patricia

Publication Date
2013

Peer reviewed|Thesis/dissertation

Investigating Gas Migration in Enzymes: Dioxygen Channels inside of Soybean Lipoxygenase 1

By

Lara Patricia Collazo

A dissertation submitted in partial satisfaction of the

requirements for the degree of

Doctor of Philosophy

in

Molecular and Cell Biology

in the

Graduate Division

of the

University of California, Berkeley

Committee in charge:

Professor Judith P. Klinman, Chair
Professor Tom Alber
Professor Christopher J. Chang
Professor Michelle C. Chang

Spring 2013

Abstract

Investigating Gas Migration in Enzymes:
Dioxygen Channels inside of Soybean Lipoxygenase 1

by

Lara Patricia Collazo

Doctor of Philosophy in Molecular and Cell Biology

University of California, Berkeley

Professor Judith P. Klinman, Chair

Enzymes are complex systems that contain a variety of pockets, clefts, and channels throughout the protein matrix. These gaps and tunnels represent potential transport pathways for gases, ions, and other small molecules, and can play a critical role in tuning enzyme function. In this work, the functional role of gas migration pathways was examined in soybean lipoxygenase 1 (SLO-1), a prototypical lipoxygenase that catalyzes the regio- and stereospecific peroxidation of linoleic acid to 13S hydroperoxyoctadecadienoic acid (13S HPOD). Two computational techniques—implicit ligand sampling and CAVER—were employed to evaluate pathways for oxygen migration in the enzyme. Both approaches converged on a single channel deemed most competent for oxygen delivery. Interestingly, this channel is consistent with a cavity originally detected in the crystal structure of SLO-1 and previously proposed as a pathway for oxygen. Site-directed mutagenesis was used to assess the impact of introducing bulk at the channel's bottleneck residues. Introducing tryptophan into the pathway at positions 553 and 496 resulted in increased Michaelis constants for oxygen and disrupted reaction regio- and stereospecificity, supporting a functional role for the tunnel in oxygen trafficking. Intriguingly, mutations at Ile^{553} and Leu^{496} appear to influence oxygen migration in distinct ways. Introducing tryptophan at 553 dramatically reduces O_2 access to the active site, as evidenced by a markedly increased $K_M(O_2)$—744 μM O_2 compared to 38 μM O_2 for wild-type—together with an increase in the proportion of 13R, 9S, and 9R HPOD isomers generated. Introducing bulk at 496, by contrast, appears to ungate an alternate pathway for O_2 access, as evidenced by an increased proportion of 9S and 9R HPOD isomers generated. The divergent behavior of the Ile553Trp and Leu496Trp mutants provides striking evidence for the plasticity of oxygen pathways, which can be manipulated via single site mutations. Taken together, our computational and mutagenesis studies point to a single delivery channel that shuttles oxygen to the active site of SLO-1 and tunes the regio- and stereospecificity of oxygen insertion into linoleic acid. Our results speak to the vital role that the protein matrix plays in regulating catalysis and lay the framework for future protein engineering efforts in oxygen-dependent enzymes.

Table of Contents

Acknowledgements

I would like to thank my advisor, Judith Klinman, for her support during my thesis work. Her excitement about research and drive to learn more about enzyme function continues to amaze and impress me. I am grateful to have worked with such a passionate and visionary mentor. I would also like to recognize my committee members—Tom Alber, Chris Chang, and Michelle Chang—for asking insightful questions, challenging my assumptions, and providing valuable feedback during each committee meeting.

Thanks to my lab mates for their help over the past six years (e.g. opening bottles, reaching reagents on the top shelf, troubleshooting experiments, and interpreting data). Zac Nagel, Kevin McCusker, Sam Shen, Jianyu Zhang, Jerome Cattin, Shenshen Hu, and Hui Zhu, you have been kind enough to answer my many questions and it has been a pleasure working with you.

I would also like to thank my wonderful collaborators, who played an essential role in bringing this work to fruition and were very generous with their time and patience. Kathy Durkin, Tony Iavarone, Chris Canlas and Jeff Pelton, your substantial contributions to this project are greatly appreciated.

Thank you to Florence Bonnot, for reminding me to focus on the big picture. To Sudhir Sharma, for teaching me to stay calm, be methodical and not take any experiment for granted. To Marcus Carr, for making everything better by commiserating and providing trail mix. To Erin Imsand, for trips to Bizarro Peet's, pho lunches, and (plentiful) heart to hearts in the electrode room. To Albert Lang, for cobbler delivery, tête-à-têtes in the stairwell, excellent advice, and so many laughs. To Elena Bekerman, for making graduate school twenty times as fun and co-founding the SFS. To Brandon Bunker, for simultaneously distracting me from and helping me in lab—this thesis would not be what it is without Thai teas and your rotovapping. To Rock, for setting an example of work-life balance.

I would like to thank my parents and brothers for providing perspective and unconditional support. Finally, I want to recognize my grandparents who had so much faith in me that they began prematurely calling me 'doctor' years ago. I love you!

Dedication

Para mi mamá.

“I don't know—maybe the world has two different kinds of people, and for one kind the world is this completely logical, rice pudding place, and for the other it's all hit-or-miss macaroni gratin.”

Haruki Murakami, *The Wind-Up Bird Chronicle*

Chapter 1

Introduction

1.1 Soybean Lipoxygenase 1

Introduction

Oxygenase and oxidase chemistry is common in aerobic cells, making access of oxygen to enzyme active sites critical. Previously it had been believed that gases diffuse unhindered throughout the protein matrix thanks to its inherent breathing and flexibility; channels were thought to be exclusively for substrate use. (*1*) Such a diffusion-based model presents immediate challenges for oxygen-dependent enzymes. If oxygen is randomly distributed within proteins, how is its insertion subject to regio- and stereocontrol during active site chemistry—as in lipoxygenases, for example?

Lipoxygenases (LOXs) catalyze the regio- and stereoselective insertion of dioxygen into achiral polyunsaturated fatty acids to yield chiral hydroperoxides. Although a putatively delocalized carbon radical is formed during catalysis, its reaction with dioxygen occurs with immaculate regio- and stereospecificity. (*2*) Lipoxygenases are an excellent system in which to examine oxygen migration because product positional and stereochemistry can report on oxygen targeting to the active site. Furthermore, the hydroperoxy products of mammalian lipoxygenases are both physiologically and medically relevant. Many serve as precursors for signaling molecules involved in cellular homeostasis, differentiation, and proliferation. Aberrant LOX activity is implicated in anaphylaxis, inflammation, and atherosclerosis; inhibitors of mammalian 5-LOXs are currently being prescribed as anti-asthmatic drugs. (*2*, *3*)

Soybean lipoxygenase 1 (SLO-1) is a prototypical non-heme iron-containing lipoxygenase that displays high sequence identity with all mammalian LOXs. (*4*) SLO-1 also displays the regio- and stereospecificity characteristic of LOXs when it converts linoleic acid to 13S-hydroperoxyoctadecadienoic acid (13S HPOD). By contrast, the analogous autoxidation yields a mixture of 13S, 13R, 9S, and 9R HPOD. The availability of two high-resolution x-ray crystal structures and a high-yield bacterial expression and purification system further recommend SLO-1 as a suitable model for LOX study. (*5*-*7*) Paralleling their mammalian counterparts, plant LOX pathway products are involved in immunity, growth, regulation, and germination. Some products, including jasmonic acid, are volatile and can play a role in inter-plant signaling. (*8*)

Catalytic Mechanism of SLO-1

A simplified scheme for the SLO-1-catalyzed reaction is depicted in **Scheme 1-1**. The reaction occurs in three chemical steps. The first is hydrogen atom abstraction from the bis-allylic methylene of linoleic acid by the active site Fe^{3+}-OH; this rate-limiting step yields Fe^{2+}-OH_2 and a carbon-based linoleyl radical. The linoleyl radical then reacts rapidly with oxygen to yield a 13S peroxyl radical. Finally, the peroxyl radical is reduced, generating 13S HPOD and re-generating the active site Fe^{3+}-OH. (*7*) Based on autoxidation chemistry, there is effectively no energy barrier for the formation of a peroxyl radical by oxygen insertion into the linoleyl pentadienyl radical. (*9*) Consequently, a targeted mechanism for oxygen delivery seems necessary to ensure regio- and stereospecificity. Without such a mechanism, dioxygen would likely attack non-specifically at multiple carbons and faces of the linoleic acid radical intermediate—leading to loss of stereocontrol and production of 13R, 9R, and 9S HPOD (also depicted in **Scheme 1-1**) in addition to the 13S isomer.

Regio- and Stereospecificity of SLO-1 Reaction

At least three theories that are distinct from gas channeling have been proposed to explain LOX product regio- and stereospecificity. In the first, LOX distorts the substrate structure so that the radical cannot be delocalized over the 5 pentadienyl carbons. The radical character and resulting oxygen reactivity are focused on a single carbon. This mechanism, however, would demand a large energy input and significant protein movement during catalysis for which there is no evidence. A second hypothesis proposes peroxyl radical trapping and assumes reversible addition of oxygen to the linoleyl radical at multiple carbons. Stereocontrol is achieved because the enzyme chooses a single peroxyl radical to reduce into product. Given the stability of conjugated peroxyls and SLO-1's 3 millisecond catalytic cycle, however, it is unlikely that multiple on-off cycles can occur before product formation. (*2*) A third hypothesis proposes that SLO-1 actively binds oxygen in order to control substrate oxidation like P450 monooxygenases. P450s bind oxygen using a heme iron and present an activated ferryl oxygen to bound substrate. (*10*) There is no direct evidence for Fe-O_2 or Fe-OOH species in SLO-1, however, making such a mechanism of stereocontrol unlikely. (*2*) The alternate theories described cannot definitively explain how SLO-1 achieves regio- and stereospecificity. This work investigates the hypothesis that a gas channel within SLO-1 shuttles oxygen to the active site, thereby ensuring its targeted insertion into linoleic acid.

1.2 Intra-enzyme Gas Migration

Introduction

Early work on gas channeling within proteins was performed with myoglobin using techniques that include time-resolved x-ray crystallography, molecular dynamics simulations, and spectroscopy of the geminate recombination process. (*11*) Although these experiments certainly pointed to the existence of gas binding pockets, conclusive identification of specific dioxygen channels within proteins has remained a challenge. X-ray crystallography, in particular, has struggled to detect oxygen pathways since dioxygen is rarely able to generate a robust signal in electron-density difference maps. (*12*) How then can the gas permeability of proteins be demystified?

A synergistic multi-technique and multi-enzyme approach has recently been employed in many laboratories. Significant evidence has been collected using a creative combination of noble gas pressurization, implicit ligand sampling, explicit gas diffusion simulations, and site-directed mutagenesis. The application of these techniques to enzymes with diverse functional roles in different species has been key in assessing the ubiquity of gas channels. Investigated proteins include photosystem II, lipoxygenases, hydrogenases, copper-containing amine oxidases, heme-copper oxidases, and, of course, the globins. Gradually, a model for gas migration within proteins has emerged. It seems probable that dioxygen neither diffuses freely throughout the protein matrix nor travels through a single, rigid and permanent tube of empty space toward the buried site of catalysis. In reality, the gas seems to be accessing a network of transient hydrophobic pathways that form and disappear as a function of the protein's thermal fluctuations. (*13*)

While a variety of techniques have contributed to our current understanding of gas migration within enzymes, the following discussion will focus on three—noble gas pressurization, implicit ligand sampling, and site-directed mutagenesis.

Noble Gas Pressurization

The location of gas migration pathways in enzymes can rarely be inferred by locating oxygen in crystal structures. This is because oxygen's low electron density makes it challenging to detect by x-rays. Consequently, experimentalists often perform x-ray crystallography on proteins pressurized with dioxygen mimics like xenon or krypton. With Van der Waals diameters of 4.3 and 4.0 angstroms respectively, xenon and krypton match the dioxygen bond length of 4.2 angstroms. Like dioxygen, both of these noble gases also prefer hydrophobic environments and populate the cavities created by packing defects in the interiors of folded proteins. The advantage conferred by the noble gases is an increased electron density that is more amenable to x-ray crystallography. Xenon is actually more frequently employed, as krypton displays a slightly reduced affinity and decreased binding. Importantly, no movements of the side chains or peptide backbone are typically detected upon noble gas binding in difference fourier maps following rigid-body refinement. This suggests that xenon-pressurized and native protein crystals are isomorphous, and therefore, that dioxygen channels so discovered are physiologically relevant. (*14*)

Some of the most informative x-ray crystallographic work with xenon-pressurized crystals involves an overlay of the xenon binding sites in copper amine oxidases (CAOs) from *Hansenula polymorpha (HPAO), Arthrobacter globiformis (AGAO), Pichia pastoris (PPLO),* and *Pisum sativum (PSAO),* pictured in **Figure 1-1**. One can visualize a chain of non-coincident Xe atoms revealing a pathway lined by hydrophobic and bulky amino acid residues. The mobility and flexibility of such side chains lend themselves to dynamic packing defects that could permit dioxygen to pass. The overlay strongly supports oxygen entry on either side of the catalytic beta sandwich and subsequent passage to the active site. CAO sequence conservation in the channel region was typical of any protein hydrophobic interior, suggesting that the beta sandwich is not unique in its capacity for directed dioxygen migration. (*13*)

Based on crystal structures, dioxygen channels have also been postulated for several proteins within the heme-copper oxidase superfamily—bovine heart*, Paracoccus denitrificans (Pd), Rhodobacter sphaeroides (Rs),* and *Thermus thermophilus (Tt)* cytochrome c oxidases as well as *Escherichia coli (Ec)* quinol oxidase bo_3. Xenon-pressurized crystal structures, however, only exist for those of *Tt* and *Rs*. In the latter, two Xe binding sites are observed, consistent with a putative dioxygen channel but not definitively outlining one. In the case of *Tt*, by contrast, a continuous forked channel is defined by 7 adjacent xenon atoms without room for intervening sites. The pathway converges from two entry points on the protein surface before leading dioxygen into the dinuclear catalytic center. Hydrophobic amino acid side chains along the channel are all within van der Waals contact of the bound xenons with no preference between aliphatic or aromatic residues. (*14*)

Xenon-pressurized crystallography has provided similarly promising evidence for hydrophobic gas channels in myoglobin, methane mono-oxygenase hydroxylase, acetyl-CoA synthase, and carbon monoxide dehydrogenase. This structural technique is a robust tool for examining gas migration within proteins. (*15*)

Implicit Ligand Sampling

Like xenon-pressurized x-ray crystallography, implicit ligand sampling (ILS) enables the identification of pockets of oxygen favorability within proteins. A novel computational method, this technique is remarkable because it does not attempt to resolve static channels but instead identifies dynamic pathways that are a function of the thermal fluctuations of the protein. ILS makes the powerful assumption that, because gas-protein interactions are weak, gas channels appear and disappear independently of the gas ligand itself. Thus, by analyzing protein dynamics in the absence of any gas ligand, ILS can sample protein migration pathways at every point in space simultaneously. (*16*) With this approach, better statistics can be generated than by sampling the trajectory of a hypothetical single ligand. (*11*)

The output of ILS is a "potential of mean force" (PMF) map which describes the Gibbs free energy cost ($DG_s(O_2)$) associated with transferring a gas molecule from the solvent to any position inside the protein. The lower the $DG_s(O_2)$ at a particular location, the greater the probability of finding dioxygen there. Consequently, dynamic dioxygen channels can be identified by drawing PMF isoenergy surfaces—that is, plotting all points in a protein for which the $DG_s(O_2)$ is below a certain value. These isoenergy surfaces often highlight xenon binding sites as highly favorable dioxygen binding regions. (*11*, *16*)

ILS has been performed by Cohen and co-workers on the copper amine oxidases of *Hansenula polymorpha, Arthrobacter globiformis, Pichia pastoris,* and *Pisum sativum* without contradicting previous xenon binding experiments. Indeed, the fidelity between crystallographic and ILS data is exquisitely exemplified in **Figure 1-2**, which depicts xenon binding in the ILS-favored regions of sperm whale myoglobin. (*17*) Unfortunately, the limitations of noble gas pressurization also become obvious upon inspection of ILS-generated PMF iso-surfaces. The former technique offers restricted information about single binding sites while the latter generates a full and dynamic picture of the protein.

ILS has been previously employed to detect multiple oxygen delivery pathways in rabbit 12/15-lipoxygenase. Three low energy dioxygen routes between the protein exterior and active site were identified using PMF iso-surfaces, one of which is not continuously open and thus was undetectable crystallographically. In fact, a fourth dioxygen channel opens in the presence of substrate, confirming the dynamic nature of these gas migration pathways. Within the active site itself, the iron complex and region of maximal O_2 probability were found to be on opposite sides of the fatty acid backbone—an arrangement that is consistent with the antarafacial nature of lipoxygenase catalysis. Furthermore, the O_2 favorability around C15 of the fatty acid backbone is 7-fold greater than around C11, where lipoxygenase does not insert dioxygen. Although these results should not be overinterpreted in light of the mobility and flexibility of the fatty acid itself, they do seem to partially explain the regio- and stereospecificity of lipoxygenase catalysis. Data collected for cyclooxygenase parallels these conclusions for oxygen-dependent enzymes. (*12*)

Site-directed Mutagenesis

This technique is conceptually the most straightforward to understand. The rationale involves blocking putative gas channels in an enzyme by site-specifically mutating a single amino acid residue lining the channel. Dioxygen kinetics assays are then performed to assess the degree of channel blockage and catalytic activity impairment; often the parameter analyzed is $K_M(O_2)$ which equals the $[O_2]$ at which reaction rate is half-maximal. An increased $K_M(O_2)$ reflects slower dioxygen diffusion to the enzymatic active site and supports the relevance of the putative pathway obstructed. (*18*)

Some success has been obtained by Brzezinski and co-workers using this approach on *Rs* cytochrome c oxidase. Based on a gas channel apparent in the xenon-pressurized crystal structure, a single glycine to valine mutation was introduced into the enzyme. The mutant oxidase bound both dioxygen and its inert analog CO at a rate several orders of magnitude below wild-type. (*19*) Similarly, mutation of channel-lining valine 287 to isoleucine in *Ec* cytochrome c oxidase severely impacts its quinol-oxidizing activity at low concentrations of oxygen—the mutation increases the apparent $K_M(O_2)$ by 10- to 15-fold. (*18*) Such observations provide convincing evidence against the non-specific diffusion of dioxygen through the protein matrix.

Site-directed mutagenesis, however, does not always yield as conclusive data with respect to gas migration within proteins. Not only is it difficult to assess exactly how a mutation is influencing enzyme kinetic behavior, often mutations produce no change whatsoever. In the copper amine oxidase of *Hansenula polymorpha*, for example, a leucine to phenylalanine mutation made at a xenon binding site within the enzyme's catalytic beta sandwich has no effect on dioxygen kinetics. (*13*) **Figure 1-3** displays an overlay of xenon binding sites, ILS-generated PMF iso-

surfaces, and key residues identified in sperm whale myoglobin. The residues depicted are those that, when mutated, significantly alter the migration properties of dioxygen in myoglobin. What is the correlation between the location of these residues and putative gas channels? Many of these residues—particularly those depicted in red, blue, and yellow in **Figure 1-3**—do localize to dioxygen-favorable regions. There are several residues, however, that are implicated in O_2 migration by site-directed mutagenesis but not by PMF maps and xenon binding experiments. These residues are depicted in green in **Figure 1-3**. (*11*) Thus, it is challenging to infer the importance of specific residues with respect to gas migration from mutagenesis studies alone.

1.3 Oxygen Transport Channel in SLO-1

Site-directed Mutagenesis

A dioxygen channel leading to the active site was originally identified in the x-ray crystal structure of SLO-1. (*6*) Site-directed mutagenesis studies in our laboratory have supported the functional relevance of this channel. Mutagenesis of channel-constricting residue Ile553 to phenylalanine, for example, was shown to disrupt oxygen channeling without perturbing the active site chemistry itself. Introducing the phenylalanine mutation increased the enzyme's $K_M(O_2)$ by >3-fold, while leaving k_{cat} relatively unchanged. The SLO-1 active site and putative channel are depicted in **Figure 1-4.** (*20*)

Role of O_2 in SLO-1 Activation

Additional support for oxygen channeling in SLO-1 derives from recent studies in lipoxygenase activation. These reports suggest not only that oxygen plays an important role in SLO-1 activation but also that SLO-1 may have a unique way of facilitating oxygen's access to the active site.

It is known that SLO-1 must first undergo oxidation from Fe^{2+} to Fe^{3+} in order to react with its substrate, linoleic acid; this process is described in **Part I** of **Figure 1-5**. During activation, the Fe^{2+} enzyme reacts with HPOD to generate the Fe^{3+} enzyme and a bound epoxyallylic radical. This radical subsequently reacts rapidly with O_2 to form a peroxy radical that cannot react with Fe^{3+} and quickly dissociates. The enzyme remains in its activated Fe^{3+} state and the radical is reduced in solution to yield an epoxyallylic hydroperoxide. A detailed scheme of the reaction of 13S HPOD and ferrous SLO-1 is provided in **Scheme 1-2**. (*21*, *22*)

Oxygen plays an important role in the activation process because it facilitates the dissociation of the radical. In the absence of oxygen, a fraction of the radical dissociates spontaneously, dimerizing in solution and leaving the enzyme in its activated Fe^{3+} state. However, a substantial portion of the radical also remains bound to SLO-1 and re-reduces the ferric enzyme back to its inactive state, Fe^{2+}. This process is depicted in **Part II** of **Figure 1-5**. Epoxyalcohols and ketones are produced as the Fe^{2+} enzyme is re-generated and the enzyme is said to be acting as a hydroperoxide isomerase. (*21*, *22*)

Recent studies of activation in epidermal lipoxygenase 3 (eLOX3) suggest that SLO-1 may have a specialized way of ensuring oxygen availability at the active site. eLOX3 differs from SLO-1 with respect to its reaction with HPOD by exhibiting hydroperoxide isomerase activity even at ambient oxygen. In eLOX3, the epoxyallylic radical generated by the enzyme's reaction with HPOD remains bound, re-reducing the enzyme to the Fe^{2+} state. It is thought that the radical remains bound because O_2 access to the eLOX3 active site is restricted relative to that of SLO-1. (*21*, *22*) The disparate behaviors of these two enzymes are consistent with SLO-1 having a specialized delivery channel that is responsible for ensuring oxygen's access the active site.

Conclusion

Enzymes harness the reductive power of dioxygen to drive a variety of processes in the cell. It remains unclear, however, how the diatomic non-polar gas travels to the active site of these enzymes from solvent. Random diffusion appears inconsistent with the penetration of oxygen

into deeply-buried active sites and its highly regio/stereoselective insertion into polyunsaturated fatty acids by lipoxygenases and cyclooxygenases. Instead, it has been proposed that dioxygen proceeds to the catalytic core via tunnels that prevent it from accessing the substrate indiscriminately.

This hypothesis will be tested using soybean lipoxygenase 1 (SLO-1), the best-studied model of lipoxygenase catalysis and structure. (*20*) Mutations will be introduced to disrupt a putative gas channel in SLO-1. The kinetic behavior and product distribution of these mutant enzymes will be used to assess the importance of channeling in catalysis and regio/stereocontrol. Mutagenesis will be guided and complemented by computational and structural data. Molecular dynamics simulations and implicit ligand sampling (ILS) will be performed on SLO-1 to identify favorable routes for oxygen travel.

This synergistic approach—including site-directed mutagenesis, kinetic and product distribution analysis, and computational modeling—will clarify the importance of dioxygen channeling in SLO-1 and provide valuable context for oxygen-dependent enzymes in general. Going forward, identification of gas channels may ultimately allow for the engineering of enzymes with altered gas delivery networks. In the case of hydrogenases, for example, inactivation by dioxygen limits their ability to reliably produce H_2 as a source of renewable energy. The ability to identify and obstruct dioxygen channels is consequently of immediate environmental and commercial significance. (*23*)

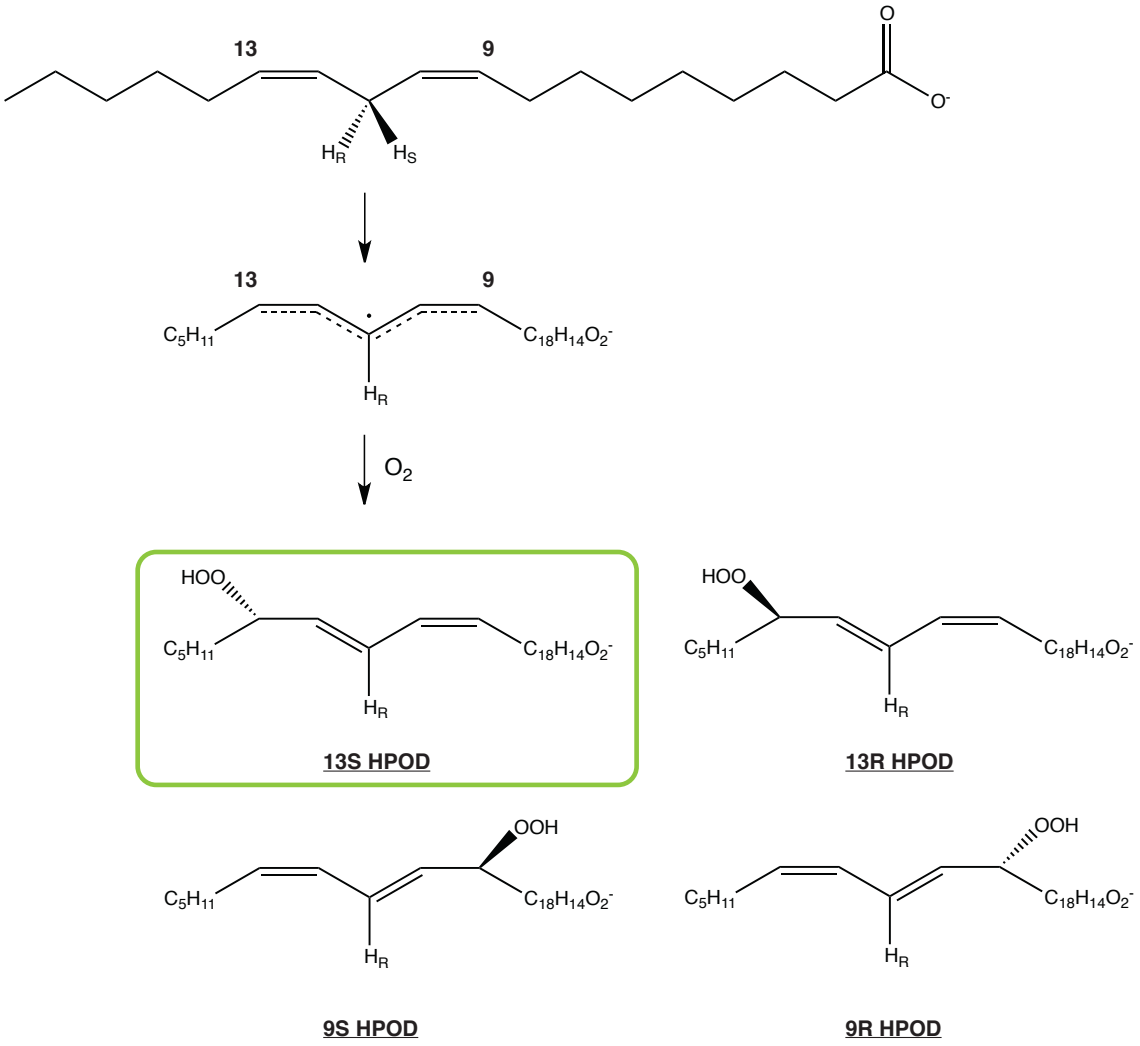

Scheme 1-1. Reaction of linoleic acid with oxygen, catalyzed by SLO-1. The enzyme-catalyzed reaction yields primarily 13S HPOD, outlined in green. The analogous reaction in solution, by contrast, yields all 4 HPOD isomers—13S, 13R, 9S, and 9R HPOD. Figure is adapted from (*20*).

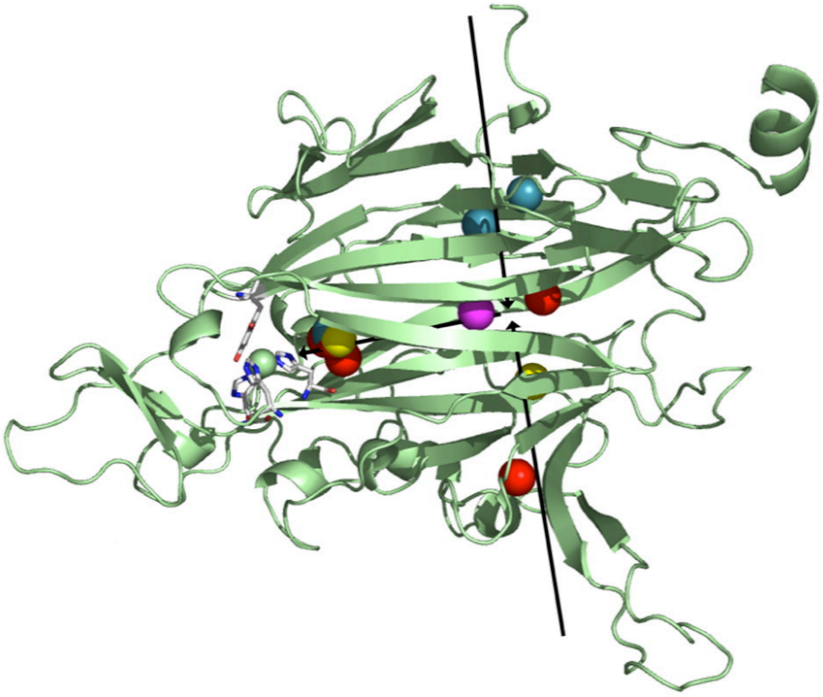

Figure 1-1. Overlay of CAO xenon binding sites with a domain of the HPAO/Xe complex. The HPAO D3 beta sandwich domain is pictured, along with CAO xenon sites deposited in the PDB. The active site is shown in stick, and the copper is shown as a green sphere. Select xenon sites in the internal D3 beta sandwich and in the neighborhood of the active site are shown. Xenon sites from individual complexes are coded by color (red, PSAO; yellow, PPLO; blue, AGAO; magenta, HPAO). Arrows indicate the direction of molecular oxygen movement to the active site using the proposed pathway. Figure is reproduced from (*13*).

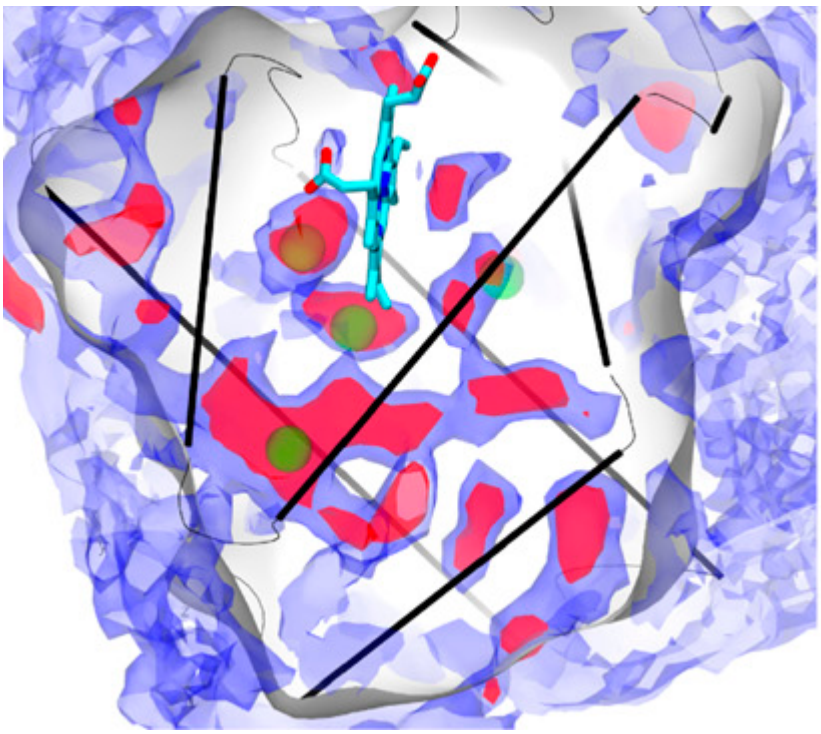

Figure 1-2. Xenon binding sites depicted with the O_2 PMF map for sperm whale myoglobin. Shown are the 0 kcal/mol (red) and 1.6 kcal/mol (blue) O_2 free energy contours. The Xe binding sites of sperm whale Mb are shown as green spheres, and the protein's alpha helices are displayed as black lines. Figure is reproduced from (*17*).

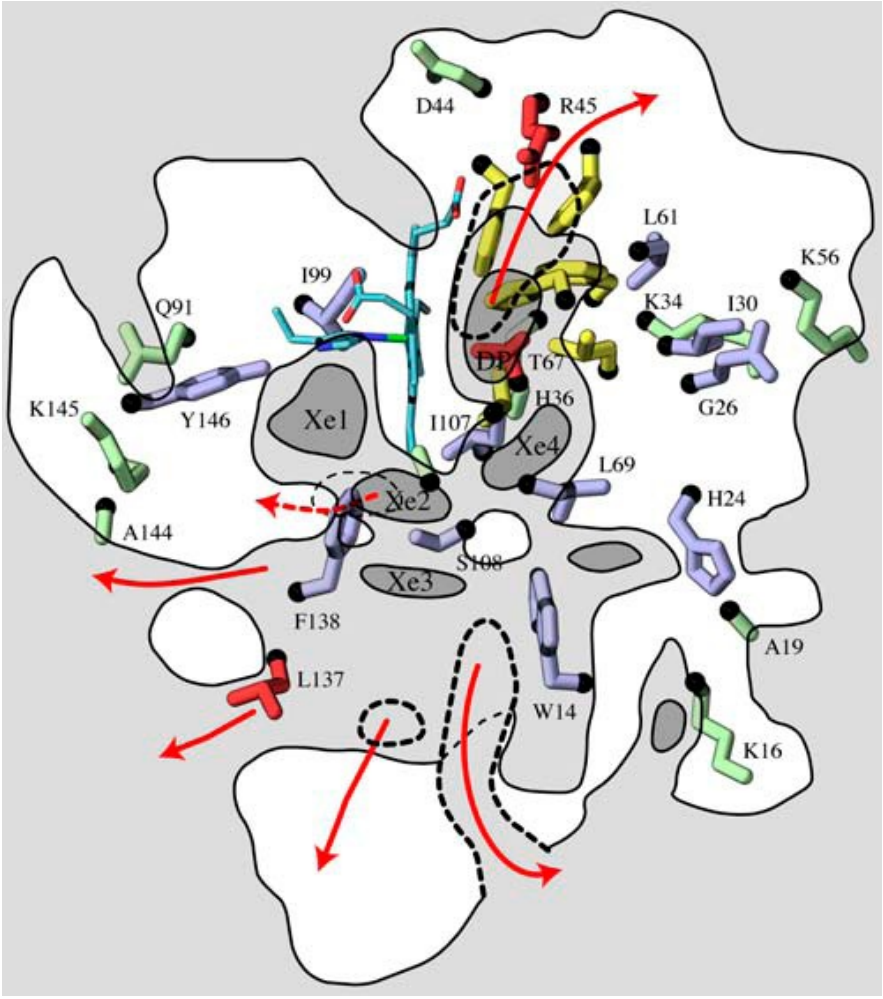

Figure 1-3. Overlay of gas migration data gathered for sperm whale myoglobin via xenon-pressurized crystallography, implicit ligand sampling, and site-directed mutagenesis. Four xenon binding pockets are depicted within the protein. Gas migration pathways identified using implicit ligand sampling are represented by the light gray (favorable) and dark gray (more favorable) regions. Red arrows represent gas exit pathways calculated from implicit ligand PMF analysis. Residues whose substitution by another amino acid significantly affects O_2 or CO migration properties during geminate rebinding in Mb are highlighted in red, blue, yellow, and green. Most residues identified experimentally—in particular, the residues in red, blue, and yellow—were also implicated by xenon binding and implicit ligand sampling analysis. For example, red residues coincide with exits from the Mb interior according to PMF maps. Blue residues include small amino acids that line a constriction between cavities and large amino acids that block passages between neighboring ligand-accessible areas. Yellow residues form the commonly recognized distal pathway that links the heme to the exterior of the protein. Residues that were shown to affect ligand migration properties upon mutation, but do not have any visible influence on gas migration according to PMF maps and xenon binding experiments, are colored in green. Figure is reproduced from (*11*).

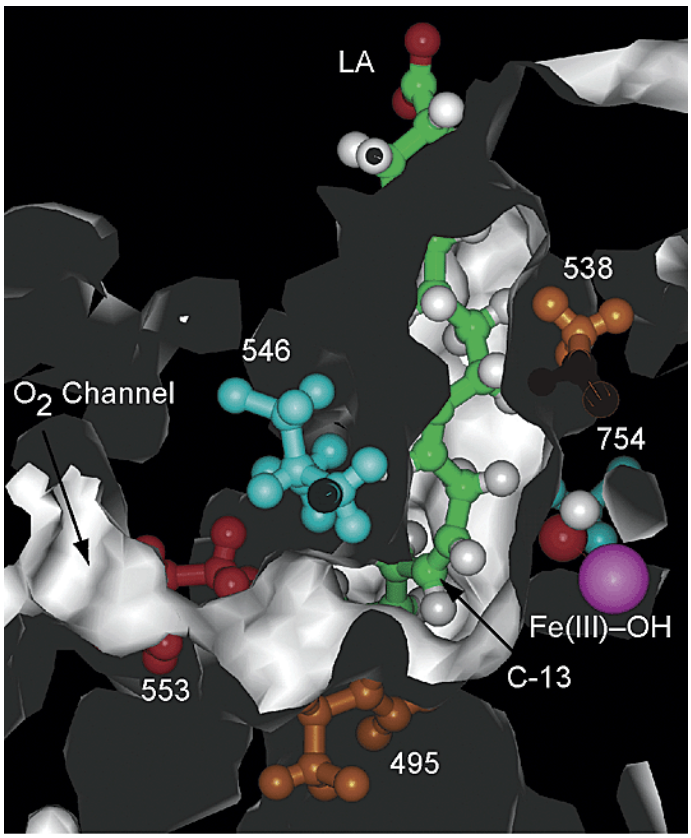

Figure 1-4. Substrate cavity and proposed O_2 access channel in SLO-1, featuring bound linoleic acid. Figure is reproduced from (*20*).

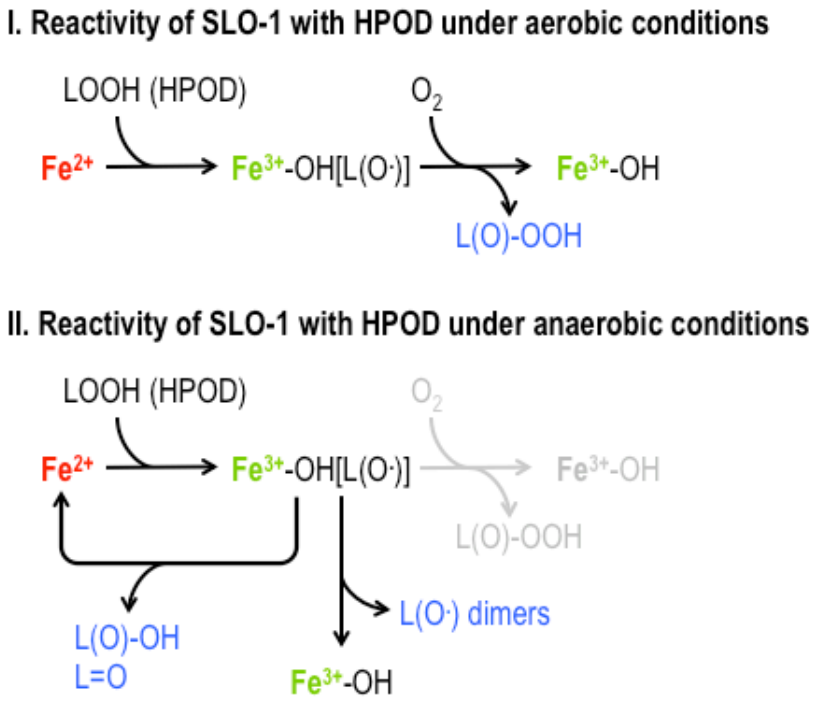

Figure 1-5. Reactivity of SLO-1 with HPOD under aerobic and anaerobic conditions. Ferrous and ferric iron ligands are depicted in red and green, respectively. Reaction products are depicted in blue. (I) Under aerobic conditions, ferrous SLO-1 is activated efficiently to ferric SLO-1. The ferrous enzyme reacts with HPOD to produce an epoxyallylic radical intermediate bound to the ferric enzyme. The radical dissociates after reacting with oxygen, forming an epoxyallylic hydroperoxide in solution and leaving the ferric enzyme activated for reaction with LA. (II) By contrast, ferrous SLO-1 is activated inefficiently under anaerobic conditions. In the absence of O_2, the epoxyallylic radical generated by the reaction of ferrous SLO-1 and HPOD participates in two distinct processes. In one, the epoxyallylic radical dissociates, dimerizing and leaving the ferric enzyme activated for reaction with LA. In the second, the epoxyallylic radical remains bound to the enzyme and re-reduces ferric SLO-1 to its inactive ferrous state. This process produces epoxyalcohols and ketones and represents the hydroperoxide isomerase reactivity of SLO-1. (*22*)

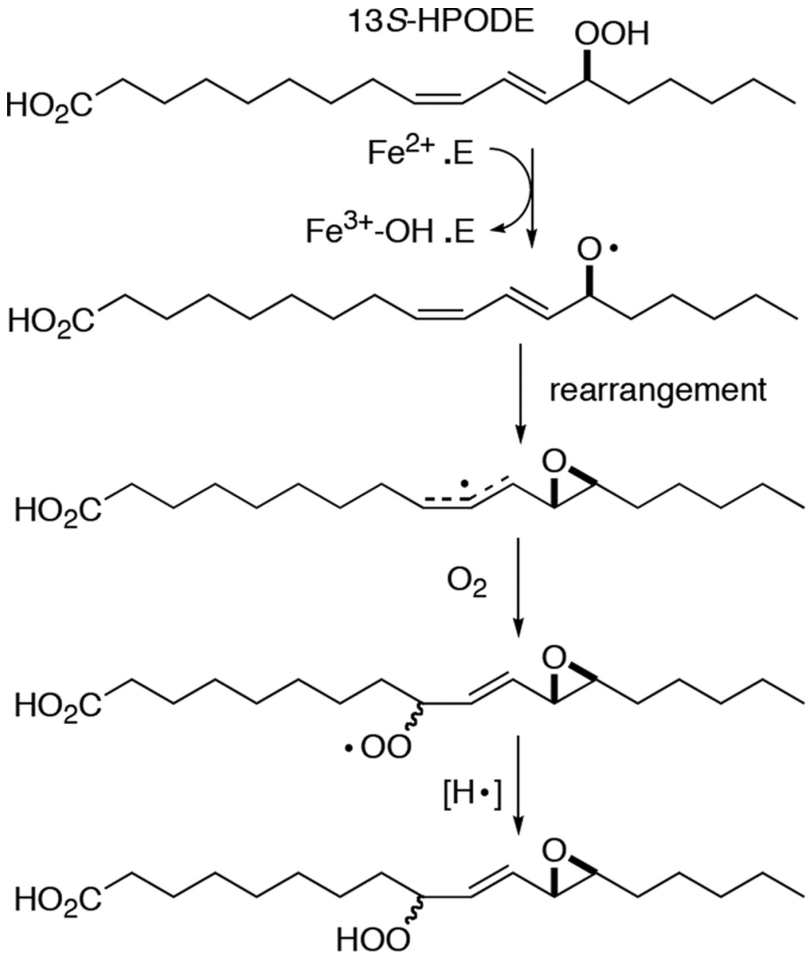

Scheme 1-2. Scheme for reaction of ferrous SLO-1 with 13S HPOD under aerobic conditions. Ferrous SLO-1 reacts with 13S HPOD to produce an epoxyallylic radical intermediate bound to the ferric enzyme. The radical dissociates after reacting with oxygen, forming an epoxyallylic hydroperoxide in solution and leaving the ferric enzyme activated for reaction with LA. Figure is reproduced from (*22*).

References

1. Calhoun, D. B., Vanderkooi, J. M., and Englander, S. W. (1983) Penetration of small molecules into proteins studied by quenching of phosphorescence and fluorescence, *Biochemistry 22*, 1533–1539.
2. Schneider, C., Pratt, D. A., Porter, N. A., and Brash, A. R. (2007) Control of Oxygenation in Lipoxygenase and Cyclooxygenase Catalysis, *Chemistry & Biology 14*, 473–488.
3. Schwarz, K. (2000) Structural Basis for Lipoxygenase Specificity: Conversion of the Human Leukocyte 5-Lipoxygenase to a 15-Lipoxygenating Enzyme Species by Site-directed Mutagenesis, *Journal of Biological Chemistry 276*, 773–779.
4. Kuhn, H., Saam, J., Eibach, S., Holzhütter, H. G., Ivanov, I., and Walther, M. (2005) Structural biology of mammalian lipoxygenases: Enzymatic consequences of targeted alterations of the protein structure, *Biochemical and Biophysical Research Communications 338*, 93–101.
5. Boyington, J. C. J., Gaffney, B. J. B., and Amzel, L. M. L. (1993) The three-dimensional structure of an arachidonic acid 15-lipoxygenase., *Science 260*, 1482–1486.
6. Minor, W., Steczko, J., Boguslaw Stec, O., Otwinowski, Z., Bolin, J. T., Walter, R., and Axelrod, B. (1996) Crystal structure of soybean lipoxygenase L-1 at 1.4 Å resolution, *Biochemistry 35*, 10687–10701.
7. Knapp, M. J., and Klinman, J. P. (2003) Kinetic Studies of Oxygen Reactivity in Soybean Lipoxygenase-1, *Biochemistry 42*, 11466–11475.
8. Tomchick, D. R., Phan, P., Cymborowski, M., Minor, W., and Holman, T. R. (2001) Structural and Functional Characterization of Second-Coordination Sphere Mutants of Soybean Lipoxygenase-1, *Biochemistry 40*, 7509–7517.
9. Porter, N. A. N., Caldwell, S. E. S., and Mills, K. A. K. (1995) Mechanisms of free radical oxidation of unsaturated lipids, *Lipids 30*, 277–290.
10. Coffa, G., Imber, A. N., Maguire, B. C., Laxmikanthan, G., Schneider, C., Gaffney, B. J., and Brash, A. R. (2005) On the relationships of substrate orientation, hydrogen abstraction, and product stereochemistry in single and double dioxygenations by soybean lipoxygenase-1 and its Ala542Gly mutant, *Journal of Biological Chemistry 280*, 38756–38766.
11. Cohen, J., Arkhipov, A., Braun, R., and Schulten, K. (2006) Imaging the Migration Pathways for O_2, CO, NO, and Xe Inside Myoglobin, *Biophysical Journal 91*, 1844–1857.
12. Saam, J., Ivanov, I., Walther, M., Holzhütter, H. G., and Kuhn, H. (2007) Molecular dioxygen enters the active site of 12/15-lipoxygenase via dynamic oxygen access channels, *Proceedings of the National Academy of Sciences 104*, 13319–13324.
13. Johnson, B. J., Cohen, J., Welford, R. W., Pearson, A. R., Schulten, K., Klinman, J. P., and Wilmot, C. M. (2007) Exploring molecular oxygen pathways in Hansenula polymorpha copper-containing amine oxidase, *Journal of Biological Chemistry 282*, 17767–17776.
14. Luna, V. M., Chen, Y., Fee, J. A., and Stout, C. D. (2008) Crystallographic studies of Xe and Kr binding within the large internal cavity of cytochrome ba3 from Thermus thermophilus: structural analysis and role of oxygen transport channels in the heme-Cu oxidases, *Biochemistry 47*, 4657–4665.
15. Duff, A. P., Trambaiolo, D. M., Cohen, A. E., Ellis, P. J., Juda, G. A., Shepard, E. M., Langley, D. B., Dooley, D. M., Freeman, H. C., and Guss, J. M. (2004) Using Xenon as a

Probe for Dioxygen-binding Sites in Copper Amine Oxidases, *Journal of Molecular Biology 344*, 599–607.

16. Cohen, J., Olsen, K. W., and Schulten, K. (2008) Finding Gas Migration Pathways in Proteins Using Implicit Ligand Sampling, *Methods in Enzymology 437*, 439–457.
17. Cohen, J., and Schulten, K. (2007) O_2 Migration Pathways Are Not Conserved across Proteins of a Similar Fold, *Biophysical Journal 93*, 3591–3600.
18. Riistama, S., Puustinen, A., García-Horsman, A., Iwata, S., Michel, H., and Wikström, M. (1996) Channelling of dioxygen into the respiratory enzyme, *Biochim. Biophys. Acta 1275*, 1–4.
19. Salomonsson, L., Lee, A., Gennis, R. B., and Brzezinski, P. (2004) A single-amino-acid lid renders a gas-tight compartment within a membrane-bound transporter, *Proceedings of the National Academy of Sciences 101*, 11617–11621.
20. Knapp, M. J., Seebeck, F. P., and Klinman, J. P. (2001) Steric Control of Oxygenation Regiochemistry in Soybean Lipoxygenase-1, *J. Am. Chem. Soc. 123*, 2931–2932.
21. Zheng, Y., and Brash, A. R. (2010) Dioxygenase Activity of Epidermal Lipoxygenase-3 Unveiled, *Journal of Biological Chemistry 285*, 39866–39875.
22. Zheng, Y., and Brash, A. R. (2010) On the Role of Molecular Oxygen in Lipoxygenase Activation, *Journal of Biological Chemistry 285*, 39876–39887.
23. Cohen, J., Kim, K., King, P., Seibert, M., and Schulten, K. (2005) Finding Gas Diffusion Pathways in Proteins: Application to O_2 and H_2 Transport in CpI [FeFe]-Hydrogenase and the Role of Packing Defects, *Structure 13*, 1321–1329.

Chapter 2

Computational Characterization of SLO-1 Oxygen Transport Channel

2.1 Introduction

Computational Approach

Access of oxygen to the active site relies on the existence of channels and cavities in the protein matrix that are favorable for the hydrophobic gas to inhabit. Specific residues in the protein matrix act as gates along these routes, tuning access to the active site. (*1*) Computational approaches serve as a powerful lens through which to explore routes for gas travel in enzymes because they are able to provide a full picture of the protein from both a structural and energetic perspective.

Two complementary computational techniques were used to investigate gas migration pathways within SLO-1. Implicit ligand sampling (ILS) was used to assess regions of SLO-1 favorable for oxygen migration from a dynamic, energetic perspective. CAVER, by contrast, was employed to identify potential pathways from a purely geometric standpoint. Together, ILS and CAVER enabled not only the visualization of gas channels in SLO-1 but also the identification of critical residues implicated in modulating oxygen's access to the buried active site of the enzyme.

Implicit Ligand Sampling

Enzymes are dynamic systems whose thermal fluctuations play an important role in allowing ligands to migrate through the protein matrix. (*1*) ILS is a method tailored for assessing gas migration pathways based on a molecular dynamics simulation of the enzyme being studied. ILS makes the assumption that, because gas-protein interactions are weak, gas channels appear and disappear independently of the gas ligand itself. Protein dynamics are analyzed in the absence of any gas ligand and oxygen's presence is subsequently treated as a weak perturbation. With this approach, protein migration pathways can be sampled at every point throughout the protein matrix simultaneously and better statistics are generated than by sampling the trajectory of a hypothetical single ligand. (*2*, *3*)

ILS requires a five to ten nanosecond molecular dynamics simulation of the solvated enzyme as its input. The output is a three-dimensional potential of mean force (PMF) map that describes the Gibbs free energy cost associated with placing a gas molecule at any position inside the protein matrix. The free energy cost is calculated at every point on a finely spaced three-dimensional grid throughout the system and averaged over every segment of the trajectory. The lower the cost, or $\Delta G_s(O_2)$, at a particular location, the greater the probability of finding oxygen at that position. Regions favorable for oxygen migration can be identified by drawing PMF isoenergy surfaces—that is, plotting all points in a protein for which the $\Delta G_s(O_2)$ is below a certain value. (*2*, *3*)

ILS provides valuable dynamic and energetic insight into gas migration within enzymes. The technique has been employed successfully to analyze the migration free energy landscapes in a number of diverse systems, including but not limited to hemoglobin from seven distinct species, myoglobin from three species, copper-containing amine oxidase, aquaporin 1, homoprotocatechuate 2,3-dioxygenase, flavoprotein D-amino-acid oxidase, rabbit 12/15-lipoxygenase, truncated hemoglobin, and nitrophorin 4. (*2-10*)

CAVER

The protein matrix is characterized by a complex network of cavities and channels, some of which play a functional role in the transport of small molecules such as oxygen to the active site. (*11*) CAVER is a geometry-based computational technique that enables the detection and visualization of channels that link buried sites in proteins to the surrounding environment. Channels are detected based on purely geometric criteria—the protein is treated as a collection of "hard sphere" atoms with fixed radii. CAVER is a versatile tool in that it can be applied to either static crystal structures or molecular dynamics simulations. (*12*, *13*)

In addition to an x-ray crystal structure (or molecular dynamics simulation), starting point coordinates inside a cavity within the protein must be input into CAVER. CAVER subsequently identifies all possible continuous routes from the given starting point to the exterior of the protein. These pathways are also ranked by CAVER according to a 'throughput' parameter that takes into account channel length and width. Generally, shorter, wider channels are preferred to long, narrow channels. Characteristics such as length, mean radius, and bottleneck radius are also computed for each tunnel. (*13*)

CAVER provides a computationally inexpensive way to identify and visualize continuous routes from the solvent to buried sites within a protein. The technique has previously been used to probe pathways for gas migration in multiple systems, including but not limited to homoprotocatechuate 2,3-dioxygenase, FeFe hydrogenase, cytochrome P450, photosystem II, heme nitric oxide/oxygen binding domain, and haloalkane dehalogenase from three distinct species. (*7*, *12*-*18*)

2.2 Materials and Methods

Implicit Ligand Sampling

SLO-1 MD simulations and implicit ligand sampling were performed in collaboration with Dr. Kathleen Durkin of the UC Berkeley College of Chemistry Molecular Graphics and Computation Facility.

Preparation of SLO-1 Model
The LEaP module of the Amber 11 software package was used to generate a fully solvated model of SLO-1 based on the x-ray coordinates deposited in the Protein Data Bank (PDB entry: 1YGE). (*19*) In the crystal structure, the nonheme iron is in the ferrous state, complexed by the side chains of His^{499}, His^{504}, His^{690}, and Asn^{694} in addition to the carboxylate of Ile^{839} and a water molecule. (*20*) Topology and force field parameters for the bound water were adapted from a TIP3P model and are detailed in **Figure 2-1** and **2-2**. (*21*) Parameters for the iron ligand were adapted from those published for a six-coordinate iron in a heme-containing protein and are detailed in **Figure 2-3** and **2-4**. (*22*) Amber FF99 force field parameters were employed for the protein, as in previous SLO-1 simulations. (*23-25*) The SLO-1 structure was solvated in a truncated octahedral box of TIP3P waters, such that all solute atoms were at least 9 Å from the edge of the box. (*21*) The overall charge of system was neutralized by the addition of 11 peripheral sodium cations. The complete model consisted of 106,333 atoms.

Molecular Dynamics Simulation
The Sander module of the Amber 11 software package was employed to propagate a 10 ns simulation of SLO-1 with a time step of 2 fs. (*19*) An NPT ensemble (1 atm, 300K) was used, as is required for analysis by implicit ligand sampling. (*3*) Temperature was held constant using Langevin dynamics with a collision frequency of 1 ps^{-1}. Non-orthogonal periodic boundary conditions were employed with a truncated octahedral unit cell ($x = y = z = 111.262$ Å, $\alpha = \beta = \gamma = 109.471°$). Particle-mesh Ewald was used for long-range electrostatics and all other non-bonded interactions were calculated using a cutoff of 12 Å. All bonds involving hydrogen were constrained to their equilibrium lengths with the SHAKE algorithm.

Prior to the simulation, SLO-1 was minimized at constant volume for 10,000 steps while restraining the protein (with a force constant of 10 kcal mol^{-1} $Å^{-2}$) and 4,000 steps with no restraints. The system was subsequently equilibrated for 300 ps at constant volume and temperature and 1 ns at constant pressure and temperature before the simulation was run. The setup files for the minimization, equilibration, and simulation runs are available in **Figures 2-5**, **2-6**, and **2-7**, respectively.

Implicit Ligand Sampling
The ILS tool was applied to the molecular dynamics simulation of SLO-1 in order to assess regions favorable for oxygen migration within the enzyme. The ILS technique allows for the generation of a three-dimensional map of the Gibbs free energy cost, or $\Delta G_s(O_2)$, associated with transferring a oxygen molecule from a vacuum to a particular position inside the protein. (*3*) The lower the $\Delta G_s(O_2)$ at a particular location, the greater the probability of finding dioxygen there.

$\Delta G_s(O_2)$ was evaluated for every 1 $Å^3$ volume element throughout the SLO-1 system. Within each of these elements, oxygen was placed in 20 different rotational orientations at each of 27 different positions on a 3x3x3 grid. 5,000 protein conformations were sampled from the 10 ns trajectory. A three-dimensional free energy map was generated describing the distribution of oxygen throughout SLO-1. Regions of the enzyme likely to be occupied by oxygen were identified by drawing isoenergy surfaces—that is, plotting all points in a protein for which the $\Delta G_s(O_2)$ is below a certain value. Results were visualized in VMD, the molecular visualization program in which the ILS method is realized. (*26*)

CAVER

The CAVER 3.0 software tool was employed to identify pathways from the active site in SLO-1 to the exterior of the protein. (*13*) Given starting point coordinates within a static crystal structure or molecular dynamics simulation, CAVER identifies all possible routes to the solvent with a bottleneck radius larger than a specified minimum radius. These channels are ranked from most to least favorable by CAVER based on a 'throughput' parameter that takes into account both channel length and width. Parameters such as bottleneck radius, mean radius, and length are also computed and output by the program. In addition, CAVER can be used to automatically identify residues within a specified number of angstroms from the channel bottleneck.

Channels in the x-ray crystal structure of soybean lipoxygenase 1 (PDB entry: 1YGE) were identified and visualized using CAVER. To approximate the location of the active site, starting point coordinates within SLO-1 were computed as the spatial average of the coordinates of the catalytic iron atom and active site residue Leu^{546}. A minimum bottleneck radius of 0.9 Å was specified. Additional details regarding the configuration employed are available in **Figure 2-8**. Results were visualized in the molecular visualization program VMD to facilitate comparison to ILS results. (*26*)

2.3 Results

A network of cavities favorable for oxygen transport exists in SLO-1.
Implicit ligand sampling was used to evaluate regions favorable for oxygen travel within SLO-1. This technique infers gas migration pathways by generating a three-dimensional map of the Gibbs free energy cost, or $\Delta G_s(O_2)$, associated with placing an oxygen molecule anywhere in the protein. The lower the $\Delta G_s(O_2)$ at a particular location, the greater the probability of finding dioxygen there. Regions of the enzyme likely to be occupied by oxyen were identified by drawing isoenergy surfaces—that is, plotting all points in a protein for which the $\Delta G_s(O_2)$ is below a certain value. **Figure 2-9** depicts SLO-1 and pockets favorable for oxygen transport, in the form of the -0.5 kT isosurface generated by ILS.

Region of greatest oxygen favorability is proximal to the active site.
Lower free energy values are associated with a greater probability of finding oxygen. An isosurface with a free energy of -2.5 kT was visualized in order to identify regions most favorable for oxygen migration. This surface, pictured with SLO-1 in **Figure 2-10**, highlights regions proximal to the active site as likely regions for oxygen migration.

Multiple pathways exist from the active site to the exterior of the protein.
A complementary approach to ILS, CAVER, successfully identified multiple pathways from the active site to the exterior of the protein. These eight pathways are depicted in **Figure 2-11**. The length, average radius, and minimum radius of these channels are described in **Table 2-1**. The channels were also ranked from most favorable (A) to least favorable (H) by CAVER, based on a throughput parameter that takes into account channel length as well as width.

A single route to the active site is preferred by CAVER.
Channel A, depicted with SLO-1 in **Figure 2-12**, was identified by CAVER as the most favorable route for oxygen to travel from the solvent to the active site. This channel exhibited the highest throughput (0.4) and largest bottleneck radius (1.1 Å). Channel A was also the pathway with the 2nd largest mean radius and 2nd shortest total length, as detailed in **Table 2-1**. The evolving radius of Channel A is profiled in **Figure 2-13**. The channel's bottleneck is found approximately 7 Å from the start of the channel in the active site.

ILS and CAVER analysis implicate four key residues in oxygen transport.
Four residues were identified by CAVER to lie within 1.5 Å of the Channel A bottleneck—Ile^{553}, Ile^{547}, Leu^{496}, and Val^{564}. These residues are depicted with Channel A in **Figure 2-14**. Interestingly, all four residues are also in close proximity to the region identified by ILS as favorable for oxygen travel near the active site, as pictured in **Figure 2-15**. It appears that both computational methods are consistent with the importance of these four residues in defining an oxygen route within SLO-1.

2.4 Discussion

Two complementary techniques—ILS and CAVER—were used to investigate gas migration pathways in SLO-1 from a computational perspective. ILS was used to identify regions favorable for oxygen travel throughout the protein while CAVER was employed to visualize pathways leading continuously from the active site to the exterior of the protein.

ILS was successfully applied to a ten nanosecond molecular dynamics simulation of the solvated SLO-1 system. Regions favorable for oxygen to inhabit were delineated by drawing PMF isoenergy surfaces at -0.5 kT and -2.5 kT. The -0.5 kT isoenergy surface, depicted in **Figure 2-9**, highlighted a network of cavities favorable for oxygen transport in SLO-1. The -2.5 kT isoenergy surface, depicted in **Figure 2-10**, outlined regions most favorable for oxygen migration—many of which were found near the active site. One pocket to the left of the catalytic iron is located closest to the active site, making it a promising candidate for a role in oxygen delivery.

CAVER was used to detect pathways leading from the active site to the exterior of the protein. Although multiple pathways were found, Channel A, depicted in **Figure 2-12**, was identified by CAVER as the most favorable route from the active site. Four residues were identified within 1.5 Å of the bottleneck of this channel—Ile^{553}, Ile^{547}, Leu^{496}, and Val^{564}. These residues are pictured with Channel A in **Figure 2-14**. Their proximity to the bottleneck recommends these residues as gates capable of tuning oxygen's access to the active site.

In summary, the two computational techniques employed here to examine gas migration in SLO-1 implicate the same region of the protein in oxygen delivery. The four bottleneck residues identified as gatekeepers by CAVER are found in close proximity to the pocket outlined as favorable for oxygen migration by ILS. This pocket, which is located to the left of the active site, and the bottleneck residues are depicted together in **Figure 2-15**. Furthermore, the pocket identified by ILS directly overlaps with the top-ranked channel identified by CAVER, as is shown explicitly in **Figure 2-16**.

Together, energetic and geometric insights from ILS and CAVER point to a single pathway for oxygen delivery and implicate 4 residues in modulating oxygen access to the active site. These four residues were identified as candidates for mutagenesis to bulky residues such as phenylalanine and tryptophan. Introducing bulk at these gating residues is expected to disrupt oxygen access to the active site and therein corroborate the functional relevance of this channel.

It is interesting to note that the channel supported by our ILS and CAVER findings is consistent with the pathway originally detected crystallographically in SLO-1. (*20*) In fact, one of the bottleneck residues—Ile^{553}—has previously been mutated to a phenylalanine in the Klinman group. The Ile553Phe mutation was shown to disrupt oxygen access, as evidenced by a >3-fold increase in $K_M(O_2)$ and a fairly unchanged k_{cat}. The regio- and stereospecificity of the SLO-1 reaction was not disrupted in this mutant, however. (*27*) Mutating Ile^{553} to a tryptophan, as well as introducing bulk at other bottleneck residues, may have the potential to not only result in an increased $K_M(O_2)$ for SLO-1 but also to disrupt oxygen migration to the extent that reaction regio- and stereospecificity also becomes compromised.

```
    0    0    2

This is a remark line
molecule.res
BOW   INT  0
CORRECT     OMIT DU   BEG
  0.0000
   1  DUMM  DU    M    0  -1  -2     0.000      .0        .0      .00000
   2  DUMM  DU    M    1   0  -1     1.449      .0        .0      .00000
   3  DUMM  DU    M    2   1   0     1.522   111.1        .0      .00000
   4  O     OH    M    3   2   1     1.540   111.208   180.000  0.000000
   5  H1    HO    E    4   3   2     1.000   161.217   121.025  0.000000
   6  H2    HO    E    4   3   2     1.000    79.217  -119.332  0.000000


LOOP

IMPROPER

DONE
STOP
```

Figure 2-1. Topology information for the iron-bound water ligand (BOW) in SLO-1. The 'bow.in' file above was used to describe the chemical nature of the water ligand in the SLO-1 active site. This information was employed in the molecular dynamics simulation of the enzyme. Parameters were adapted from a TIP3P water model. (*21*)

```
!!index array str
 "bow"
!entry.bow.unit.atoms table  str name  str type  int typex  int resx  int flags  int
seq  int elmnt  dbl chg
 "O" "oh" 0 1 131072 1 8 0.0
 "H1" "ho" 0 1 131072 2 1 0.0
 "H2" "ho" 0 1 131072 3 1 0.0
!entry.bow.unit.atomspertinfo table  str pname  str ptype  int ptypex  int pelmnt  dbl
pchg
 "O" "oh" 0 -1 0.0
 "H1" "ho" 0 -1 0.0
 "H2" "ho" 0 -1 0.0
!entry.bow.unit.boundbox array dbl
 -1.000000
 0.0
 0.0
 0.0
 0.0
!entry.bow.unit.childsequence single int
 843
!entry.bow.unit.connect array int
 0
 1
!entry.bow.unit.connectivity table  int atom1x  int atom2x  int flags
 1 2 1
 1 3 1
!entry.bow.unit.hierarchy table  str abovetype  int abovex  str belowtype  int belowx
 "U" 0 "R" 1
 "R" 1 "A" 3
 "R" 1 "A" 2
 "R" 1 "A" 1
!entry.bow.unit.name single str
 ""
!entry.bow.unit.positions table  dbl x  dbl y  dbl z
 23.894000 46.596000 9.764000
 24.841000 46.762000 9.488000
 23.707000 47.077000 10.620000
!entry.bow.unit.residueconnect table  int c1x  int c2x  int c3x  int c4x  int c5x  int
c6x
 1 1 0 0 0 0
!entry.bow.unit.residues table  str name  int seq  int childseq  int startatomx  str
restype  int imagingx
 "BOW" 842 4 1 "?" 0
!entry.bow.unit.residuesPdbSequenceNumber array int
 1
!entry.bow.unit.solventcap array dbl
 -1.000000
 0.0
 0.0
 0.0
 0.0
!entry.bow.unit.velocities table  dbl x  dbl y  dbl z
 0.0 0.0 0.0
 0.0 0.0 0.0
 0.0 0.0 0.0
```

Figure 2-2. Force field parameters for the iron-bound water ligand (BOW) in SLO-1. The 'bow.lib' file above was employed in the molecular dynamics simulation of the enzyme. Parameters were adapted from a TIP3P water model. (*21*)

```
   0    0    2

    Heme residue  ALL ATOM, Yves names, Bayly-modified
heme_all.db3
HEM  INT     0
CORRECT  OMIT DU   BEG
   0.50000
   1   DUMM  DU    M      0   0   0       0.0000      0.0000      0.0000   0.0000
   2   DUMM  DU    M      1   0   0       1.4490      0.0000      0.0000   0.0000
   3   DUMM  DU    M      2   1   0       1.5220    111.1000      0.0000   0.0000
  19   FE    FE    M     16  14  12       2.1000    124.0000    180.0000   0.2500
  20   NA    NP    S     19  16  14       2.0800     98.0000     90.0000  -0.1800
  21   C1A   CC    S     20  19  16       1.3800    125.4000     90.0000   0.0300
  22   C2A   CB    B     21  20  19       1.4100    109.0000    180.0000  -0.0200
  23   CAA   CT    3     22  21  20       1.5100    124.0000    180.0000  -0.1600
  24   HP71  HC    E     23  22  21       1.0900    109.5000     60.0000   0.1000
  25   HP72  HC    E     23  22  21       1.0900    109.5000    300.0000   0.1000
  26   CBA   CT    3     23  22  21       1.5400    111.0000    180.0000  -0.3000
  27   HP73  HC    E     26  23  22       1.0900    109.5000     60.0000   0.1000
  28   HP74  HC    E     26  23  22       1.0900    109.5000    300.0000   0.1000
  29   CGA   C     B     26  23  22       1.5270    109.4000    180.0000   0.3000
  30   O1A   O2    E     29  26  23       1.2600    117.2000     90.0000  -0.5000
  31   O2A   O2    E     29  26  23       1.2600    117.2000    270.0000  -0.5000
  32   C3A   CB    B     22  21  20       1.4100    107.0000      0.0000   0.0200
  33   CMA   CT    3     32  22  21       1.5100    125.0000    180.0000  -0.2650
  34   HM81  HC    E     33  32  22       1.0900    109.5000     60.0000   0.0750
  35   HM82  HC    E     33  32  22       1.0900    109.5000    180.0000   0.0750
  36   HM83  HC    E     33  32  22       1.0900    109.5000    300.0000   0.0750
  37   C4A   CC    S     32  22  21       1.4100    107.0000      0.0000   0.0200
  38   CHB   CD    B     37  32  22       1.3700    127.0000    180.0000  -0.1100
  39   HDM   HC    E     38  37  32       1.0800    120.0000      0.0000   0.1500
  40   C1B   CC    B     38  37  32       1.3700    127.0000    180.0000   0.0300
  41   NB    NO    E     40  38  37       1.3800    124.0000      0.0000  -0.1800
  42   C2B   CB    B     40  38  37       1.4100    127.0000    180.0000   0.0200
  43   CMB   CT    3     42  40  38       1.5100    125.0000      0.0000  -0.2650
  44   HM11  HC    E     43  42  40       1.0900    109.5000     60.0000   0.0750
  45   HM12  HC    E     43  42  40       1.0900    109.5000    180.0000   0.0750
  46   HM13  HC    E     43  42  40       1.0900    109.5000    300.0000   0.0750
  47   C3B   CB    B     42  40  38       1.4100    107.0000    180.0000  -0.0500
  48   CAB   CY    B     47  42  40       1.5100    126.0000    180.0000  -0.1300
  49   HV2   HC    E     48  47  42       1.0800    120.0000      0.0000   0.1500
  50   CBB   CX    B     48  47  42       1.3300    120.0000    180.0000  -0.3000
  51   HVC2  HC    E     50  48  47       1.0800    120.0000      0.0000   0.1000
  52   HVT2  HC    E     50  48  47       1.0800    120.0000    180.0000   0.1000
  53   C4B   CC    S     47  42  40       1.4100    107.0000      0.0000   0.0200
  54   CHC   CD    B     53  47  42       1.3700    127.0000    180.0000  -0.1100
  55   HAM   HC    E     54  53  47       1.0800    120.0000      0.0000   0.1500
  56   C1C   CC    B     54  53  47       1.3700    130.0000    180.0000   0.0300
  57   NC    NP    E     56  54  53       1.3800    124.0000      0.0000  -0.1800
  58   C2C   CB    B     56  54  53       1.4100    127.0000    180.0000   0.0200
  59   CMC   CT    3     58  56  54       1.5100    125.0000      0.0000  -0.2650
  60   HM31  HC    E     59  58  56       1.0900    109.5000     60.0000   0.0750
  61   HM32  HC    E     59  58  56       1.0900    109.5000    180.0000   0.0750
  62   HM33  HC    E     59  58  56       1.0900    109.5000    300.0000   0.0750
  63   C3C   CB    B     58  56  54       1.4100    107.0000    180.0000  -0.0500
  64   CAC   CY    B     63  58  56       1.5100    126.0000    180.0000  -0.1200
  65   HV4   HC    E     64  63  58       1.0800    120.0000      0.0000   0.1500
  66   CBC   CX    B     64  63  58       1.3300    120.0000    180.0000  -0.3000
  67   HVC4  HC    E     66  64  63       1.0800    120.0000      0.0000   0.1000
  68   HVT4  HC    E     66  64  63       1.0800    120.0000    180.0000   0.1000
  69   C4C   CC    S     63  58  56       1.4100    107.0000      0.0000   0.0200
  70   CHD   CD    B     69  63  58       1.3700    127.0000    180.0000  -0.1100
  71   HBM   HC    E     70  69  63       1.0800    120.0000      0.0000   0.1500
```

```
  72   C1D   CC    B     70  69  63       1.3700    130.0000    180.0000   0.0300
  73   ND    NO    E     72  70  69       1.3800    124.0000      0.0000  -0.1800
  74   C2D   CB    B     72  70  69       1.4100    127.0000    180.0000   0.0200
  75   CMD   CT    3     74  72  70       1.5100    125.0000      0.0000  -0.2650
  76   HM51  HC    E     75  74  72       1.0900    109.5000     60.0000   0.0750
  77   HM52  HC    E     75  74  72       1.0900    109.5000    180.0000   0.0750
  78   HM53  HC    E     75  74  72       1.0900    109.5000    300.0000   0.0750
  79   C3D   CB    B     74  72  70       1.4100    107.0000    180.0000  -0.0200
  80   C4D   CC    S     79  74  72       1.4100    107.0000      0.0000   0.0200
  81   CHA   CD    S     80  79  74       1.3700    127.0000    180.0000  -0.1100
  82   HGM   HC    E     81  80  79       1.0800    120.0000      0.0000   0.1500
  83   CAD   CT    3     79  74  72       1.5100    124.0000    180.0000  -0.1600
  84   HP61  HC    E     83  79  74       1.0900    109.5000     60.0000   0.1000
  85   HP62  HC    E     83  79  74       1.0900    109.5000    300.0000   0.1000
  86   CBD   CT    3     83  79  74       1.5400    111.0000    180.0000  -0.3000
  87   HP63  HC    E     86  83  79       1.0900    109.5000     60.0000   0.1000
  88   HP64  HC    E     86  83  79       1.0900    109.5000    300.0000   0.1000
  89   CGD   C     B     86  83  79       1.5300    109.4000    180.0000   0.3000
  90   O1D   O2    E     89  86  83       1.2600    117.2000     90.0000  -0.5000
  91   O2D   O2    E     89  86  83       1.2600    117.2000    270.0000  -0.5000

LOOP  EXPLICIT
 NA   C4A
 FE   NB
 FE   NC
 FE   ND
 NB   C4B
 NC   C4C
 ND   C4D
 C1A  CHA

IMPROPER
 NA   C1A  C4A  FE
 NB   C1B  C4B  FE
 NC   C1C  C4C  FE
 ND   C1D  C4D  FE
 C1A  C2A  NA   CHA
 C1B  C2B  NB   CHB
```

Figure 2-3. Topology information for the catalytic iron atom in SLO-1. The 'fe.in' file above was used to describe the chemical nature of the iron atom in the SLO-1 active site. This information was employed in the molecular dynamics simulation of the enzyme. Parameters were adapted from those published for a six-coordinate iron ligand in a heme-containing protein. (*22*)

```
#modifed from frcmod.hemall - KD 2010

MASS
NB 14.01
FE 55.85

BOND
FE-OH   70.000     2.10
FE-NB   60.000     2.23
FE-O2   50.000     2.18
FE-O    70.000     2.40

ANGLE
NB-FE-NB    50.000      90.000
NB-FE-O     50.000      90.000
NB-FE-OH    50.000      90.000
NB-FE-O2    50.000      90.000
OH-FE-O2    50.000      90.000
OH-FE-O     50.000      90.000
O-FE-O2     50.000      90.000
FE-NB-C     30.000     127.400
FE-O2-C     30.000     112.200
FE-O-C      30.000     128.000
FE-OH-HO    30.000     125.000
CR-NB-FE    30.000     122.400
CV-NB-FE    30.000     130.100
HO-OH-HO    100.000      104.52 ! from TIP3P water

#see http://ambermd.org/formats.html#frcmod
DIHEDRAL
X -NB-FE-X    1       0.000     180.000       2.000
X -O2-FE-X    1       0.000     180.000       2.000
X -O-FE-X     1       0.000     180.000       2.000
X -OH-FE-X    1       0.000     180.000       2.000
X -O2-C-X    1       0.000     180.000       2.000

NONBON
  FE         1.20000   0.05000   0.00000
```

Figure 2-4. Force field parameters for the catalytic iron atom in SLO-1. The 'fe.frc' file above was employed in the molecular dynamics simulation of the enzyme. Parameters were adapted from those published for a six-coordinate iron ligand in a heme-containing protein. (*22*)

```
Minimization 1
 &cntrl
  imin   = 1,
  ntmin =  1,
  maxcyc = 10000,
  ncyc   = 5000,
  ntpr = 10,
  ntb    = 1,
  cut    = 8,
  ntr = 1,
  restraint_wt=10.0,
  restraintmask=':1-839'
 /

Minimization 2
 &cntrl
  imin   = 1,
  ntmin =  1,
  maxcyc = 4000,
  ncyc   = 50,
  ntb    = 1,
  cut    = 12,
 /
```

Figure 2-5. Settings employed for the first and second minimization runs of SLO-1. SLO-1 was minimized at constant volume for 10,000 steps while restraining the protein (with a force constant of 10 kcal mol^{-1} $Å^{-2}$) and 4,000 steps with no restraints.

```
Equilibration 1
 &cntrl
  ntx = 1
  ntb = 1,
  cut = 12,
  ntc=2, ntf = 2,
  ntt = 3, gamma_ln = 1.0,
  tempi = 0.0,
  temp0 = 300.0,
  nstlim = 150000,
  dt = 0.002,
  ntpr = 100,
  ntwx = 100,
  ntwr = 1000
 /

Equilibration 2
 &cntrl
  ntx = 5
  ntb = 2, pres0 = 1.0, ntp = 1, taup = 2.0,
  cut = 12,
  ntc=2, ntf = 2,
  ntt = 3, gamma_ln = 1.0,
  temp0 = 300.0,
  nstlim = 500000,
  dt = 0.002,
  ntpr = 100,
  ntwx = 100,
  ntwr = 1000
 /
```

Figure 2-6. Settings employed for the first and second equilibration runs of SLO-1. The system was equilibrated for 300 ps at constant volume and temperature and 1 ns at constant pressure and temperature before the simulation was run.

```
Dynamics Run
 &cntrl
  ntx = 5
  ntb = 2, pres0 = 1.0, ntp = 1, taup = 2.0,
  cut = 12,
  ntc=2, ntf = 2,
  ntt = 3, gamma_ln = 1.0,
  temp0 = 300.0,
  nstlim = 5000000,
  dt = 0.002,
  ntpr = 100,
  ntwx = 100,
  ntwr = 1000
 /
```

Figure 2-7. Settings employed for the 10 ns molecular dynamics simulation of SLO-1. The simulation was performed using a constant pressure (1 atm) and temperature (300K) ensemble (NPT) as is required for analysis by implicit ligand sampling. (*3*)

```
# CALCULATION SETUP
load_tunnels no
load_cluster_tree no

# INPUT DATA
time_sparsity 1
first_frame 1
last_frame 10

# TUNNEL CALCULATION
probe_radius 0.9
shell_radius 3
shell_depth 4

# TUNNEL CLUSTERING
clustering average_link
weighting_coefficient 1
clustering_threshold 3.5

# GENERATION OF OUTPUTS
one_tunnel_in_snapshot cheapest
save_dynamics_visualization yes
generate_summary yes
generate_tunnel_characteristics yes
generate_tunnel_profiles yes
generate_histograms yes
bottleneck_histogram 0.0 2.0 20
throughput_histogram 0 1.0 10
generate_bottleneck_heat_map yes
bottleneck_heat_map_range 1.0 2.0
bottleneck_heat_map_element_size 10 20
generate_profile_heat_map yes
profile_heat_map_resolution 0.5
profile_heat_map_range 1.0 2.0
profile_heat_map_element_size 20 10
compute_tunnel_residues yes
residue_contact_distance 1.5
compute_bottleneck_residues yes
bottleneck_contact_distance 1.5

# ADVANCED SETTINGS
number_of_approximating_balls 12
compute_errors no
save_error_profiles no
path_to_vmd "C:/Program Files/University of Illinois/VMD/vmd.exe"
generate_trajectory yes

# Others
swap no
seed 1
starting_point_coordinates -6.104 2.553 2.491
```

Figure 2-8. Configuration employed for analysis of SLO-1 by CAVER. The x-ray crystal structure of SLO-1 served as the input structure. Starting point coordinates in the active site were computed as the spatial average of the coordinates of the catalytic iron atom and active site residue Leu^{546}. A minimum bottleneck radius of 0.9 Å was specified.

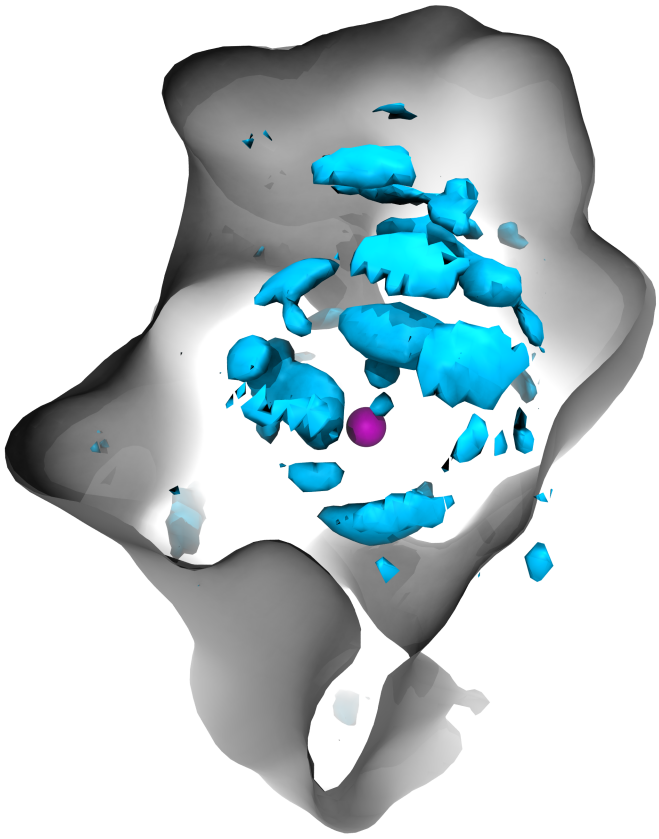

Figure 2-9. SLO-1 depicted with the -0.5 kT isoenergy surface computed by ILS. The -0.5 kT isoenergy surface (cyan) highlights multiple, preferred pockets for oxygen to inhabit throughout the SLO-1 protein matrix (gray). The active site iron of SLO-1 is represented as a magenta sphere.

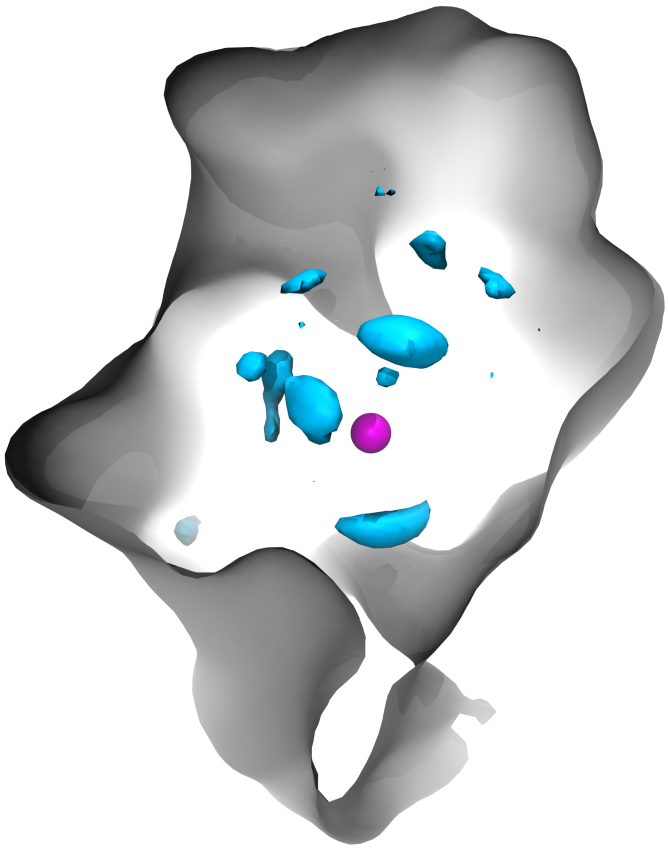

Figure 2-10. SLO-1 depicted with the -2.5 kT isoenergy surface computed by ILS. The -2.5 kT isoenergy surface (cyan) imposes a more stringent requirement than the -0.5 kT surface, including only the most favorable regions for oxygen migration in the protein matrix (gray). These regions tend to be in the neighborhood of the active site of SLO-1. Note the pocket to the left of the catalytic iron (magenta), which is located closest to the active site.

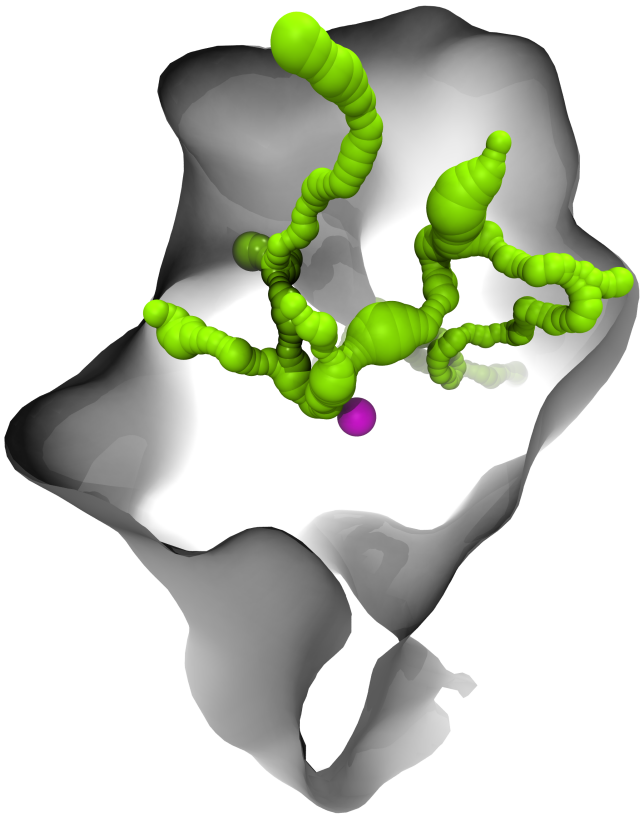

Figure 2-11. SLO-1 depicted with the eight channels detected by CAVER. CAVER detected 8 channels (green) extending from the buried active site in SLO-1 to the exterior of the protein. The surface of SLO-1 is depicted in gray and the catalytic iron, a hallmark of the active site, is represented as a magenta sphere.

Tunnel	A	B	C	D	E	F	G	H
Length (Å)	21	20	25	41	50	44	109	133
Mean radius (Å)	1.6	1.4	1.5	1.8	1.5	1.4	1.3	1.3
Bottleneck radius (Å)	1.1	0.9	1	0.9	0.9	1	0.9	0.9
Throughput	0.4	0.3	0.3	0.2	0.1	0.1	0.002	0.0003

Table 2-1. Characterization of eight channels detected and ranked by CAVER. Length, mean radius, and bottleneck radius were computed by the program, in addition to a throughput parameter that reflects the overall competency of each channel. Based on this throughput parameter, each channel was ranked by CAVER, with (A) representing the most favorable tunnel and (H) representing the least favorable path. Pathways with small lengths and large radii (e.g. A) were preferred to longer, narrower tunnels (e.g. H).

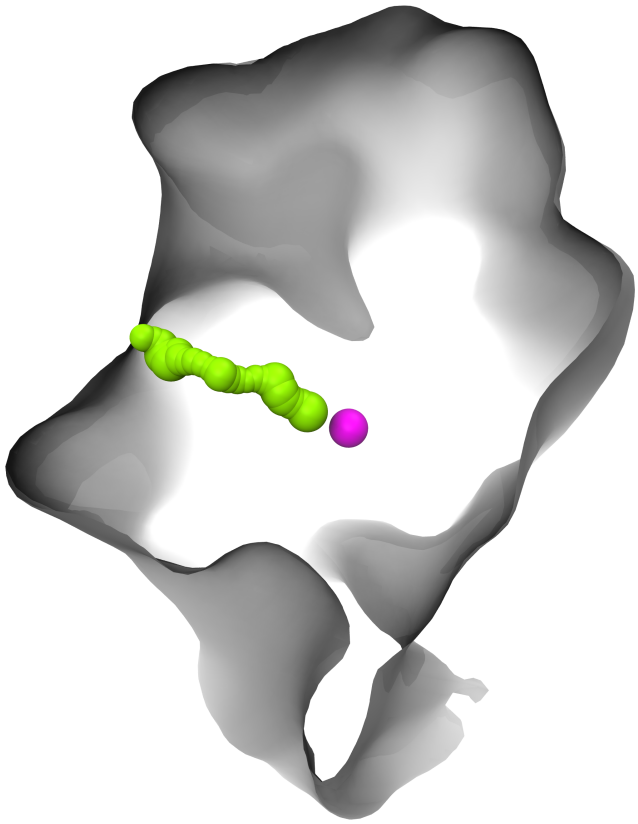

Figure 2-12. SLO-1 depicted with Channel A as detected by CAVER. Channel A (green) was identified as the most favorable route from the active site to the solvent by CAVER according to the throughput metric, which favors short, reasonably wide channels. SLO-1 is represented by a gray surface and the catalytic iron atom is depicted as a magenta sphere. Channel A coincides with the putative channel previously identified by the Klinman group based on crystallographic evidence. (*27*)

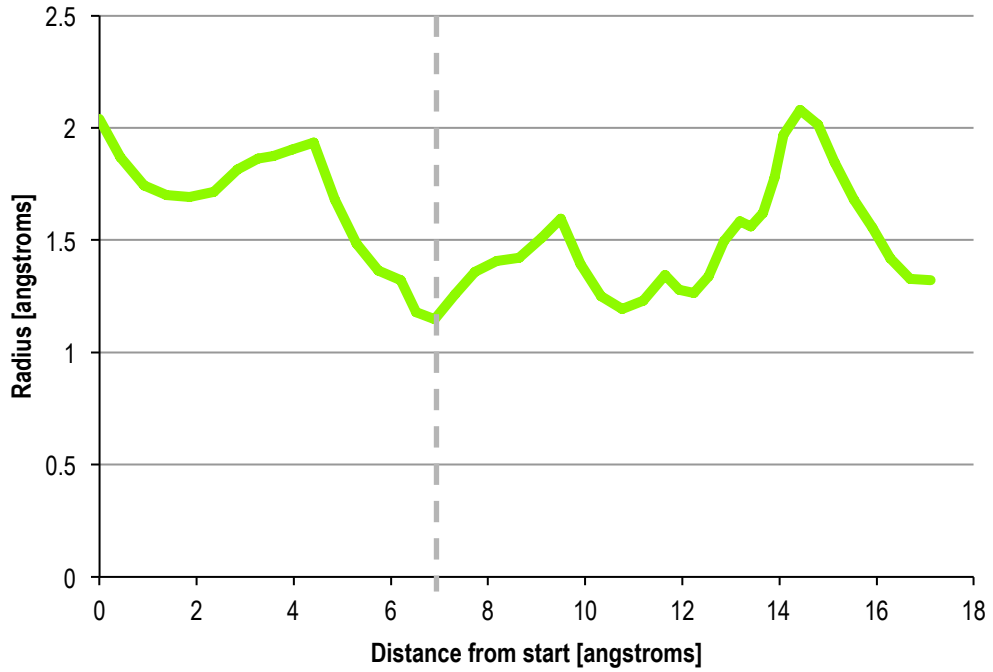

Figure 2-13. Profile of Channel A, the top-ranked pathway identified by CAVER. Channel A's radius at regular distance intervals from its starting point in the active site was computed and mapped as a function of distance. The bottleneck radius of Channel A—1.1 Å—is found at approximately 7 Å from the active site, as indicated by the dotted gray line. Residues within 1.5 Å of Channel A's bottleneck are listed here, sorted from closest: Ile^{553}, Ile^{547}, Leu^{496}, and Val^{564}.

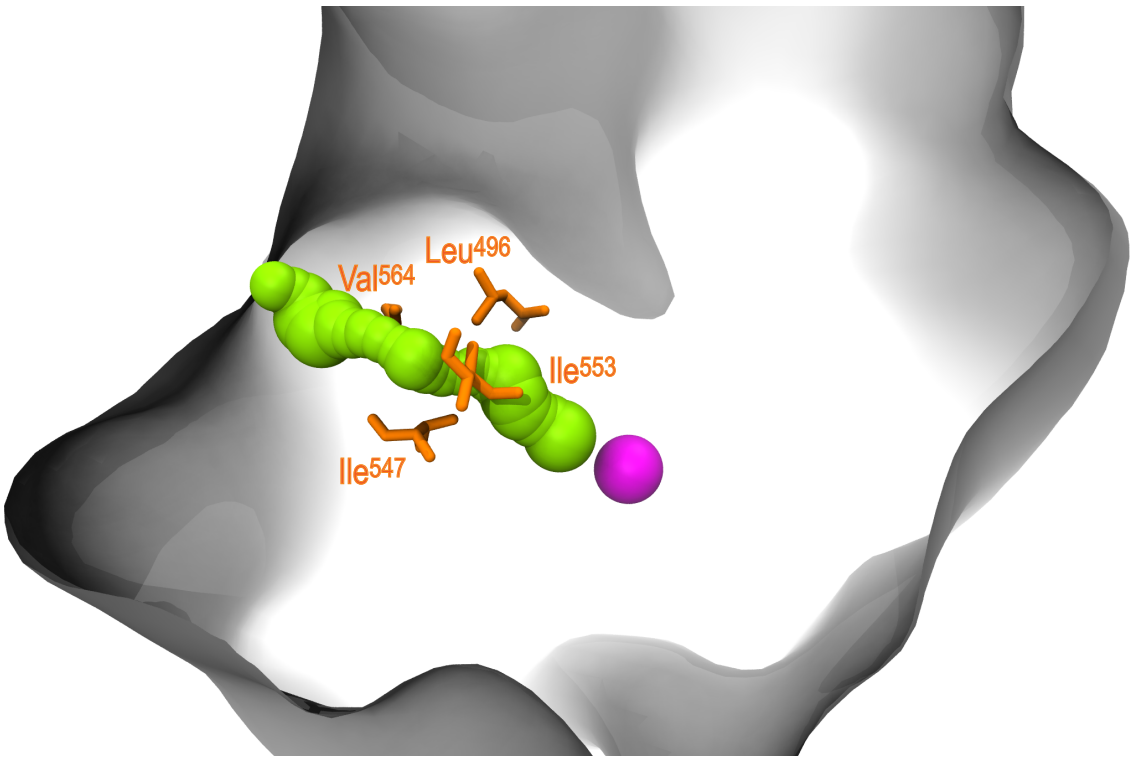

Figure 2-14. SLO-1 depicted with Channel A and its bottleneck residues. Channel A (green) was identified as the most favorable route from the active site to the solvent by CAVER. Residues within 1.5 Å of Channel A's bottleneck are depicted in orange, and are listed here, sorted from closest: Ile^{553}, Ile^{547}, Leu^{496}, and Val^{564}. SLO-1 is represented by a gray surface and the catalytic iron atom is depicted as a magenta sphere.

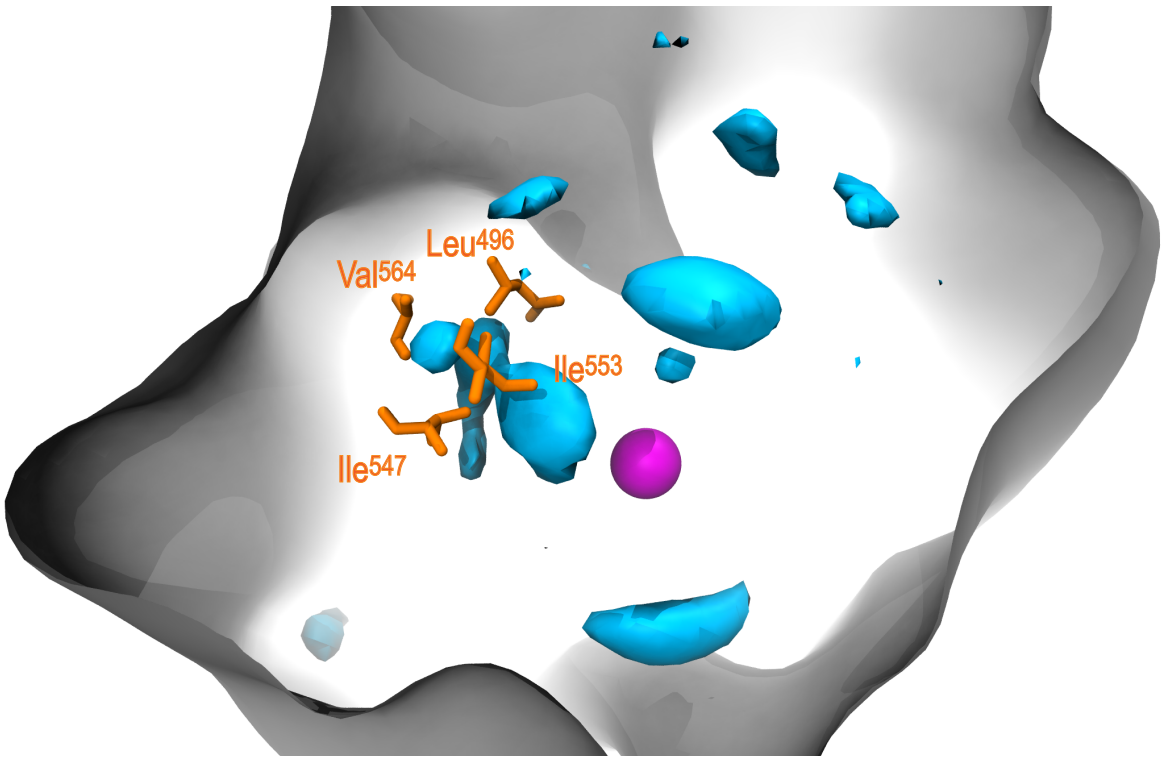

Figure 2-15. SLO-1 depicted with the -2.5 kT isoenergy surface computed by ILS and the bottleneck residues identified by CAVER. The -2.5 kT isoenergy surface (cyan) highlights regions of the protein most favorable for oxygen migration. The region computed by ILS that is closest to the active site is in close proximity to the bottleneck residues identified by CAVER, highlighting the accordance of these two techniques. Bottleneck residues are depicted in orange, and are listed here, sorted from closest: Ile^{553}, Ile^{547}, Leu^{496}, and Val^{564}. SLO-1 is represented by a gray surface and the catalytic iron atom is depicted as a magenta sphere.

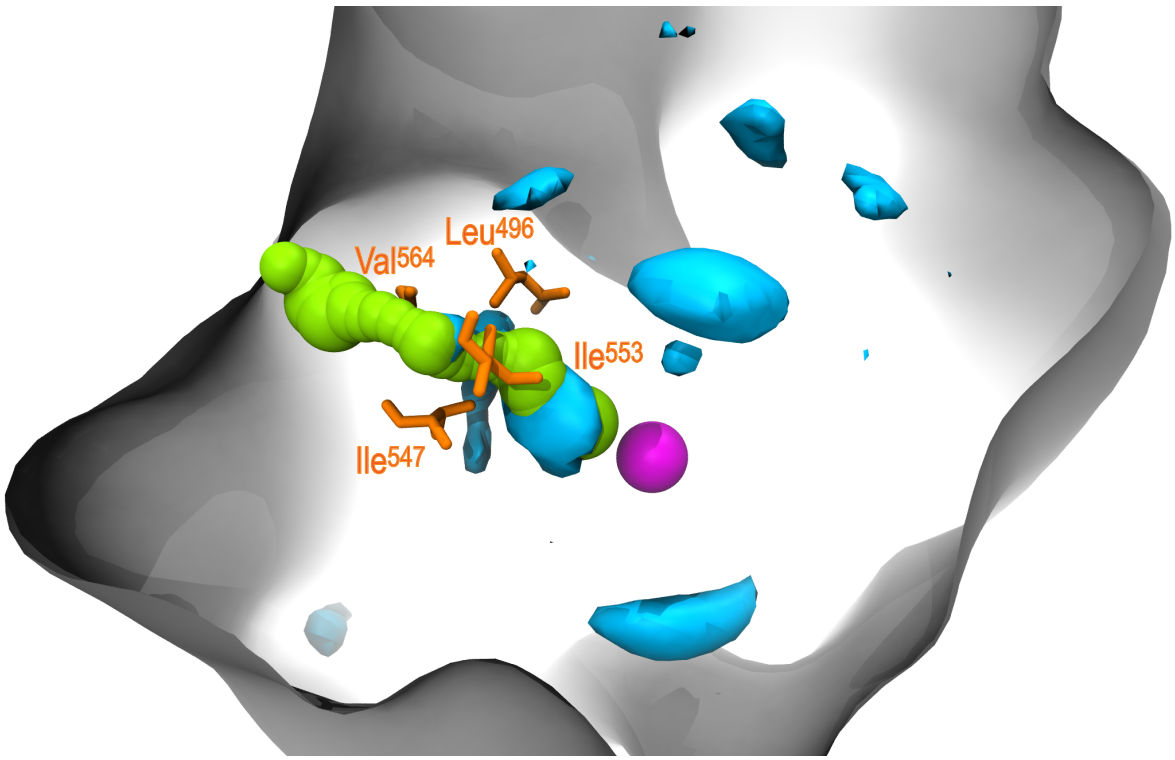

Figure 2-16. SLO-1 depicted with the -2.5 kT isoenergy surface generated by ILS as well as Channel A and its bottleneck residues. The -2.5 kT isoenergy surface (cyan) highlights regions of the protein most favorable for oxygen migration. The region computed by ILS that is closest to the active site directly overlaps with Channel A (green), the top-ranked channel detected by CAVER. This region is also in close proximity to the bottleneck residues identified by CAVER (orange), highlighting the accordance of these two techniques. Overlap of the -2.5 kT isoenergy surface with other channels detected by CAVER (B-H) is comparatively small, consistent with Channel A representing the biologically relevant pathway. SLO-1 is represented by a gray surface and the catalytic iron atom is depicted as a magenta sphere.

References

1. Arroyo-Mañez, P., Bikiel, D. E., Boechi, L., Capece, L., Di Lella, S., Estrin, D. A., Marti, M. A., Moreno, D. M., Nadra, A. D., and Petruk, A. A. (2011) Protein dynamics and ligand migration interplay as studied by computer simulation, *Biochimica et Biophysica Acta (BBA) - Proteins and Proteomics 1814*, 1054–1064.
2. Cohen, J., Arkhipov, A., Braun, R., and Schulten, K. (2006) Imaging the Migration Pathways for O_2, CO, NO, and Xe Inside Myoglobin, *Biophysical Journal 91*, 1844–1857.
3. Cohen, J., Olsen, K. W., and Schulten, K. (2008) Finding Gas Migration Pathways in Proteins Using Implicit Ligand Sampling, *Methods in Enzymology 437*, 439–457.
4. Cohen, J., and Schulten, K. (2007) O_2 Migration Pathways Are Not Conserved across Proteins of a Similar Fold, *Biophysical Journal 93*, 3591–3600.
5. Johnson, B. J., Cohen, J., Welford, R. W., Pearson, A. R., Schulten, K., Klinman, J. P., and Wilmot, C. M. (2007) Exploring molecular oxygen pathways in Hansenula polymorpha copper-containing amine oxidase, *Journal of Biological Chemistry 282*, 17767–17776.
6. Wang, Y., Cohen, J., Boron, W. F., Schulten, K., and Tajkhorshid, E. (2007) Exploring gas permeability of cellular membranes and membrane channels with molecular dynamics, *Journal of Structural Biology 157*, 534–544.
7. Xu, L., Zhao, W., and Wang, X. (2009) Finding molecular dioxygen tunnels in homoprotocatechuate 2,3-dioxygenase: implications for different reactivity of identical subunits, *Eur. Biophys. J. 39*, 327–336.
8. Saam, J., Rosini, E., Molla, G., Schulten, K., Pollegioni, L., and Ghisla, S. (2010) O_2 Reactivity of Flavoproteins: Dynamic Access of Dioxygen to the Active Site and Role of a H+ Relay System in $_D$-Amino Acid Oxidase, *Journal of Biological Chemistry 285*, 24439–24446.
9. Saam, J., Ivanov, I., Walther, M., Holzhütter, H. G., and Kuhn, H. (2007) Molecular dioxygen enters the active site of 12/15-lipoxygenase via dynamic oxygen access channels, *Proceedings of the National Academy of Sciences 104*, 13319–13324.
10. Forti, F., Boechi, L., Estrin, D. A., and Marti, M. A. (2011) Comparing and combining implicit ligand sampling with multiple steered molecular dynamics to study ligand migration processes in heme proteins, *J. Comput. Chem. 32*, 2219–2231.
11. Brezovsky, J., Chovancova, E., Gora, A., Pavelka, A., Biedermannova, L., and Damborský, J. (2013) Software tools for identification, visualization and analysis of protein tunnels and channels, *Biotechnology Advances 31*, 38–49.
12. Petřek, M., Otyepka, M., Banáš, P., Košinová, P., Koča, J., and Damborský, J. (2006) CAVER: a new tool to explore routes from protein clefts, pockets and cavities, *BMC Bioinformatics 7*, 316.
13. Chovancova, E., Pavelka, A., Benes, P., Strnad, O., Brezovsky, J., Kozlikova, B., Gora, A., Sustr, V., Klvana, M., Medek, P., Biedermannova, L., Sochor, J., and Damborský, J. (2012) CAVER 3.0: A Tool for the Analysis of Transport Pathways in Dynamic Protein Structures, *PLoS Comput. Biol. 8(10)*, e1002708.
14. Lautier, T., Ezanno, P., Baffert, C., Fourmond, V., Cournac, L., Fontecilla-Camps, J. C., Soucaille, P., Bertrand, P., Meynial-Salles, I., and Léger, C. (2011) The quest for a functional substrate access tunnel in FeFe hydrogenase, *Faraday discussions 148*, 385–407.

15. Otyepka, M., Skopalík, J., Anzenbacherová, E., and Anzenbacher, P. (2007) What common structural features and variations of mammalian P450s are known to date?, *Biochimica et Biophysica Acta (BBA) - General Subjects 1770*, 376–389.
16. Murray, J. W., and Barber, J. (2007) Structural characteristics of channels and pathways in photosystem II including the identification of an oxygen channel, *Journal of Structural Biology 159*, 228–237.
17. Winter, M. B., Herzik, M. A., Jr, Kuriyan, J., and Marletta, M. A. (2011) Tunnels modulate ligand flux in a heme nitric oxide/oxygen binding (H-NOX) domain, *Proceedings of the National Academy of Sciences 108*, E881–E889.
18. Pavlova, M., Klvana, M., Prokop, Z., Chaloupkova, R., Banáš, P., Otyepka, M., Wade, R. C., Tsuda, M., Nagata, Y., and Damborský, J. (2009) Redesigning dehalogenase access tunnels as a strategy for degrading an anthropogenic substrate, *Nature Chemical Biology 5*, 727–733.
19. Case, D. A., Darden, T. A., Cheatham, T. E., III, Simmerling, C. L., Wang, J., Duke, R. E., Luo, R., Walker, R. C., Zhang, W., Merz, K. M., Roberts, B., Wang, B., Hayik, S., Roitberg, A., Seabra, G., Kolossvary, I., Wong, K. F., Paesani, F., Vanicek, J., Liu, J., Wu, X., Brozell, S. R., Steinbrecher, T., Gohlke, H., Cai, Q., Ye, X., Wang, J., Hsieh, M. -J., Cui, G., Roe, D. R., Mathews, D. H., Seetin, M. G., Sagui, C., Babin, V., Luchko, T., Gusarov, S., Kovalenko, A., and Kollman, P. A. (2010) AMBER 11, *University of California, San Francisco*.
20. Minor, W., Steczko, J., Boguslaw Stec, O., Otwinowski, Z., Bolin, J. T., Walter, R., and Axelrod, B. (1996) Crystal structure of soybean lipoxygenase L-1 at 1.4 Å resolution, *Biochemistry 35*, 10687–10701.
21. Jorgensen, W. L., Chandrasekhar, J., Madura, J. D., Impey, R. W., and Klein, M. L. (1983) Comparison of simple potential functions for simulating liquid water, *The Journal of Chemical Physics 79*, 926.
22. Giammona, D. A. (1984) Ph.D. Thesis, *University of California, Davis.*
23. Wang, J., Cieplak, P., and Kollman, P. A. (2000) How well does a restrained electrostatic potential (RESP) model perform in calculating conformational energies of organic and biological molecules?, *J. Comput. Chem. 21*, 1049–1074.
24. Hatcher, E., Soudackov, A. V., and Hammes-Schiffer, S. (2007) Proton-Coupled Electron Transfer in Soybean Lipoxygenase: Dynamical Behavior and Temperature Dependence of Kinetic Isotope Effects, *J. Am. Chem. Soc. 129*, 187–196.
25. Edwards, S. J., Soudackov, A. V., and Hammes-Schiffer, S. (2010) Impact of Distal Mutation on Hydrogen Transfer Interface and Substrate Conformation in Soybean Lipoxygenase, *J. Phys. Chem. B 114*, 6653–6660.
26. Humphrey, W., Dalke, A., and Schulten, K. (1996) VMD: Visual Molecular Dynamics, *Journal of Molecular Graphics 14*, 33–38.
27. Knapp, M. J., Seebeck, F. P., and Klinman, J. P. (2001) Steric Control of Oxygenation Regiochemistry in Soybean Lipoxygenase-1, *J. Am. Chem. Soc. 123*, 2931–2932.

Chapter 3

Kinetics and Regio/stereospecificity of SLO-1 Channel Mutants

3.1 Introduction

Mutagenesis Approach

The lipoxygenase (LOX) family catalyzes the regio- and stereospecific peroxidation of polyunsaturated fatty acids. How these enzymes are able to generate chiral hydroperoxides with exquisite regio- and stereospecificity remains an open question. A role for oxygen channels in delivering the small, hydrophobic gas to the active site has been proposed in a number of lipoxygenases. (*1*) This hypothesis was addressed using soybean lipoxygenase 1 (SLO-1), a prototypical non-heme iron-containing lipoxygenase and the best-studied model of LOX catalysis and structure.

Computational analysis of gas migration pathways in SLO-1—described in **Chapter 2**—identified a putative oxygen transport route linking the active site to the exterior of the protein. This channel, previously identified crystallographically, is hypothesized to deliver O_2 to the active site, ensuring reaction regio- and stereospecificity. (*2*) The functional role of this pathway was evaluated by introducing bulk into the channel via site-directed mutagenesis. The four bottleneck residues of the channel—Ile^{553}, Ile^{547}, Leu^{496}, and Val^{564}—were selected as mutagenesis targets. Disruption of O_2 migration was assessed by evaluating both kinetic parameters and reaction regio- and stereospecificity.

Kinetic Characterization

SLO-1 catalyzes the peroxidation of linoleic acid (LA) to 13S hydroperoxyoctadecadienoic acid (13S HPOD), as depicted in **Scheme 1-1**. The reaction occurs in three chemical steps—hydrogen abstraction, oxygen insertion, and peroxy radical reduction. Hydrogen atom abstraction from LA by the active-site Fe^{3+}-OH generates a carbon-based linoleyl radical and Fe^{2+}-OH_2. The linoleyl radical is then trapped by oxygen to yield a 13S-peroxyl radical. Finally, the peroxyl radical is reduced, producing 13S-HPOD and re-generating the active-site Fe^{3+}-OH. (*3*)

Enzyme kinetics can be analyzed by determining reaction rate at varying concentrations of linoleic acid (LA) and molecular oxygen. Parameters such as k_{cat}, $K_M(LA)$, and $K_M(O_2)$ are determined by nonlinear least-squares fitting to the Michaelis-Menten equation. (*3*, *4*) Disruptions in oxygen trafficking are expected to primarily affect $K_M(O_2)$ since k_{cat} is limited by $H^{\cdot}$ abstraction and $K_M(LA)$ primarily reflects LA binding. Blocking oxygen delivery to the active site is expected to leave k_{cat} relatively unchanged while significantly increasing $K_M(O_2)$ relative to wild-type SLO-1. That is, obstructing the channel should hinder O_2 access to the linoleyl radical but not affect the rate of $H^{\cdot}$ abstraction from LA itself. (*3*, *5*)

Mutagenesis of one bottleneck residue—Ile^{553}—has previously been performed in the Klinman group. As expected, introducing phenylalanine at this position primarily impacts $K_M(O_2)$, increasing this parameter by over 3-fold. $K_M(LA)$ remains unchanged in this mutant and k_{cat} is reduced by 2-fold. The regio- and stereospecificity of the Ile553Trp mutant reaction remains unperturbed compared to wild-type SLO-1. The kinetic profile of the Ile553Phe mutant is consistent with a role for the putative channel in facilitating oxygen diffusion to the active site. (*3*, *5*)

Characterization of Reaction Regio- and Stereospecificity

In addition to kinetic parameters such as $K_M(O_2)$, reaction regio- and stereospecificity also reports on oxygen targeting to the active site. At ambient oxygen, hydrogen abstraction, oxygen insertion, and peroxyl radical reduction proceed as described in **Scheme 1-1** and 13S HPOD is generated. Under conditions of low oxygen, by contrast, regio- and stereospecificity is disrupted, as depicted in **Scheme 3-1**. When oxygen availability at the active site is restricted, the linoleyl radical generated at the active site tends to dissociate from the enzyme and react in solution to form a mixture of 13S, 13R, 9S and 9R HPOD. Analogously, blocking oxygen delivery to the active site via mutagenesis is expected to result in increased radical dissociation and a corresponding increase in the amount of 13R, 9S, and 9R HPOD produced relative to the 13S isomer.

It is also possible that blocking the putative oxygen transport pathway leads oxygen to pursue an alternate route to the active site. In this case, the distribution of HPOD produced is expected to shift accordingly to reflect the pathway or pathways taken by oxygen. For example, if the alternate pathway leads oxygen to the opposite face of carbon 13, an increase in the proportion of 13R HPOD formed would be observed.

In summary, reaction regio- and stereospecificity provides an excellent handle with which to examine O_2 migration in wild-type SLO-1 and its mutant enzymes. A uniform increase in the proportion of 13R, 9S, and 9R HPOD produced is consistent with increased radical dissociation and occlusion of the O_2 delivery channel. On the other hand, an increase in any one or two of these alternate HPOD isomers alone is consistent with the ungating of an alternate channel in SLO-1 for O_2 delivery.

3.2 Materials and Methods

Mutagenesis
Seven SLO-1 mutants were generated through site-directed mutagenesis according to the QuickChange II protocol (Agilent Technologies). HPLC-purified primers were purchased from Eurofins MWG Operon. **Table 3-1** describes the forward and reverse primers employed in the generation of Ile553Trp, Leu496Phe, Leu496Trp, Ile547Phe, Ile547Trp, Val564Phe, and Val564Trp. XL1-Blue super competent cells (Agilent Technologies) were transformed for plasmid amplification. DNA mutation was confirmed by automated sequencing at the UC Berkeley Sequencing Facility.

SLO-1 Expression and Purification

Preparation of Non-His-tagged SLO-1
The SLO-1 Val564Phe mutant was expressed using the SLO-1 pT7-7 plasmid in *Escherichia coli* and purified as described previously. (*6*)

Preparation of His-tagged SLO-1
Wild-type SLO-1 and all remaining SLO-1 mutants were expressed using the pET-30Xa/LIC plasmid, acquired from Professor Betty Gaffney at Florida State University. These enzymes were expressed and purified as described previously, with several modifications. (*7*) The adapted protocol is described below.

The BL21-CodonPlus (DE3)-RIL strain of *Escherichia coli* (Agilent Technologies) was employed for SLO-1 expression. Overnight cultures in LB (37°C) were diluted 200-fold into 3 4-liter flasks, each containing 1.5 liters of TB, 50 μg/mL kanamycin, and 50 μg/mL chloramphenicol. Cultures were grown at 37°C until an $OD_{600} > 1.2$ was reached (4-5 hours), cooled to 14°C, induced with isopropyl 1-thio-β-D-galactopyranoside (0.1 mM), and grown for an additional 30 hours at 8°C. Cells were subsequently harvested and stored at -80°C until purification.

Cell paste from 4.5 L (25 g) was re-suspended in 100 mL lysis buffer—50 mM NaP_i (pH 8.0), 1x BugBuster (Novagen), 1250 units of benzonase (Novagen), 0.2 mM $MgSO_4$, 0.5 mM aminoethylbenzenesulfonyl fluoride, and 0.2 mg/mL of lysozyme. The lysis reaction was allowed to proceed for 40 minutes at room temperature followed by cooling at 4°C for 20 minutes. The suspension was subsequently clarified by centrifugation (18,600*g* in this and following steps). Solid ammonium sulfate was added to the supernatant to 30% of saturation. After 1 hour, a pellet was removed by centrifugation and the supernatant was brought to 60%-saturated ammonium sulfate. After 1 hour, the suspension was centrifuged and the supernatant discarded.

The 60% ammonium sulfate pellet was re-suspended in wash buffer—50mM NaP_i (pH 8.0), 500mM NaCl, 10% glycerol, and 20 mM imidazole—and immediately cycled twice through a prepared column of Ni-NTA resin (Novagen) equilibrated with the same buffer. The column was subsequently washed with 100 mL of wash buffer. His-tagged SLO-1 was eluted with wash

buffer containing 250 mM imidazole and dialyzed overnight (4°C) into 20mM Bis-Tris (pH 6.6) buffer.

The dialyzed eluate from Ni-NTA was concentrated and injected onto an FPLC system with a 6 mL UNO S6 column (Bio-Rad) for separation by cation exchange chromatography. A salt gradient for protein elution was run from 0.0 to 0.5 M NaCl in 20 mM Bis-Tris (pH 6.6) buffer. SLO-1 activity was assayed in fractions by monitoring the formation of HPOD at 234 nm upon the addition of 5 μL of a column fraction to 245 μL of 100 μM linoleic acid in 0.1 M Borate (pH 9.0). Fractions containing SLO-1 activity were combined, dialyzed into 0.1 M Borate (pH 9.0), concentrated, and stored at -80°C.

Kinetic Characterization

SLO-1 enzyme kinetics were analyzed by determining reaction rate at varying concentrations of linoleic acid (LA) and molecular oxygen. Parameters such as k_{cat}, K_M for LA, and K_M for molecular oxygen were determined by nonlinear least-squares fitting to the Michaelis-Menten equation:

$$v_0 = \frac{k_{cat}[S][E_{total}]}{K_M(S) + [S]}$$

The initial rate is reflected in v_0. $[E_{total}]$ represents total enzyme concentration and [S] is the concentration of the varied substrate, i.e. [LA] or $[O_2]$. (*3*, *4*)

Product Formation

Steady-state kinetics assays were performed on a Varian Cary 50 Bio UV-Vis spectrophotometer in single-wavelength mode, as described previously with minor modifications. (*8*) Reaction progress was monitored by following the generation of the product, hydroperoxyoctadecadienoic acid (HPOD) (ε_{234} = 23,600 M^{-1} cm^{-1}). (*9*) All assays were performed at 20°C and performed under ambient atmosphere in 0.1 M Borate (pH 9.0). Linoleic acid was purchased from Sigma and stock solutions (~500 μM) were prepared by diluting 0.5 mL of 40 mM linoleic acid in methanol into 40 mL of 0.1 M Borate (pH 9.0).

Kinetic assays were performed at 2-80 μM LA for wild-type SLO-1 and the six mutant enzymes studied here. Initial rates were fit in Kaleidagraph to the Michaelis-Menten equation in order to determine the first order rate constant (k_{cat}) as well as K_M(LA). In cases where substrate inhibition was observed, data points were omitted from the fitting.

Oxygen Consumption

The rate of oxygen consumption by wild-type SLO-1 and the six mutants studied here was monitored using a Clark-type electrode from Yellow Springs Inc. and a YSI-5300 biological oxygen monitor, as described previously with minor modifications. (*8*) One milliliter of 0.1 M Borate (pH 9.0) and LA was equilibrated in a thermally controlled water-jacketed cell at 20° C. The desired O_2 concentration was established by maintaining the appropriate O_2/N_2 mixture in the headspace above the LA solution for >10 minutes. The electrode was subsequently placed in

contact with the solution surface, eliminating the headspace. The reaction was initiated by injecting a similarly buffered solution of SLO-1.

Kinetic assays were performed at 30-1365 μM O_2 for wild-type SLO-1 and the six mutant enzymes studied here. Initial rates were fit in Kaleidagraph to the Michaelis-Menten equation in order to determine the first order rate constant (k_{cat}) as well as $K_M(O_2)$. Reported estimates of k_{cat} are derived from these oxygen electrode studies rather than UV kinetic data, since the former correct for saturating O_2.

Assessment of HPOD Distribution

Incubation and Extraction of SLO-1 Reaction

The distribution of HPOD isomers generated was assessed for the reaction of linoleic acid with wild-type SLO-1 and the six mutants studied here. Reactions at ambient atmosphere were incubated at 20°C in 0.1M Borate (pH 9.0) and 100 μM LA for 5 hours after initiation with enzyme. The reaction mixtures were subsequently quenched via acidification to pH 4 with glacial acetic acid and extracted into dichloromethane. Reaction products were taken to dryness under a stream of N_2 and stored at -80°C until HPLC analysis.

Reactions at elevated and depressed O_2 concentrations were performed using a Clark-type electrode from Yellow Springs Inc. and a YSI-5300 biological oxygen monitor. Two milliliters of 0.1 M Borate (pH 9.0) and 100 μM LA were equilibrated in a thermally controlled water-jacketed cell at 20° C. The desired O_2 concentration was established by maintaining the appropriate O_2/N_2 mixture in the headspace above the LA solution for >10 minutes. The electrode was subsequently placed in contact with the solution surface, eliminating the headspace. The reaction was initiated by injecting a similarly buffered solution of SLO-1 and incubated in the cell until quenching by acidification with N_2-saturated acetic acid. Reaction products were extracted into dichloromethane, taken to dryness under N_2, and stored at -80°C until HPLC analysis.

HPLC Analysis

A three-step protocol was employed to identify the distribution of HPOD isomers generated by the reaction of SLO-1 and its mutants with linoleic acid. HPOD was purified from the reaction mixture by reverse phase HPLC. Triphenylphosphine was used to reduce purified HPOD to the corresponding alcohol—hydroxyoctadecadienoic acid (HODE). The HODE generated was subsequently analyzed by chiral phase HPLC and the isomeric distribution determined.

Reaction products for wild-type SLO-1 and its mutant enzymes were injected onto a reverse phase HPLC system with a Luna C18 5-μm column (0.46 x 25 cm, Phenomenex). An isocratic solvent system of 78% methanol and 21.9% water with 0.1% acetic acid was employed in order to elute HPOD. A flow rate of 0.9 mL/minute was used. HPOD was collected, taken to dryness under N_2, and reduced via incubation for >1 hour with a solution of 1.9 mM triphenylphosphine in methanol. The HODE generated was taken to dryness under N_2 and stored at -80°C until chiral phase HPLC analysis.

HODE was injected onto a chiral phase HPLC system with a Chiralcel OD-3 column (0.46 x 25 cm, Chiral Technologies, Inc.). An isocratic solvent system of 1.55% isopropanol, 0.3% acetic acid, and 98.2% hexanes was employed in order to separate the 13S, 13R, 9S, and 9R isomers. A flow rate of 2 mL/minute was used. Assignment of the four HODE isomeric peaks was accomplished using standards of 13S, 13R, 9S, and 9R HODE acquired from Cayman Chemical. A chiral phase HPLC trace featuring these standards is depicted in **Figure 3-1**.

3.3 Results

Bottleneck residues of channel were mutated to introduce bulk and disrupt oxygen transport. One channel and four bottleneck residues— Ile^{553}, Ile^{547}, Leu^{496}, and Val^{564}—were implicated in tuning oxygen access to the active site based on computational studies. In order to confirm the functional role of the putative oxygen channel, bulk was introduced at its bottleneck residues via site-directed mutagenesis to phenylalanine and tryptophan. A His-tagged construct was purified and kinetically characterized for wild-type SLO-1 and mutant enzymes other than Val564Phe. **Table 3-2** confirms that the wild-type His-tagged enzyme reproduces the behavior of non-His-tagged SLO-1with respect to published kinetic parameters.

Kinetic characterization of the mutants was performed to probe changes in oxygen migration. The effect of mutations on the oxygen conductivity of the pathway was evaluated by determining k_{cat}, $K_M(O_2)$, and $K_M(LA)$. These parameters are summarized for the wild-type and mutant enzymes in **Table 3-3**. The Ile553Phe SLO-1 mutant had been previously studied in the Klinman group; published parameters for this mutant are included in **Table 3-3**.

Unaffected $K_M(O_2)$ suggests that introducing bulk at Ile^{547} & Val^{564} doesn't impact O_2 delivery. Introducing bulk at Ile^{547} and Val^{564} does not appear to impede oxygen transport to the active site of SLO-1. Mutant enzymes with phenylalanine and tryptophan at positions 547 or 564 exhibit Michaelis constants for oxygen in a range from 32 to 50 μM O_2—similar to that of wild-type SLO-1, 38 μM O_2. $K_M(LA)$ values for these mutants were found to be slightly lower than that of wild-type SLO-1, ranging from 3-8 μM LA compared to 20 μM LA for wild-type. Ile^{547} and Val^{564} mutants also exhibit decreases in k_{cat} in the range of 2- to 5-fold.

Increased $K_M(O_2)$ suggests that introducing bulk at Ile^{553} & Leu^{496} impedes oxygen transport. Introducing bulk at Ile^{553} and Leu^{496} appears to impede oxygen transport to the active site of SLO-1. Mutant enzymes with phenylalanine and tryptophan at positions 553 or 496 exhibit increased Michaelis constants for oxygen in a range from 132 to 744 μM O_2—substantially greater than that of wild-type SLO-1, 38 μM O_2. Consistent with this observation, $k_{cat}/K_M(O_2)$ values for the Ile^{553} and Leu^{496} mutants are significantly decreased, from 6 s^{-1} μM^{-1} O_2 for wild-type SLO-1 to between 0.7 and 0.0005 s^{-1} μM^{-1} O_2 for the mutants. It is interesting to note that the increase in $K_M(O_2)$ and decrease in $k_{cat}/K_M(O_2)$ are more dramatic in each tryptophan mutant when compared to the analogous phenylalanine mutant, consistent with tryptophan residues providing additional bulk.

$K_M(LA)$ values for Ile^{553} and Leu^{496} mutants were found to be similar to that of wild-type SLO-1, ranging from 5 to 25 μM LA compared to 20 μM LA for wild-type. Since the primary kinetic isotope effect of these mutants has not been determined, it is difficult to evaluate how close $K_M(LA)$ is to K_d in these mutants. The introduction of space-filling residues at positions 553 and 496 also resulted in a decreased k_{cat}, particularly in the case of the tryptophan mutants. Ile553Trp and Leu496Trp exhibit k_{cat} values that are reduced by three and two orders of magnitude, respectively.

HPOD distribution was analyzed in mutants to probe changes in oxygen migration.
In addition to parameters such as $K_M(O_2)$**,** the regio- and stereospecificity of the SLO-1-catalyzed reaction also reports on oxygen targeting to the active site. To demonstrate the effect of reducing O_2 availability at the active site on SLO-1 regio- and stereospecificity, the wild-type reaction was performed and analyzed under ambient (284 μM O_2) and reduced oxygen (28 μM O_2) conditions. The distribution of HPOD isomers produced at each oxygen concentration was determined via chiral HPLC analysis and is detailed in **Figure 3-2**. At ambient oxygen, the wild-type SLO-1 reaction produces >90% 13S HPOD. 13R, 9S, and 9R HPOD are presented in small amounts and account in total for <10% of HPOD produced. At 28 μM O_2, by contrast, a substantial amount of 13R, 9S, and 9R HPOD is generated—together these isomers account for >60% of HPOD produced. It is clear that under oxygen-deprived circumstances, the regio- and stereospecificity of the SLO-1 reaction is disrupted. A decrease of 10-fold in oxygen concentration is able to reduce the amount of 13S HPOD produced dramatically.

The effect of mutations on oxygen trafficking was evaluated by determining the regio- and stereospecificity of reactions catalyzed by the mutant enzymes. The distribution of HPOD isomers produced by reaction of LA with each enzyme is detailed in **Table 3-4**. The Ile553Phe SLO-1 mutant had been previously studied in the Klinman group; published parameters for this mutant are included in **Table 3-4**.

Unchanged HPOD distribution in Ile^{547} & Val^{564} reflects no perturbation of oxygen migration.
Introducing bulk at Ile^{547} and Val^{564} does not appear to impede oxygen transport to the active site of SLO-1. Mutant enzymes with phenylalanine and tryptophan at positions 547 or 564 catalyze reactions with regio- and stereospecificity comparable to that of the wild-type reaction. Ile^{547} and Val^{564} mutants react with LA to produce between 86% and 93% 13S HPOD, similar to the wild-type enzyme, which generates 93% 13S HPOD. The total proportion of 13R, 9S, and 9R HPOD generated does not exceed 15% for any Ile^{547} or Val^{564} mutant. The unchanged regio- and stereochemistry of the Ile^{547} and Val^{564} mutant reactions is consistent with the unchanged $K_M(O_2)$ for these mutants.

Disrupted HPOD distribution in Ile553Trp reaction suggests that oxygen transport is impeded.
Introducing bulk at Ile^{553} appears to impede oxygen transport to the active site of SLO-1. Regio- and stereospecificity is dramatically disrupted in the reaction of the Ile553Trp mutant with LA. Reaction with the Ile553Trp mutant produces 45% 13S HPOD, while reaction with the wild-type enzyme generates 93% 13S HPOD. A substantial amount of 13R, 9S, and 9R HPOD is generated—together these isomers account for >50% of HPOD produced. Consistent with impaired oxygen delivery, the regio- and stereospecificity of the Ile553Trp mutant resembles that of the wild-type reaction at low O_2. The altered regio- and stereochemistry of the Ile553Trp mutant reaction is also consistent with the dramatically elevated $K_M(O_2)$ determined for this mutant (744 μM O_2).

It is interesting to note that introducing phenylalanine at position 553 does not disrupt regio- and stereospecificity in the same way as tryptophan. Despite exhibiting an elevated $K_M(O_2)$, the Ile553Phe mutant produces >90% 13S HPOD. The introduction of phenylalanine at position 553 may disrupt oxygen access to some extent, but not to the extent that is required to alter the regio- and stereospecificity of the reaction.

Disrupted HPOD distribution in Leu^{496} mutant reactions reflects perturbed oxygen trafficking. Introducing bulk at Leu^{496} appears to disrupt oxygen transport to the active site of SLO-1. Regio- and stereospecificity is dramatically disrupted in the reaction of both Leu^{496} mutants with LA. Reaction with the phenylalanine and tryptophan mutants produces 63% and 31% 13S HPOD, respectively, while reaction with the wild-type enzyme generates 93% 13S HPOD. A substantial amount of 13R, 9S, and 9R HPOD is generated—together these isomers account for 37% and 69% of HPOD produced in reactions with Leu496Phe and Leu496Trp, respectively.

It is interesting to note that the 13R, 9S and 9R are not produced in equal amounts, as is the case with wild-type SLO-1 at low oxygen or the Ile553Trp mutant. This is particularly obvious for the Leu496Trp mutant, where the 9S and 9R isomers each account for 29% and 30% of HPOD produced compared to 10% for the 13R isomer. The disparity is subtler in the case of Leu496Phe, where the 9S and 9R isomers account for 14% of HPOD produced compared to 9% for 13R HPOD. The altered regio- and stereochemistry of the Leu^{496} mutant reactions suggests that these mutations may disrupt oxygen targeting to the active site by a different mechanism than is operating in the Ile553Trp mutant or wild-type at low O_2.

Increased [O_2] partially rescues HPOD distribution in the Ile553Trp reaction with LA. Ile553Trp displays an elevated $K_M(O_2)$ and altered regio- and stereospecificity, suggesting that oxygen transport to the active site is impeded in this mutant. The Ile553Trp reaction was performed at an elevated O_2 concentration (1365 μM O_2) in order to determine if additional O_2 could restore the wild-type HPOD distribution. Increasing [O_2] from 284 μM to 1365 μM indeed reduces the amount of 13R, 9S, and 9R isomers generated from 55% to 35% of HPOD produced. The amount of 13S HPOD generated by the Ile553Trp reaction increases from 45% at ambient O_2 to 65% at 1365 μM O_2. See **Figure 3-3**. Increased O_2 appears to partially restore the regio- and stereospecificity of the mutant reaction, consistent with additional O_2 compensating for impaired oxygen delivery in the mutant.

Increased [O_2] partially rescues HPOD distribution in the Leu496Trp reaction with LA. Like Ile553Trp, Leu496Trp displays an elevated $K_M(O_2)$ and altered regio- and stereospecificity, suggesting that oxygen transport to the active site of SLO-1 is disrupted in this mutant. The Leu496Trp reaction was performed at an elevated O_2 concentration (1365 μM O_2) in order to determine if additional O_2 could restore the wild-type HPOD distribution. As in the case of Ile553Trp, increasing [O_2] from 284 μM to 1365 μM reduces the amount of 9S and 9R HPOD isomers generated and increases the amount of 13S HPOD produced. The amount of 13R HPOD generated by Leu496Trp remains constant at high O_2, however, while it decreases in the Ile553Trp reaction at high O_2. See **Figure 3-4**.

Increased O_2 appears to partially restore the regio- and stereospecificity of the Leu496Trp mutant reaction, but not by uniformly decreasing the amount of 13R, 9S and 9R isomers produced, as in the case of Ile553Trp. The altered regio- and stereochemistry of the Leu496Trp mutant reaction at high O_2 is consistent with our hypothesis that mutations at this position disrupt oxygen trafficking by a different mechanism than is operating in the Ile553Trp mutant.

3.4 Discussion

Computational studies implicated one channel and four bottleneck residues— Ile^{553}, Ile^{547}, Leu^{496}, and Val^{564}—in tuning oxygen access to the active site. The functional role of this putative oxygen channel was confirmed by introducing bulk at its bottleneck residues via site-directed mutagenesis. Introducing bulk at two positions—Ile^{553} and Leu^{496}—disrupted oxygen trafficking to the active site, resulting in elevated $K_M(O_2)$ values and an altered distribution of HPOD isomers produced. See **Tables 3-3** and **3-4**. These observations point to an important role for these residues and the channel in guiding O_2 to the active site of SLO-1.

Both $K_M(O_2)$ and reaction regio- and stereospecificity provide insight into oxygen targeting to the active site of SLO-1. $K_M(O_2)$ reflects the concentration of oxygen at which the rate of reaction is half-maximal. Elevated $K_M(O_2)$ values are associated with restricted access of oxygen to the active site. Reaction regio- and stereospecificity also reports on oxygen availability at the active site. At ambient oxygen, the reaction of wild-type SLO-1 and LA produces >90% 13S HPOD. At low O_2, by contrast, 45% 13S HPOD is produced and approximately 18% of each alternate isomer (13R, 9S, and 9R) is generated. See **Figure 3-2**. This loss of regio- and stereospecificity has been previously documented and is driven by the dissociation of the substrate radical. When oxygen availability at the active site is restricted, the linoleyl radical tends to fall off the enzyme and into solution, where it can react in a non-specific manner with O_2 to yield a mixture of 13S, 13R, 9S and 9R HPOD. See **Scheme 3-1**.

Residues Ile^{553} and Leu^{496} were validated as gatekeepers along the oxygen transport pathway identified to the SLO-1 active site. Introducing bulk at these positions disrupts oxygen trafficking as evidenced by the 4 to 20-fold increases in the $K_M(O_2)$ observed for Ile553Phe, Ile553Trp, Leu496Phe, and Leu496Trp. The tryptophan mutants exhibit the largest $K_M(O_2)$ values—744 μM O_2 for Ile553Trp and 171 μM O_2 for Leu496Trp. See **Table 3-3**. This observation is consistent with tryptophan's additional bulk being better able block the putative pathway.

Assessing the regio- and stereospecificity of the Ile^{553} and Leu^{496} mutant reactions reveals that mutations at both of these residues disrupt oxygen trafficking, albeit in different ways. The Ile553Trp reaction exhibits impaired regio- and stereospecificity similar to the reaction of wild-type SLO-1 at low oxygen. A substantial amount of 13R, 9S, and 9R HPOD is produced—these isomers account for >50% of HPOD generated and are produced in roughly equivalent amounts, as detailed in **Table 3-4**. This observation, together with the elevated $K_M(O_2)$ determined for the Ile553Trp mutant, reflects restricted oxygen availability at the active site and increased dissociation of the linoleyl radical. Consistent with this hypothesis, performing the Ile553Trp mutant reaction at high [O_2] partially restores the wild-type regio- and stereospecificity of the reaction. The amount of 13S HPOD generated by the Ile553Trp reaction increases from 45% at ambient O_2 to 65% at 1365 μM O_2, as shown in **Figure 3-3**.

It is interesting to note that introducing phenylalanine at position 553 does not disrupt regio- and stereospecificity in the same way as tryptophan. Despite exhibiting an elevated $K_M(O_2)$, the Ile553Phe mutant produces >90% 13S HPOD. The introduction of phenylalanine at position 553

may disrupt oxygen access to some extent, but not to the extent that is required to alter the regio- and stereospecificity of the reaction, as shown in **Table 3-4**.

Introducing bulk at Leu^{496} disrupts oxygen trafficking to the active site of SLO-1 primarily by ungating another route for O_2 migration. As in the Ile553Trp reaction, a substantial amount of 13R, 9S, and 9R HPOD is produced in Leu^{496} mutants—together these isomers account for 37% and 69% of HPOD produced in reactions with Leu496Phe and Leu496Trp, respectively. However, the 13R, 9S and 9R are not produced in equal amounts, as is the case with the Ile553Trp mutant and wild-type SLO-1 at low oxygen. This is particularly obvious for the Leu496Trp mutant, where the 9S and 9R isomers each account for 29% and 30% of HPOD produced compared to 10% for the 13R isomer. See **Table 3-4**. The altered regio- and stereochemistry of the Leu^{496} mutant reactions thus cannot be directly explained by restricted availability of O_2 at the active site leading to loss of the substrate radical. The increased proportion of 9R and 9S HPOD generated is consistent with the Leu^{496} mutations ungating another route for gas migration that allows O_2 to access carbon 9 of the substrate radical.

Increasing $[O_2]$ from 284 μM to 1365 μM partially restores the wild-type regio- and stereospecificity of the Leu496Trp reaction by increasing the proportion of 13S HPOD produced from 32% to 44% and decreasing the proportion of 9S and 9R HPOD generated from 59% to 45%. Performing the Leu496Trp reaction at high O_2 does not influence the amount of 13R HPOD produced, however. See **Figure 3-4**. This observation suggests that increasing $[O_2]$ does not simply increase oxygen availability at the active site and reduce radical dissociation, as in the case of Ile553Trp at high O_2. Such a decrease in radical dissociation would affect the 13R, 9S, and 9R isomers uniformly. Rather, increasing $[O_2]$ appears to influence the partitioning of O_2 between oxygen transport pathways leading to carbon 13 and carbon 9. At higher O_2, for example, more oxygen appears to be proceeding through the pathway leading to carbon 13 compared to carbon 9. This observation is consistent with the channel leading to carbon 13 having a higher $K_M(O_2)$ than the channel leading to carbon 9.

In summary, introducing bulk at channel bottleneck residues Ile^{553} and Leu^{496} disrupts oxygen trafficking to the SLO-1 active site. The Ile553Trp and Leu496Trp mutants, in particular, exhibit elevated $K_M(O_2)$ values and produce a dramatically altered distribution of HPOD isomers. Interestingly, each of these mutations disrupts oxygen trafficking in a different way. The Ile553Trp mutant exhibits a remarkably elevated $K_M(O_2)$ and essentially behaves as the wild-type enzyme at low oxygen. Oxygen availability at the Ile553Trp active site is highly restricted and substantial amounts of 13R, 9S, and 9R HPOD are produced in solution due to linoleyl radical dissociation. The Leu496Trp mutant, by contrast, exhibits a $K_M(O_2)$ that, while elevated compared to wild-type, is approximately 4-fold lower than that of Ile553Trp. Oxygen access is restricted at the Leu496Trp active site but does not drive the mutant's dramatically altered regio- and stereospecificity. Rather, the Leu496 mutation ungates an alternate route that allows oxygen to access carbon 9 of the substrate radical, thereby increasing the proportion of 9R and 9S (but not 13R) HPOD produced. Together, these mutagenesis studies support a functional role for the putative channel in facilitating oxygen delivery to the appropriate location in the active site, thereby ensuring reaction regio- and stereospecificity.

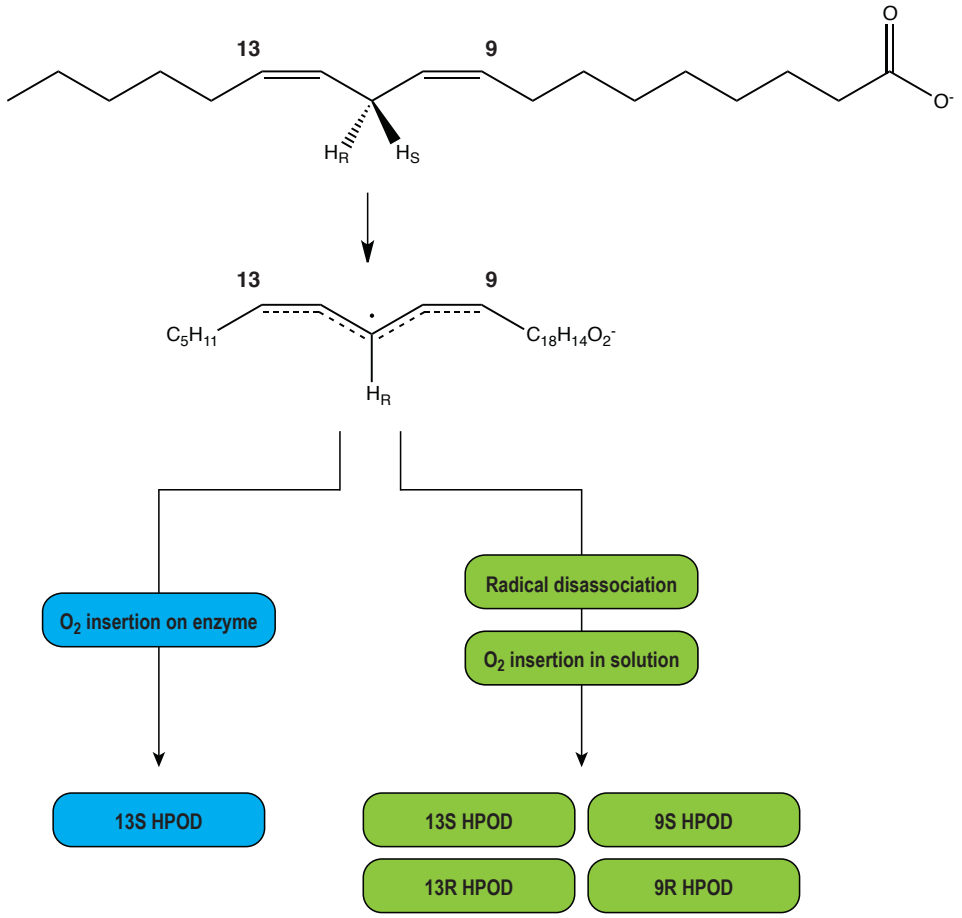

Scheme 3-1. SLO-1 catalyzed peroxidation of linoleic acid under conditions of low oxygen. Disrupted regio- and stereospecificity at low oxygen is driven by radical dissociation. At ambient oxygen, oxygen insertion occurs on the enzyme and produces primarily 13S HPOD. At low oxygen, a portion of the linoleyl radical is trapped by oxygen on the enzyme and generates 13S HPOD (blue). A portion of the linoleyl radical, however, also dissociates from the enzyme and reacts in solution to form a mixture of 13S, 13R, 9S and 9R HPOD (green).

Mutant Enzyme	Forward and reverse primers (5' to 3')
Ile553Trp	CTAATTAATGCTAATGGCATATGGGAGACAACCTTTTTGCCCTC
	GAGGGCAAAAAGGTTGTCTCCCATATGCCATTAGCATTAATTAG
Leu496Phe	CTTGCTACCATCAATTCATGAGCCATTGG
	CCAATGGCTCATGAATTGATGGTAGCAAG
Leu496Trp	GACTCTTGCTACCATCAATGGATGAGCCATTGGTTAAATAC
	GTATTTAACCAATGGCTCATCCATTGATGGTAGCAAGAGTC
Ile547Phe	CTTGCCAGGCAATCTCTATTTAATGCTAATGGC
	GCCATTAGCATTAAATAGAGATTGCCTGGCAAG
Ile547Trp	CACTTGCCAGGCAATCTCTATGGAATGCTAATGGCATAATAG
	CTATTATGCCATTAGCATTCCATAGAGATTGCCTGGCAAGTG
Val564Phe	GCCCTCAAAGTATTCTTTTGAGATGTCTTCGGCGG
	CCGCCGAAGACATCTCAAAAGAATACTTTGAGGGC
Val564Trp	CCCTCAAAGTATTCTTGGGAGATGTCTTCGGCG
	CGCCGAAGACATCTCCCAAGAATACTTTGAGGG

Table 3-1. Forward and reverse primers employed for site-directed mutagenesis of SLO-1. For each enzyme mutant, the forward and reverse primers are provided in the 5' to 3' direction.

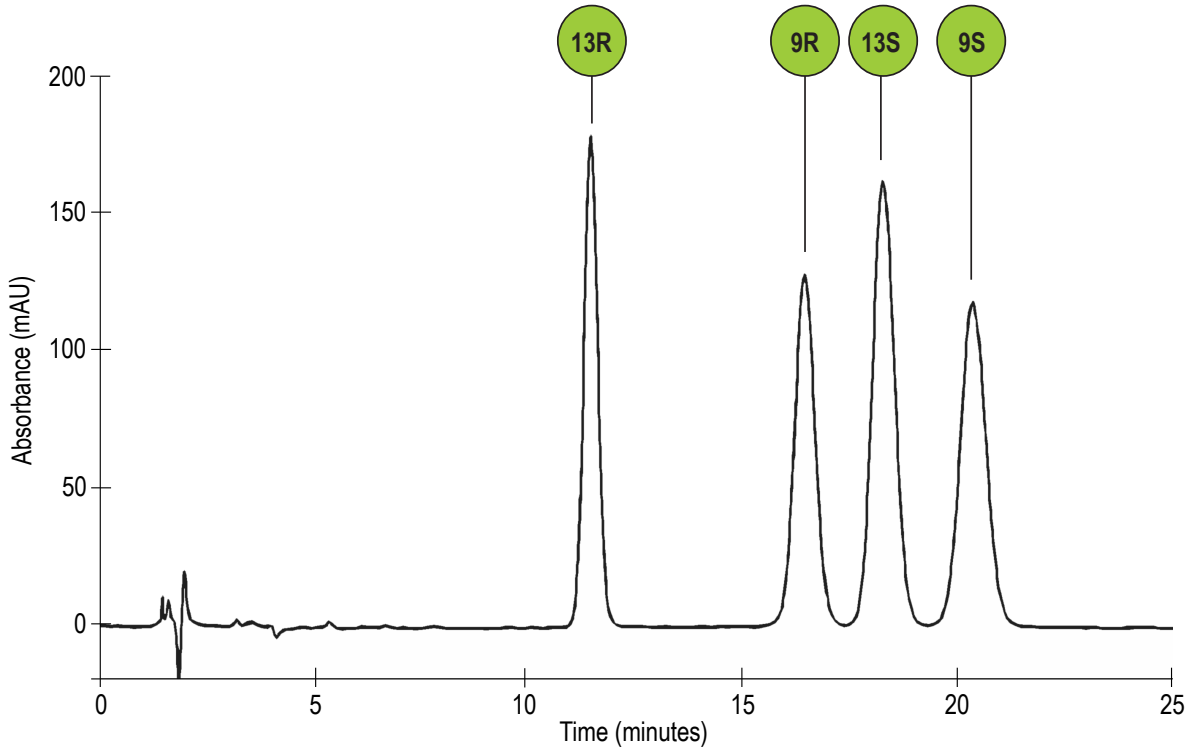

Figure 3-1. Chiral phase HPLC trace featuring 13S, 13R, 9S, and 9R HODE. Assignment of the four HODE isomeric peaks was accomplished using standards of 13S, 13R, 9S, and 9R HODE acquired from Cayman Chemical.

SLO-1	k_{cat} [s^{-1}]	K_M (LA) [μM]	K_M (O_2) [μM]
Non-His-tagged*	230±15	18 ± 3	31 ± 3
His-tagged	211 ± 9	20 ± 2	38 ± 5

*(*3*)

Table 3-2. Comparison of kinetic parameters for non-His-tagged and His-tagged SLO-1.

SLO-1	k_{cat} [s^{-1}]	K_M (LA) [μM]	K_M (O_2) [μM]
WT	211 ± 9	20 ± 2	38 ± 5
Ile553Phe*	102 ± 8	19 ± 4	142 ± 58
Ile553Trp	0.40 ± 0.04	25 ± 5	744 ± 142
Ile547Phe	66 ± 5	3.0 ± 0.3	44 ± 11
Ile547Trp	44 ± 2	5.0 ± 0.5	50 ± 7
Leu496Phe	44 ± 3	5 ± 1	132 ± 26
Leu496Trp	1.6 ± 0.1	11.0 ± 0.8	171 ± 33
Val564Phe	60 ± 1	6.0 ± 0.4	46 ± 5
Val564Trp	99 ± 5	8.0 ± 0.7	32 ± 6

*(*3*)

SLO-1	k_{cat}/K_M (LA) [s^{-1} $μM^{-1}$]	k_{cat}/K_M (O_2) [s^{-1} $μM^{-1}$]
WT	11 ± 1	6 ± 1
Ile553Phe*	5 ± 1	0.7 ± 0.3
Ile553Trp	0.016 ± 0.004	0.0005 ± 0.0001
Ile547Phe	22 ± 3	1.5 ± 0.4
Ile547Trp	9 ± 1	0.9 ± 0.1
Leu496Phe	9 ± 2	0.3 ± 0.1
Leu496Trp	0.15 ± 0.01	0.009 ± 0.002
Val564Phe	10 ± 1	1.3 ± 0.1
Val564Trp	12 ± 1	3 ± 1

*(*3*)

Table 3-3. Kinetic characterization of wild-type SLO-1 and its channel mutants.

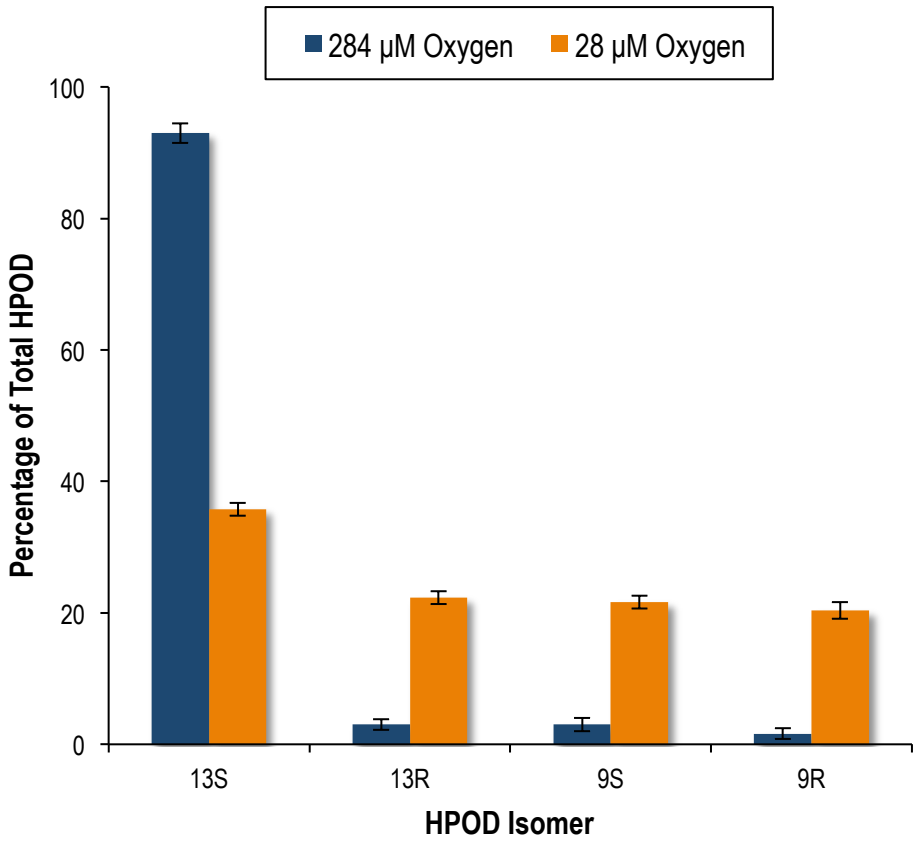

Figure 3-2. HPOD isomer distribution for wild-type SLO-1 reaction at 284 and 28 µM O_2.

SLO-1	13S HPOD (%)	13R HPOD (%)	9S HPOD (%)	9R HPOD (%)
WT	93	3	3	2
Ile553Phe*	95	2	1	2
Ile553Trp	45 ± 8	16	22 ± 3	17
Ile547Phe	93	2	2	2
Ile547Trp	93	2	3	2
Leu496Phe	63	9	14	14
Leu496Trp	32	10	29	30
Val564Phe	89	2	4	5
Val564Trp	86 ± 3	3	5	5

*(*3*)

Table 3-4. Characterization of HPOD distribution for wild-type SLO-1 and its channel mutants. Error ≤ 2 unless noted above.

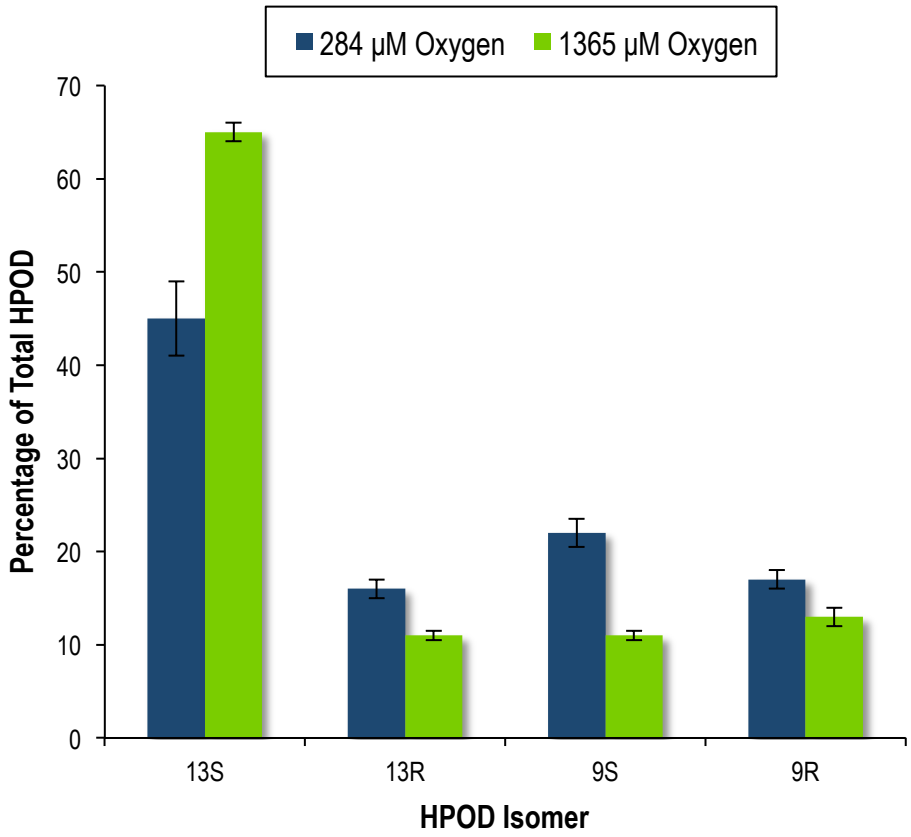

Figure 3-3. HPOD isomer distribution for Ile553Trp SLO-1 reaction at 284 and 1365 µM O_2.

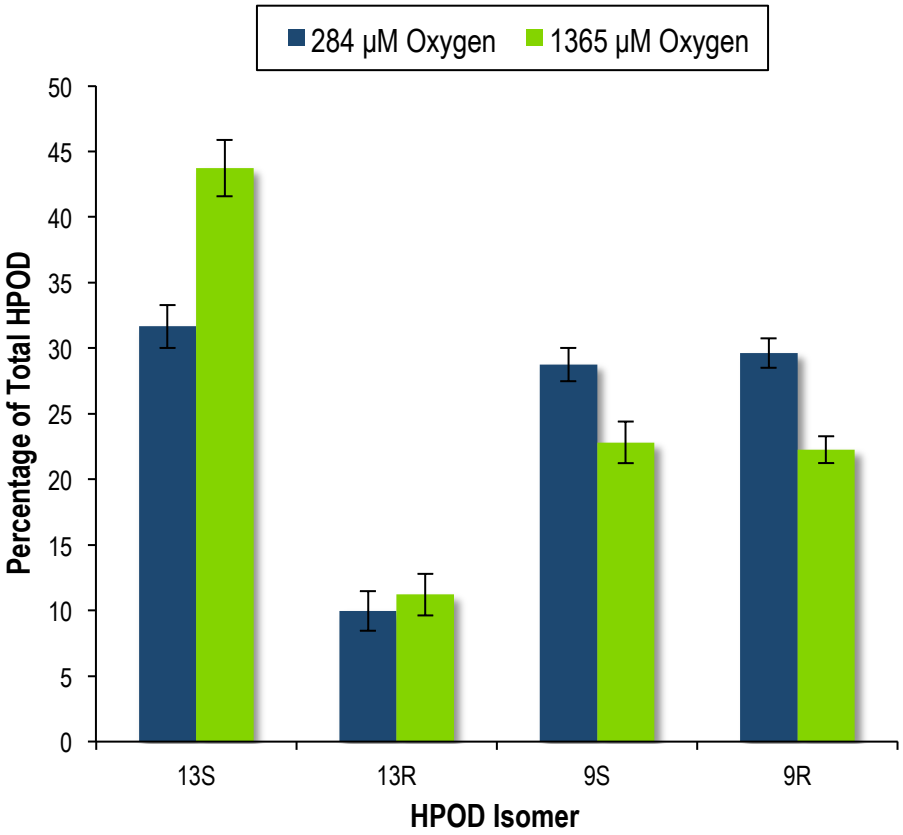

Figure 3-4. HPOD isomer distribution for Leu496Trp SLO-1 reaction at 284 and 1365 µM O_2.

References

1. Ivanov, I., Heydeck, D., Hofheinz, K., Roffeis, J., O'Donnell, V. B., Kuhn, H., and Walther, M. (2010) Molecular enzymology of lipoxygenases, *Archives of Biochemistry and Biophysics 503*, 161–174.
2. Minor, W., Steczko, J., Boguslaw Stec, O., Otwinowski, Z., Bolin, J. T., Walter, R., and Axelrod, B. (1996) Crystal structure of soybean lipoxygenase L-1 at 1.4 Å resolution, *Biochemistry 35*, 10687–10701.
3. Knapp, M. J., and Klinman, J. P. (2003) Kinetic Studies of Oxygen Reactivity in Soybean Lipoxygenase-1, *Biochemistry 42*, 11466–11475.
4. Fersht, A. (1985) Enzyme Structure and Mechanism, *W. H. Freeman, New York*.
5. Knapp, M. J., Seebeck, F. P., and Klinman, J. P. (2001) Steric Control of Oxygenation Regiochemistry in Soybean Lipoxygenase-1, *J. Am. Chem. Soc. 123*, 2931–2932.
6. Meyer, M. P., and Klinman, J. P. (2011) Investigating inner-sphere reorganization via secondary kinetic isotope effects in the C-H cleavage reaction catalyzed by soybean lipoxygenase: tunneling in the substrate backbone as well as the transferred hydrogen., *J. Am. Chem. Soc. 133*, 430–439.
7. Coffa, G., Schneider, C., and Brash, A. R. (2005) A comprehensive model of positional and stereo control in lipoxygenases, *Biochemical and Biophysical Research Communications 338*, 87–92.
8. Meyer, M. P., Tomchick, D. R., and Klinman, J. P. (2008) Enzyme structure and dynamics affect hydrogen tunneling: The impact of a remote side chain (I553) in soybean lipoxygenase-1, *Proceedings of the National Academy of Sciences 105*, 1146–1151.
9. Rickert, K. W., and Klinman, J. P. (1999) Nature of Hydrogen Transfer in Soybean Lipoxygenase 1: Separation of Primary and Secondary Isotope Effects, *Biochemistry 38*, 12218–12228.

Chapter 4

Effect of Diminishing O_2 Availability on SLO-1 Activation

4.1 Introduction

Investigation of Activation Products

SLO-1 catalyzes the regio- and stereospecific insertion of oxygen into linoleic acid to yield a chiral hydroperoxide, 13S HPOD. In this work, computational studies and site-directed mutagenesis were used to define an oxygen channel responsible for delivering the small, hydrophobic gas to the SLO-1 active site. Introducing bulk into this channel alters the kinetics as well as regio- and stereospecificity of oxygen insertion. Oxygen access to the active site was most diminished in the Ile553Trp mutant, which will serve as the focus for this chapter.

As discussed in **Chapter 1**, activation of SLO-1 from Fe^{2+} to Fe^{3+} by HPOD is required for reaction with linoleic acid. (*1*, *2*) Diminished [O_2] has significant implications for the reaction of ferrous SLO-1 with HPOD, reducing activation efficiency and altering the identity of activation products. (*3*) It is expected that since the Ile553Trp mutation diminishes oxygen availability at the active site, it would also impact the activation process. The product profile generated by Ile553Trp's reaction with LA was examined using both mass spectrometry and NMR to demonstrate that activation by HPOD is altered for this mutant enzyme, as it is for wild-type under diminished O_2.

Activation at Ambient O_2

Prior to reacting with linoleic acid, ferrous SLO-1 must be activated to ferric SLO-1 by reaction with HPOD. At ambient oxygen, activation is an efficient, single turnover process yielding ferric SLO-1 and minute amounts of epoxyallylic hydroperoxides. This process is described in **Part I** of **Figure 4-1**. First, the ferrous enzyme reacts with HPOD to produce an epoxyallylic radical intermediate bound to the ferric enzyme. The radical dissociates after reacting with oxygen, forming an epoxyallylic hydroperoxide in solution and leaving the ferric enzyme activated for reaction with LA. Notably, because of the single turnover nature of activation at ambient O_2, negligible amounts of these epoxyallylic compounds are produced. (*3*, *4*)

Anaerobic Activation

The anaerobic reaction of 13S HPOD and SLO-1 has been extensively studied. (*5*-*8*) Under anaerobic conditions, SLO-1 activation is less efficient and the enzyme displays hydroperoxide isomerase activity. In the absence of oxygen, the epoxyallylic radical generated by the reaction of ferrous SLO-1 and HPOD participates in two distinct processes, one that results in enzyme activation and one that does not. In the former, the epoxyallylic radical dissociates, dimerizing and leaving the ferric enzyme activated for reaction with LA. In the latter, the epoxyallylic radical remains bound to the enzyme and re-reduces ferric SLO-1 to its inactive ferrous state. This process, which is not observed at ambient O_2, produces epoxyalcohols and ketones and represents the hydroperoxide isomerase reactivity of SLO-1. See **Part II** of **Figure 4-1**. In sum, the reaction of SLO-1 and HPOD under anaerobic conditions yields a mixture of lipid dimers, epoxyalcohols and ketones. (*3*)

Activation of Ile553Trp SLO-1

As reviewed above, studies of aerobic and anaerobic SLO-1 activation show that reducing [O_2] decreases the efficiency of activation. In the absence of oxygen, for example, only a portion of the SLO-1 that reacts with HPOD is left in its activated, ferric state while much of the enzyme is

returned to its inactive, ferrous state. The product distribution of the enzyme's reaction with HPOD also changes in the absence of O_2—producing lipid dimers, epoxyalcohols, and ketones, rather than the epoxyallylic hydroperoxides generated at ambient O_2. (*3*) Since the Ile553Trp mutation diminishes oxygen availability at the active site, it is our hypothesis that this mutant enzyme undergoes inefficient activation and reacts with HPOD in a way that mimics wild-type SLO-1 in the absence of O_2. One important caveat here is that the aerobic Ile553Trp reaction may not form the dimers that are observed in the anaerobic wild-type reaction. This is because the portion of epoxyallylic radical that dissociates from the Ile553Trp mutant can immediately encounter oxygen in solution and form epoxyallylic hydroperoxides.

In short, it is our hypothesis that diminished O_2 availability drives inefficient activation in Ile553Trp SLO-1 and that, accordingly, the products of Ile553Trp activation by HPOD consist of epoxyallylic hydroperoxides as well as epoxyalcohols and ketones. A proposed scheme for the reactivity of Ile553Trp SLO-1 and HPOD at ambient O_2 is described in detail in **Part III** of **Figure 4-1**.

Reaction of Ile553Trp SLO-1 with LA

The validity of the activation scheme proposed for the Ile553Trp mutant in **Part III** of **Figure 4-1** can be assessed by studying the enzyme's reaction with LA. If activation by HPOD is impaired in the mutant as we hypothesize, it is expected that the product profile of the Ile553Trp reaction with LA would include alternate activation products—epoxyalcohols and ketones—in addition to epoxyallylic hydroperoxides.

It is important to note that diminished O_2 not only decreases the efficiency of activation by HPOD, but also influences the reaction of the enzyme with LA. As reviewed in **Chapter 3**, reduced O_2 availability drives increased linoleyl dissociation in the reaction of Ile553Trp with LA. Increased linoleyl radical dissociation, in turn, translates into increased quantities of activation products since each time the linoleyl radical dissociates, the enzyme is left in the inactive ferrous state and must be reactivated by HPOD. Consequently, it is expected that restricted oxygen availability will drive the formation of significant quantities of activation products in the Ile5553Trp reaction with LA.

In summary, the product distribution of the reaction of Ile553Trp SLO-1 and LA can be analyzed to determine to what extent perturbing oxygen trafficking can impede enzyme activation. Activation products generated in the mutant reaction with LA can be identified and compared to the products of SLO-1 activation under anaerobic conditions.

4.2 Materials and Methods

Incubation and Extraction of SLO-1 Reaction

Reactions were performed as discussed previously in **Chapter 3**. Reactions at ambient atmosphere were incubated at 20°C in 0.1 M Borate (pH 9.0) and 100 μM LA for 5 hours after initiation with enzyme. Reactions performed to generate samples for NMR analysis were performed with $^{13}C_{18}$-labeled LA with isotopic purity of 99%, purchased from Sigma. The reaction mixtures were subsequently quenched via acidification to pH 4 with glacial acetic acid and extracted into dichloromethane. Reaction products were taken to dryness under a stream of N_2 and stored at -80°C until HPLC analysis.

Reactions at elevated and depressed O_2 concentrations were performed using a Clark-type electrode from Yellow Springs Inc. and a YSI-5300 biological oxygen monitor. Two milliliters of 0.1 M Borate (pH 9.0) and 100 μM LA were equilibrated in a thermally controlled water-jacketed cell at 20° C. The desired O_2 concentration was established by maintaining the appropriate O_2/N_2 mixture in the headspace above the LA solution for >10 minutes. The electrode was subsequently placed in contact with the solution surface, eliminating the headspace. The reaction was initiated by injecting a solution of SLO-1 in 0.1 M Borate (pH 9.0) and incubated in the cell until acidification with N_2-saturated glacial acetic acid. Reaction products were extracted into dichloromethane, taken to dryness under N_2, and stored at -80°C until HPLC analysis.

HPLC Analysis

Reverse phase HPLC was employed to assess product distribution for the reaction of SLO-1 and its mutants with linoleic acid. Reaction products were injected onto a reverse phase HPLC system with a Luna C18 5-μm column (0.46 x 25 cm, Phenomenex). A solvent system of 78% methanol and 21.9% water with 0.1% acetic acid was employed in order to separate multiple products. A flow rate of 0.9 mL/minute was used. Product peaks were collected, taken to dryness under N_2, and stored at -80°C until further analysis.

Identification of Alternate Products

Both mass spectrometry and NMR were used to identify alternate products generated by the reaction of the Ile553Trp mutant enzyme with linoleic acid at ambient oxygen. ESI-MS analysis was performed in collaboration with Dr. Tony Iavarone (QB3/College of Chemistry Mass Spectrometry Facility at UC Berkeley). HPLC-purified product peaks were resuspended in 100% methanol for analysis by electrospray ionization mass spectrometry in negative ion mode using a Thermo LTQ Orbitrap XL mass spectrometer. NMR analysis was performed in collaboration with Dr. Jeffrey Pelton (Central California 900 MHz NMR Facility at UC Berkeley) and Dr. Chris Canlas (Berkeley College of Chemistry NMR Facility). C^{13}-labeled HPLC-purified product peaks were resuspended in 100% deuterated methanol for analysis by NMR at 25°C on a Bruker Avance II spectrometer operating at 900 MHz.

4.3 Results

Product profile of Ile553Trp reaction with LA resembles that of wild-type SLO-1 at low O_2. Prior to reacting with LA, SLO-1 must be activated by HPOD. Decreasing [O_2] impairs SLO-1 activation by HPOD and alters the identity of activation products. (*3*) To analyze the effect of the Ile553Trp mutation on enzyme activation, the product profile generated by the reaction of the mutant and LA was compared to that of the wild-type reaction at ambient and low O_2.

The reaction of wild-type SLO-1 with LA at ambient O_2 primarily produces HPOD, as evident in **Part I** of **Figure 4-2**. Since activation is efficient for the wild-type enzyme at ambient O_2, negligible amounts of activation products are produced. The reaction of Ile553Trp with LA, by contrast, generates several products in addition to HPOD, as shown in **Part II** of **Figure 4-2**. Strikingly, many of these alternate products are also generated in the reaction of wild-type SLO-1 at low O_2, which is depicted in **Part III** of **Figure 4-2**. The similarity between the product profiles of the Ile553Trp reaction and the wild-type reaction at low O_2 is consistent with diminished O_2 access and impaired activation in the mutant reaction.

It should be briefly noted that the reaction of Leu496Trp mutant with LA also produces these alternate products, albeit in smaller quantities than the Ile553Trp mutant, suggesting that activation may also be slightly impaired in this mutant. (data not shown)

13 and 9 epoxyallylic ketones are produced by the Ile553Trp reaction with LA at ambient O_2. To ensure that the alternate products generated by the Ile553Trp reaction with LA were consistent with diminished O_2 availability and impaired activation, these compounds were identified using a combination of mass spectrometry and NMR. The products analyzed are labeled as A-E in **Part II** of **Figure 4-2**.

As detailed in **Figure 4-3**, products A and B were each identified as a mixture of two compounds with molecular masses of 309 and 311 by ESI-MS, consistent with chemical formulas $C_{18}H_{30}O_4$ and $C_{18}H_{32}O_4$, respectively. Consistent with the $C_{18}H_{30}O_4$ species identified by ESI-MS, further analysis by NMR allowed for the identification of products A and B as epoxyallylic ketones—13-keto-9,10-epoxyoctadec-11E-enoic acid and 9-keto-12,13-epoxyoctadec-10E-enoic acid, respectively—as described in **Figures 4-4** and **4-5**. In **Figure 4-4**, the 2D ^{1}H-^{1}H TOCSY spectrum for product A shows a clear correlation between protons on C2 and C8, C9-10 and C11-C12, as well as C14 and C18, consistent with the localization of the epoxide at C9-C10 and the ketone at C13. The C11 and C12 protons show no connectivity with the protons on C14, confirming the presence of a ketone moiety at C13. A ^{2}J coupling constant of ~16 Hz confirms *trans* arrangement around the C11-C12 double bond. (*9*) In **Figure 4-5**, the 2D ^{1}H-^{1}H TOCSY spectrum for product B shows a clear correlation between protons on C2 and C8, C10-11 and C12-C13, as well as protons on C13 and C18, consistent with localization of the epoxide at C12-C13 and the ketone at C9. The C10 and C11 protons show no connectivity with the protons on C8, confirming the presence of a ketone moiety at C9. A ^{2}J coupling constant of ~16 Hz confirms *trans* arrangement around the C10-C11 double bond. (*9*) The structures of A and B are provided together in **Figure 4-6**.

It is worth noting that the $C_{18}H_{32}O_4$ species detected by ESI-MS in products A and B, which represents a molecular mass of 311, is consistent with the hydroxide derivative of the epoxyallylic ketones identified by NMR. The presence of epoxyallylic compounds was expected based on the scheme detailed in **Part III** of **Figure 4-1** and is consistent with Ile553Trp SLO-1 mimicking the wild-type enzyme in the absence of oxygen. It should be noted that epoxyallylic ketones (and hydroxides) rather than hydroperoxides were identified; this is not surprising, as the reduction of epoxyallylic hydroperoxides has previously been observed in similar activation studies. (*3*)

13 and 9 ketodienes are produced by the Ile553Trp reaction with LA at ambient O_2.
Products C, D, and E were also identified using a combination of mass spectrometry and NMR. The molecular mass of all three products was identified as 293 by ESI-MS, consistent with a chemical formula of $C_{18}H_{30}O_3$, as shown in **Figure 4-7**. In accordance with ESI-MS data, products C and E showed similar retention times by reverse phase HPLC as commercial standards for 13-oxo-9Z,11E-octadecadienoic acid and 9-oxo-10E,12Z-octadecadienoic acid, respectively. This identification was confirmed by comparing ^{1}H 1D NMR spectra for products C and E with those of commercial standards, depicted in **Figure 4-8** and **4-9**.

Also in accordance with ESI-MS data, Product D was identified by NMR analysis as 13-oxo-9E, 11E-octadecadienoic acid, as detailed in **Figures 4-10 and 4-11**. In **Part I** of **Figure 4-10**, the 2D ^{1}H-^{1}H TOCSY spectrum for product D shows a clear correlation between protons on C2 and C8, C9-C12 and C8, as well as C14 and C18, consistent with the localization of the ketone at C13. The C11 and C12 protons show no connectivity with the protons on C14, confirming the presence of a ketone moiety at C13. The relative cross peak intensities of the off-diagonal peaks corresponding to C14 at 2.59 ppm further support the localization of the ketone to C13. As described in **Part II** of **Figure 4-10**, the presence of the diene was confirmed by COSY, which shows connectivity between protons on C9-C12. The *trans-trans* connectivity of the C9-C10 and C11-C12 double bonds, meanwhile, was established by analyzing ^{2}J coupling values for the protons on C9-C12, as described in **Figure 4-11**. $^2J_{9\text{-}10}$ and $^2J_{11\text{-}12}$ coupling constants were found equivalent to approximately 16 Hz, consistent with a *trans* arrangement around both of these double bonds. (*9*) Taken together, **Figures 4-10** and **4-11** indicate that product D represents 13-oxo-9E,11E-octadecadienoic acid.

The structures for compounds C, D, and E are provided together in **Figure 4-12**. The presence of ketodiene compounds was expected based on the scheme detailed in **Part III** of **Figure 4-1**. This result provides strong evidence of diminished O_2 access and impaired activation in the Ile553Trp mutant since ketodienes are produced during the inefficient activation of wild-type SLO-1 by HPOD in the absence of O_2, as shown in **Part II** of **Figure 4-1**.

Increasing O_2 partially restores the product profile of the Ile553Trp reaction with LA.
As described above, the Ile553Trp reaction with LA generates a significant amount of activation products at ambient oxygen. If the formation of these epoxyallylic ketones and ketodienes were indeed driven by reduced O_2 availability at the active site, it would be expected that increasing [O_2] would reduce their presence. To test this hypothesis, the Ile553Trp reaction with LA was performed at ambient (284 μM) and high O_2 (1365 μM). The product profiles of these reactions are provided in **Figure 4-13**. It is clear that the product profile for the reaction at higher oxygen

displays a decreased amount of these products, suggesting that additional O_2 can restore the product profile of Ile553Trp SLO-1. These results are consistent with the Ile553Trp mutation impeding oxygen access to the active site and therein driving the formation of the activation products identified.

4.4 Discussion

As discussed in **Chapters 2** and **3**, a channel for oxygen delivery to the active site of SLO-1 was identified via computational methods and validated using site-directed mutagenesis. Introducing a tryptophan into the channel at residue Ile^{553} diminished oxygen availability at the active site to the greatest extent, as reflected in the mutant's dramatically elevated $K_M(O_2)$. Since oxygen plays an important role in the activation of SLO-1 for reaction with LA, it was expected that the activation process might be perturbed in the Ile553Trp reaction. The product profile of the Ile553Trp reaction with LA was examined by reverse phase HPLC to assess activation in this mutant.

Our findings suggest that activation is indeed impeded in Ile553Trp SLO-1, consistent with impaired access of O_2 to the active site in this mutant. Two pieces of evidence are in support of this conclusion—first, the similar product profiles of the Ile553Trp reaction with LA and that of wild-type at low O_2 and second, the identity of the activation products produced by the Ile553Trp mutant.

Diminished [O_2] leads to impaired activation of wild-type SLO-1 by HPOD. If the Ile553Trp mutation disrupts oxygen availability at the active site, the product profile of the mutant reaction with LA should resemble that of wild-type SLO-1 at low O_2. This is indeed the case, as evident in **Figure 4-2**. While the wild-type enzyme at ambient oxygen produces primarily HPOD, wild-type enzyme at low oxygen and the Ile553Trp mutant both produce several additional products. The striking similarity between the behavior of the Ile553Trp mutant and wild-type at low O_2 is suggestive of diminished O_2 access and impaired activation in the mutant reaction.

Second, the identity of the products generated by the Ile553Trp reaction with LA is consistent with impaired activation. These products, labeled as A-E in **Part II** of **Figure 4-2**, were identified via ESI-MS and NMR as epoxyallylic ketones and ketodienes. The formation of epoxyallylic and ketodiene compounds validates the proposed activation scheme detailed in **Part III** of **Figure 4-1** for Ile553Trp. The formation of ketodienes is particularly strong evidence of diminished O_2 access and impaired activation in the Ile553Trp mutant since ketodienes are typically observed in the anaerobic activation of wild-type SLO-1, as shown in **Part II** of **Figure 4-1**. To determine whether limited O_2 availability was definitively driving the formation of these activation products, the Ile553Trp reaction with LA was performed at high O_2. Indeed, increasing O_2 reduced the formation of activation products as evident in **Figure 4-13**.

Together, our studies indicate that limited availability at the O_2 active site results in impaired activation for the Ile553Trp mutant. Consistent with this conclusion, the reaction of Ile553Trp and LA at ambient O_2 resembles the reaction of the wild-type enzyme at low O_2. Impaired activation is evidenced by the production of ketodienes, in addition to epoxyallylic compounds, during the Ile553Trp-catalyzed peroxidation of LA. Investigating activation in the Ile553Trp mutant highlights the importance of oxygen availability at the active site in facilitating enzyme activation.

It is worth noting that diminished O_2 not only impairs activation by HPOD, but also influences the peroxidation of LA by increasing linoleyl radical dissociation. Increased radical dissociation,

in turn, translates into an increased quantity of activation products, since each time the linoleyl radical dissociates, the enzyme is left in the inactive ferrous state and must be reactivated by HPOD. Thus, the increased quantity of activation products identified in the reaction of LA with Ile553Trp and wild-type at low O_2 is driven not only by inefficient activation, but also by increased linoleyl dissociation during LA peroxidation.

Interestingly, the studies described here on Ile553Trp SLO-1 parallel previous studies by the Brash group on epidermal lipoxygenase 3, or eLOX3. In this work, diminishing O_2 access to the active site via site-directed mutagenesis was shown to impair activation and introduce hydroperoxide isomerase reactivity into SLO-1, a proto-typical dioxygenase. The Brash group has previously made the reverse observation while engineering eLOX3. In stark contrast with wild-type SLO-1, wild-type eLOX3 is a hydroperoxide isomerase with very limited dioxygenase activity. (*10*) Introducing an alanine to glycine mutation near the active site of eLOX3 appears to increase oxygen availability at the active site and promote dioxygenase activity in the enzyme. (*11*) In short, reducing oxygen availability in SLO-1 appears to promote hydroperoxide isomerase reactivity while increasing oxygen availability in eLOX3 appears to promote its dioxygenase activity. Taken together, these observations suggest that oxygen availability at the active site directs the reactivity of SLO-1 and eLOX3 and determines where these enzymes fall along the dioxygenase/hydroperoxide isomerase spectrum.

4.5 Conclusions and Future Directions

Enzymes are complex systems that contain a variety of pockets, clefts, and channels throughout the protein matrix. These gaps and tunnels represent potential transport pathways for ions, small molecules, and water and can play a critical role in tuning enzyme function. (*12*) In this work, the functional role of gas migration pathways was examined in soybean lipoxygenase 1, the best-studied member of the lipoxygenase family. SLO-1 catalyzes the regio- and stereospecific peroxidation of linoleic acid to yield 13S hydroperoxyoctadecadienoic acid (13S HPOD). Our studies support a role for a single oxygen delivery channel within SLO-1 that ensures the regio- and stereospecificity of oxygen insertion during catalysis. Interestingly, this channel is consistent with a cavity originally identified in the crystal structure of SLO-1 and previously proposed as an O_2 channel by the Klinman group. (*13-15*)

Our evidence points to a model for SLO-1 that features a variety of pockets favorable for oxygen migration throughout the protein but a single pathway for oxygen delivery to the active site. This model is depicted in **Figure 4-14** and is consistent with our computational studies, discussed in **Chapter 2**. While many pockets and pathways are identified throughout the protein by implicit ligand sampling and CAVER, both techniques also highlight a single channel that is most competent for oxygen delivery. (*12*, *16*) This channel's bottleneck residues were identified by CAVER as Ile^{553}, Ile^{547}, Leu^{496}, and Val^{564}. As reviewed in **Chapter 3**, site-directed mutagenesis of these residues validated a functional role for the channel. Introducing tryptophan at positions 553 and 496, in particular, significantly disrupts oxygen access to the active site, as evidenced by increased Michaelis constants for oxygen and altered reaction regio- and stereospecificity.

Interestingly, introducing bulk at positions 553 and 496 appears to influence oxygen migration in distinct ways. The Ile553Trp mutation diminishes oxygen availability at the active site, increasing the rate of linoleyl radical dissociation and leading to an increase in the proportion of 13R, 9S, and 9R HPOD produced by the peroxidation of LA. The efficiency of enzyme activation by HPOD is also dramatically reduced in this mutant. A model for the Ile553Trp mutant enzyme is depicted in **Figure 4-15**. The primary effect of the Leu496 mutation, by contrast, is to ungate an alternate channel for oxygen migration to the active site. While the proportion of 13R HPOD formed increases slightly, the proportion of 9S and 9R HPOD generated increases significantly in the Leu496Trp reaction with LA compared to wild-type. This observation is consistent with oxygen traveling along an alternate pathway toward carbon 9 in this mutant. A model for the Leu496Trp mutant enzyme is depicted in **Figure 4-16**.

In future studies, it would be interesting to probe oxygen migration pathways in SLO-1 via xenon-pressurized crystallography. Investigating the localization of xenon in the structure of wild-type SLO-1 could corroborate the functional role of the oxygen delivery channel validated in this work. Xenon-pressurized crystallography of Ile553Trp and Leu496Trp SLO-1 could also provide valuable insight into how oxygen migration is altered in each of these mutants. For example, xenon binding sites might be displaced in the Ile553Trp mutant while the Leu496Trp mutant might feature additional xenon binding sites, consistent with an alternate channel functioning in the enzyme.

Identifying gas migration pathways is critical to unraveling structure-function relationships in proteins. Together, our computational and experimental studies highlight the important role of the protein matrix in tuning oxygen insertion in soybean lipoxygenase 1. Computational studies were employed to visualize pathways for oxygen migration in the enzyme. A single preferred pathway for oxygen was identified and site-directed mutagenesis was used to assess the impact of obstructing this channel. Analysis of reaction kinetics and product distribution in these mutants demonstrates that this channel plays a key role in shuttling oxygen to the active site and modulating the regio- and stereospecificity of oxygen insertion into LA. This transformative result provides valuable insight into potential mechanisms of oxygen delivery in members of the LOX family as well as oxygen-dependent enzymes in general. Going forward, understanding the role of the protein matrix in tuning catalysis will be key to the success of protein engineering and, ultimately, *de novo* enzyme design.

I. Reactivity of SLO-1 with HPOD under aerobic conditions

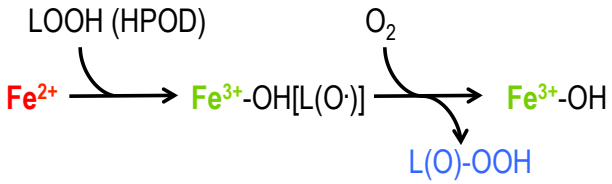

II. Reactivity of SLO-1 with HPOD under anaerobic conditions

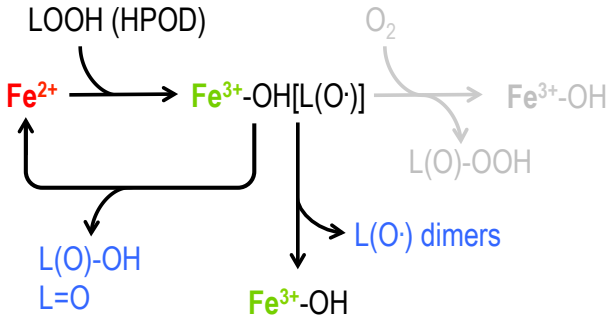

III. Proposed reactivity of Ile553Trp SLO-1 with HPOD under aerobic conditions

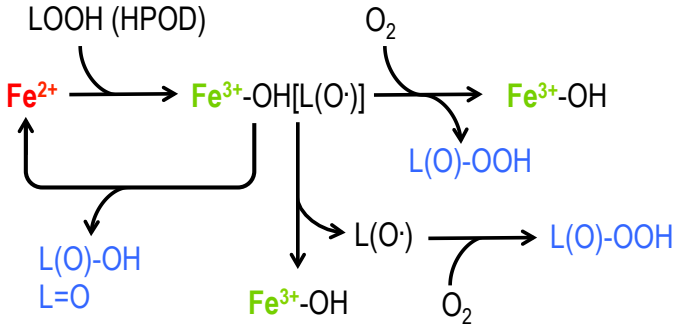

Figure 4-1. Proposed reactivity for Ile553Trp SLO-1 with HPOD (III) based on reactivity of wild-type SLO-1 with HPOD at ambient and anaerobic conditions (I and II). Ferrous and ferric iron ligands are depicted in red and green, respectively. Reaction products are depicted in blue. (I) Under aerobic conditions, ferrous SLO-1 is activated efficiently to ferric SLO-1. The ferrous enzyme reacts with HPOD to produce an epoxyallylic radical intermediate bound to the ferric enzyme. The radical dissociates after reacting with oxygen, forming an epoxyallylic hydroperoxide in solution and leaving the ferric enzyme activated for reaction with LA. (*3*) (II) By contrast, ferrous SLO-1 is activated inefficiently under anaerobic conditions. In the absence of O_2, the epoxyallylic radical generated by the reaction of ferrous SLO-1 and HPOD participates in two distinct processes. In one, the epoxyallylic radical dissociates, dimerizing and leaving the ferric enzyme activated for reaction with LA. In the second, the epoxyallylic radical remains bound to the enzyme and re-reduces ferric SLO-1 to its inactive ferrous state. This process produces epoxyalcohols and ketones and represents the hydroperoxide isomerase reactivity of SLO-1. (*3*) (III) Since the Ile553Trp mutation diminishes oxygen availability at the active site, the mutant reaction with HPOD is also proposed to display hydroperoxide isomerase activity. As in wild-type SLO-1 in the absence of oxygen, it is hypothesized that the epoxyallylic radical generated can remain bound to Ile553Trp SLO-1 and re-reduce the ferric enzyme to its ferrous state. Alternatively, the radical can dissociate spontaneously and react with O_2 in solution, leaving the enzyme activated for reaction with LA. Finally, the radical can also react with oxygen on the enzyme and dissociate; this process also leaves the enzyme in its activated ferric state.

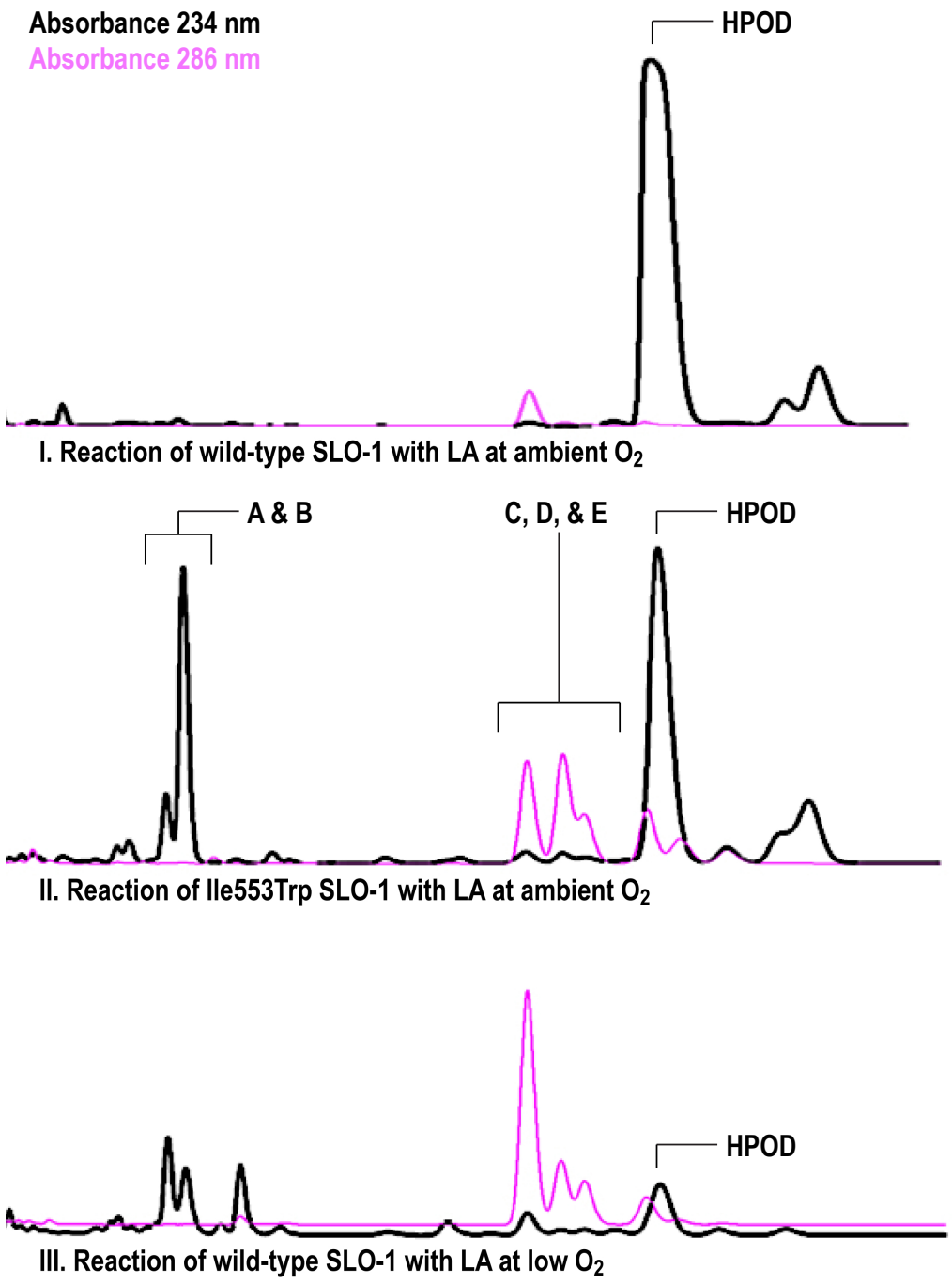

Figure 4-2. Reverse phase HPLC analysis of the reaction of Ile553Trp SLO-1 with LA at ambient O_2 (II) and wild-type SLO-1 with LA at ambient (I) and low O_2 (III). The product profile of the Ile553Trp reaction with LA is similar to that of wild-type SLO-1 at low O_2. While the wild-type enzyme at ambient oxygen produces primarily HPOD, the wild-type enzyme at low oxygen and the Ile553Trp mutant both produce several additional products in significant amounts. These products are labeled A-E in the Ile553Trp reaction trace above (II). Ambient and low oxygen reactions were performed at 284 μM O_2 and 28 μM O_2, respectively. C_{13} aldehydes, previously observed in the anaerobic reaction of SLO-1 with HPOD and LA, were also observed here but are not pictured. (*3*)

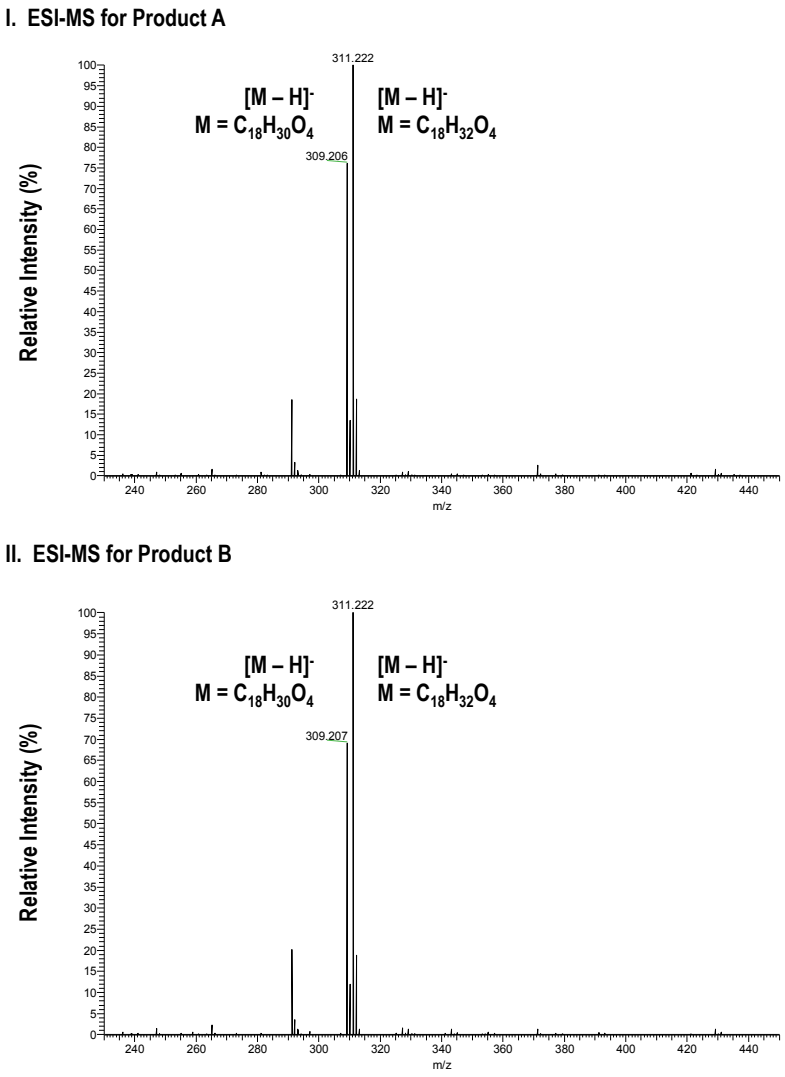

Figure 4-3. ESI-MS analysis of products A and B of the Ile553Trp SLO-1 reaction with LA. Products A (I) and B (II) were each identified as a mixture of two compounds with molecular masses of 309 and 311, consistent with chemical formulas $C_{18}H_{30}O_4$ and $C_{18}H_{32}O_4$, respectively. A minor peak (m/z of 291) corresponding to the chemical formula $C_{18}H_{28}O_3$ was also detected during ESI-MS analysis of products A and B.

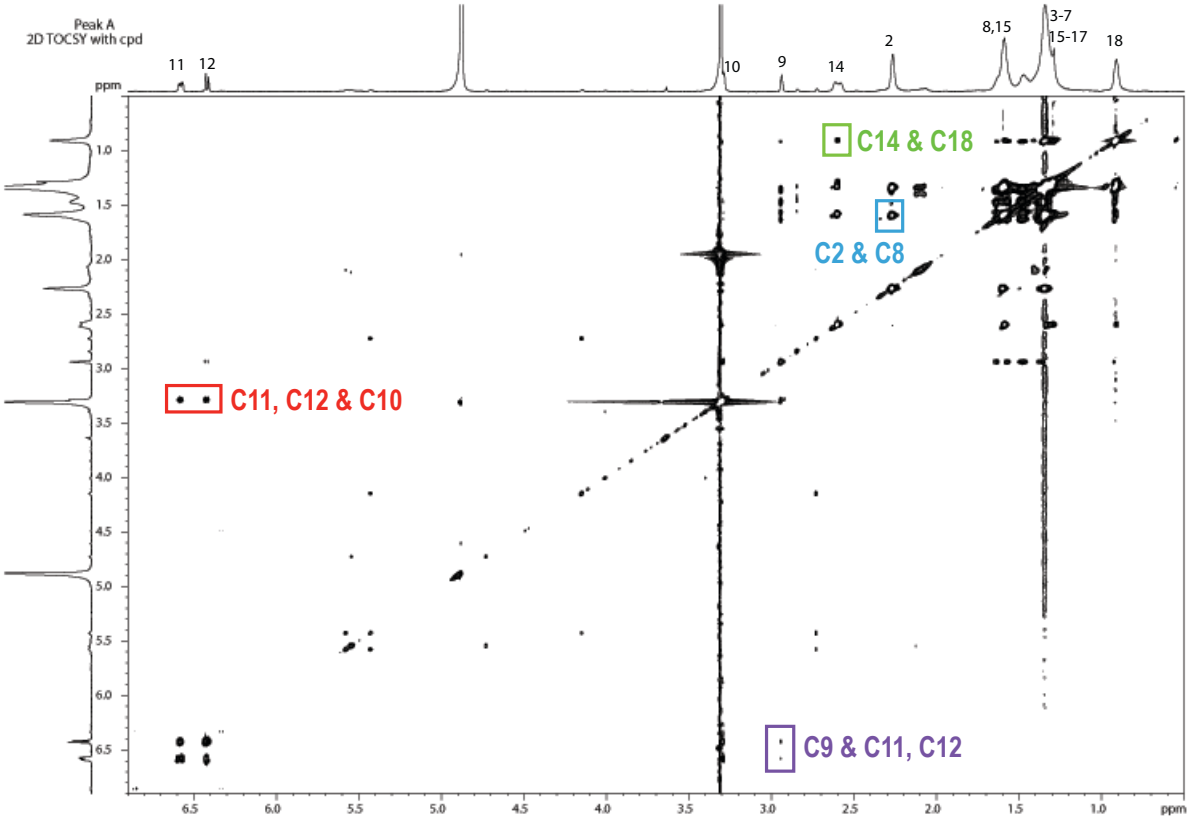

Figure 4-4. 2D ^{1}H-^{1}H TOCSY spectrum for product A of the Ile553Trp SLO-1 reaction with LA. Consistent with the $C_{18}H_{30}O_4$ species identified by ESI-MS, product A was identified as 13-keto-9,10-epoxyoctadec-11E-enoic acid by NMR. The 2D ^{1}H-^{1}H TOCSY spectrum shows a clear correlation between protons on C2 and C8, C9-10 and C11-C12, as well as C14 and C18, consistent with the localization of the epoxide at C9-C10 as well as the ketone at C13. The C11 and C12 protons show no connectivity with the protons on C14, confirming the presence of a ketone moiety at C13. A ^{2}J coupling constant of ~16 Hz confirms a *trans* arrangement around the C11-C12 double bond. (*9*) The cross peak between the protons of C9 and C18 is due to an impurity from the product B sample.

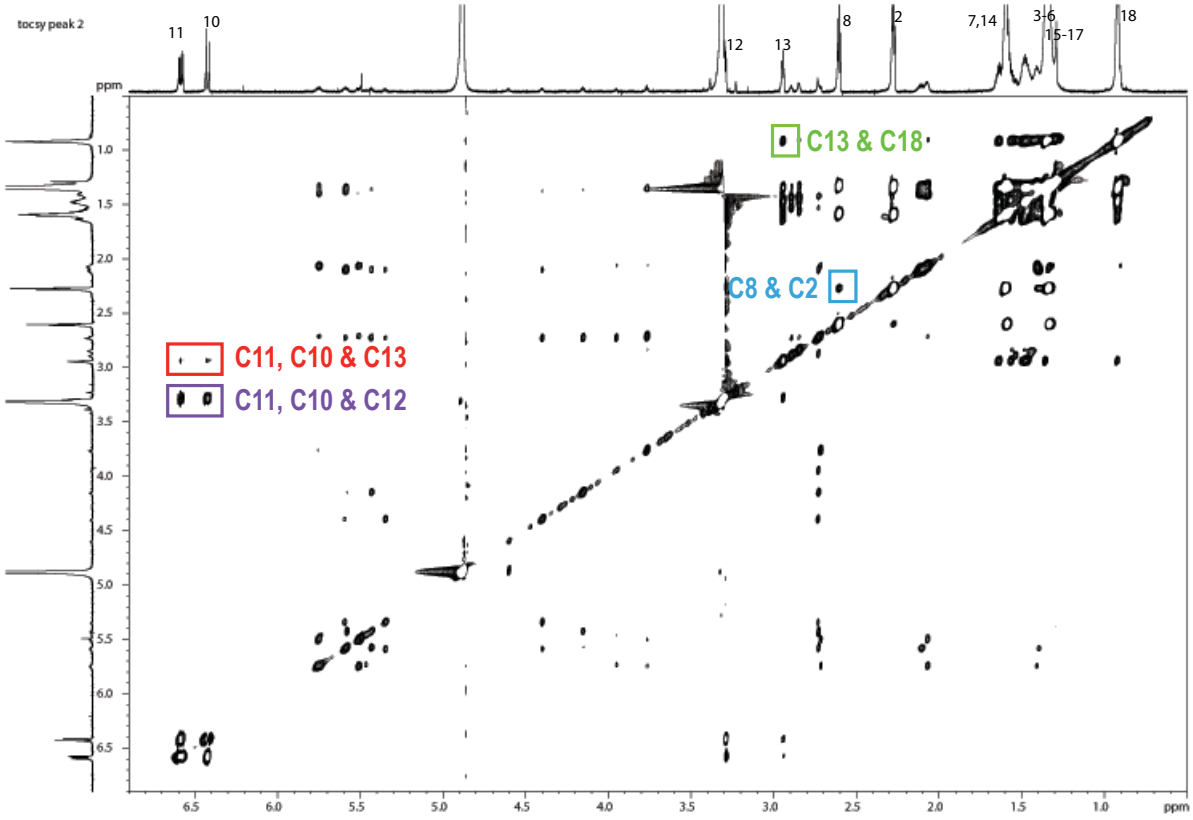

Figure 4-5. 2D ^{1}H-^{1}H TOCSY spectrum for product B of the Ile553Trp SLO-1 reaction with LA. Consistent with the $C_{18}H_{30}O_4$ species identified by ESI-MS, product B was identified as 9-keto-12,13-epoxyoctadec-10E-enoic acid by NMR. The 2D ^{1}H-^{1}H TOCSY spectrum shows a clear correlation between protons on C2 and C8, C10-11 and C12-C13, as well as protons on C13 and C18, consistent with localization of the epoxide at C12-C13 and the ketone at C9. The C10 and C11 protons show no connectivity with the protons on C8, confirming the presence of a ketone moiety at C9. A ^{2}J coupling constant of ~16 Hz confirms *trans* arrangement around the C10-C11 double bond. (*9*)

I. Product A

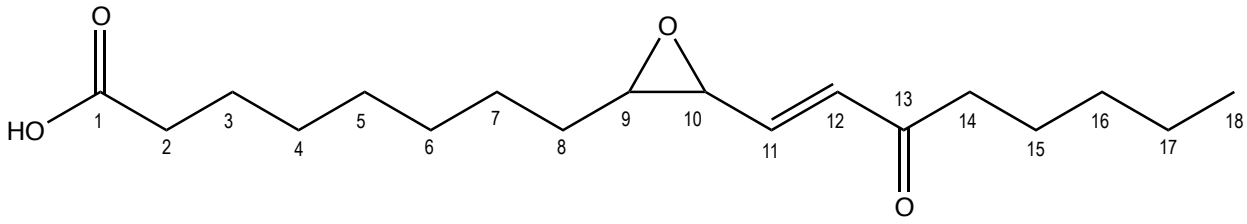

II. Product B

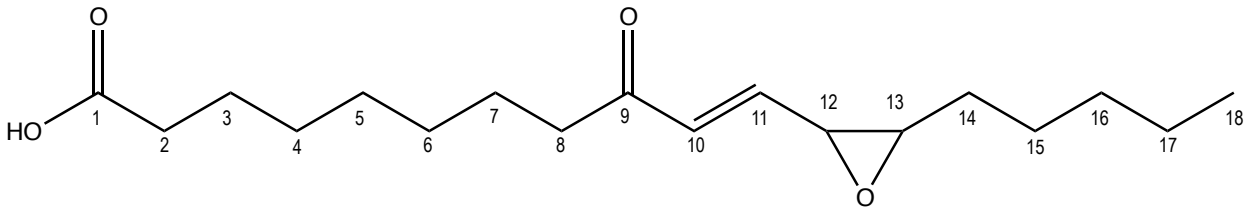

Figure 4-6. Identification of products A and B of the Ile553Trp SLO-1 reaction with LA. Products A and B were analyzed using a combination of mass spectrometry and NMR. Consistent with the $C_{18}H_{30}O_4$ species identified by ESI-MS, products A and B were identified as the following epoxyallylic ketones by NMR—13-keto-9,10-epoxyoctadec-11E-enoic acid and 9-keto-12,13-epoxyoctadec-10E-enoic acid, respectively. The $C_{18}H_{32}O_4$ species detected by ESI-MS in products A and B, which represents a molecular mass of 311, is consistent with the hydroxide derivative of the epoxyallylic ketones identified by NMR.

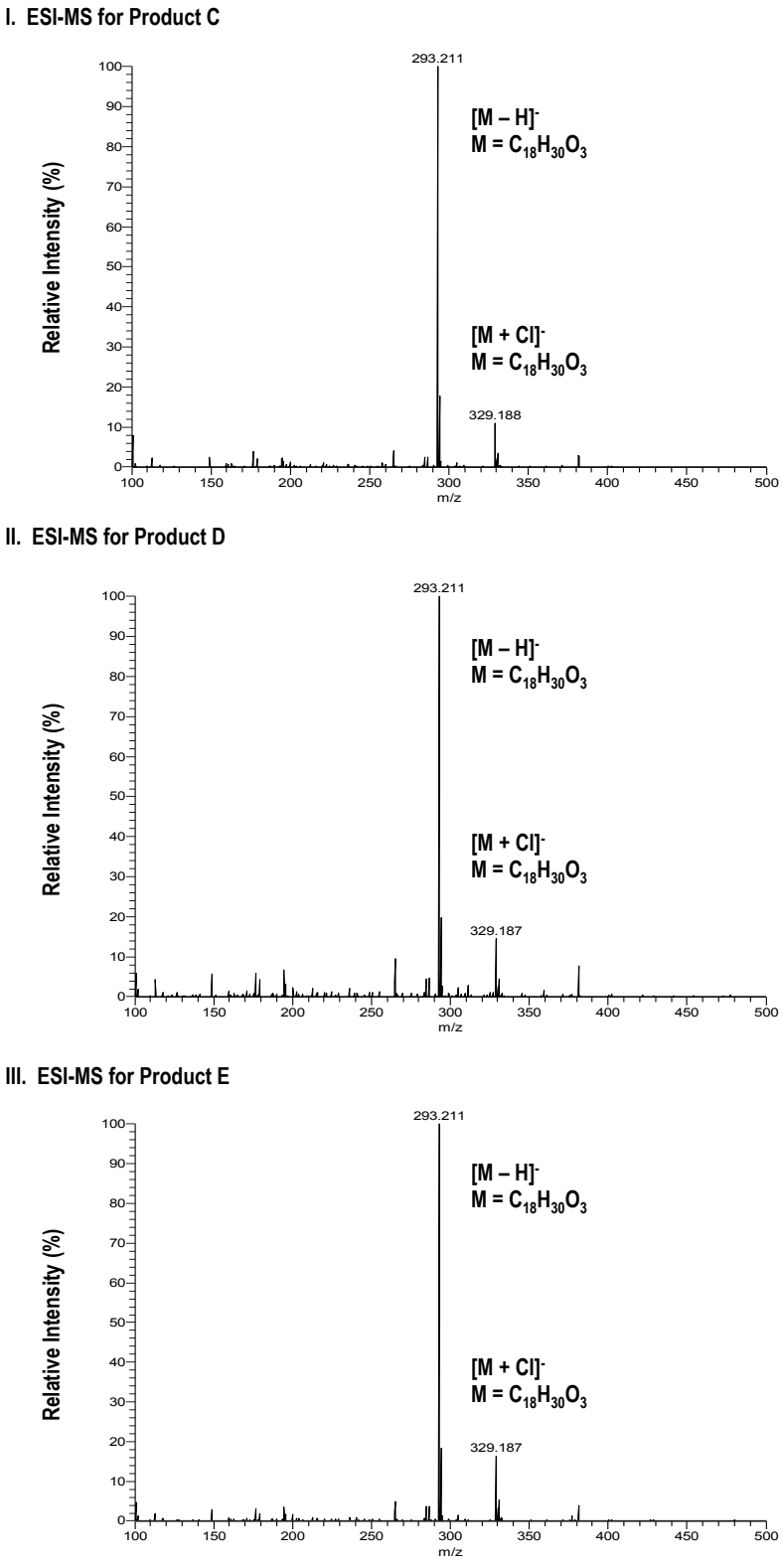

Figure 4-7. ESI-MS analysis of products C (I), D (II), and E (III) of the Ile553Trp SLO-1 reaction with LA. The molecular mass of all three products was identified as 293 by ESI-MS, consistent with a chemical formula of $C_{18}H_{30}O_3$. The minor peak (m/z of 329) represents an adduct of the fatty acid analyte with a chloride ion.

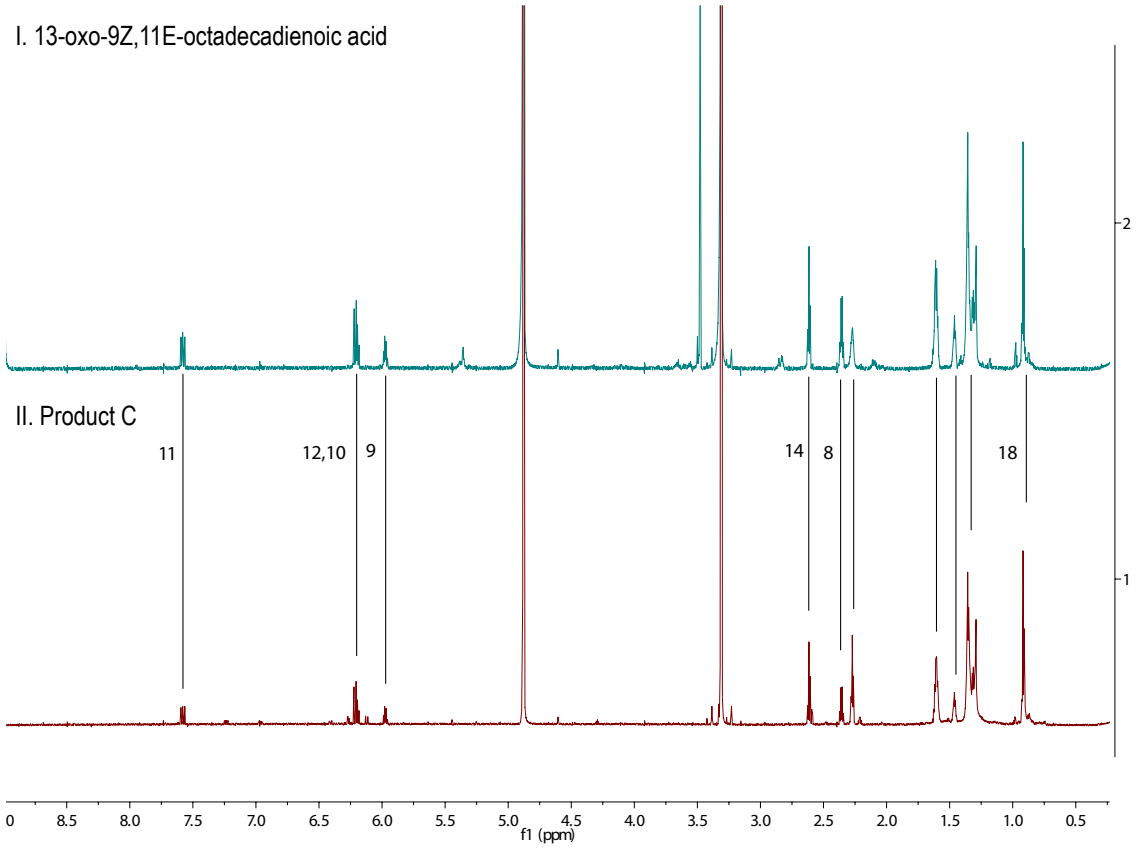

Figure 4-8. ^{1}H 1D NMR spectra for 13-oxo-9Z,11E-octadecadienoic acid (I) and product C of the Ile553Trp SLO-1 reaction with LA (II). Consistent with ESI-MS data, product C showed a similar retention time by reverse phase HPLC as the commercial standard for 13-oxo-9Z,11E-octadecadienoic acid. This assignment was supported by ^{1}H 1D NMR data shown above. Peaks observed at ~5.0 ppm and ~3.5 ppm represent solvent-related signal.

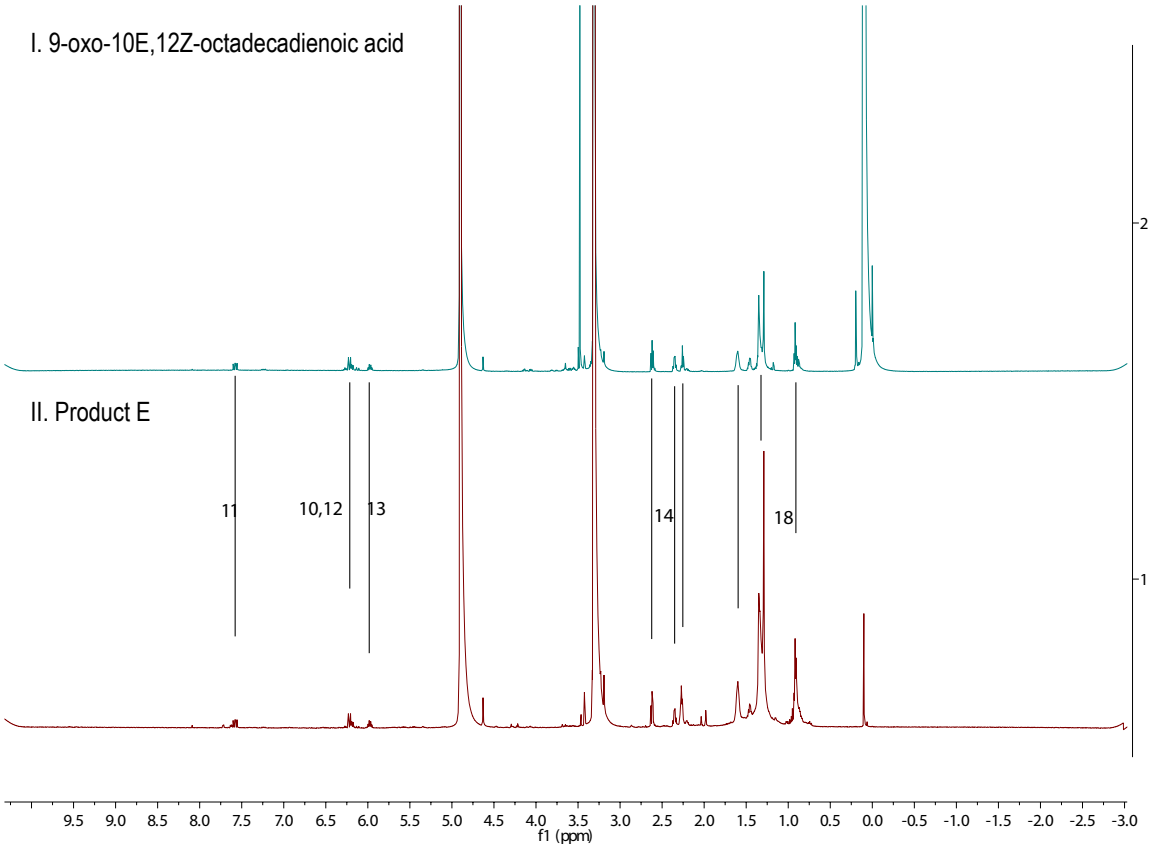

Figure 4-9. ^{1}H 1D NMR spectra for 9-oxo-10E,12Z-octadecadienoic acid (I) and product E of the Ile553Trp SLO-1 reaction with LA (II). Consistent with ESI-MS data, product E showed a similar retention time by reverse phase HPLC as the commercial standard for 9-oxo-10E,12Z-octadecadienoic acid. This assignment was supported by ^{1}H 1D NMR data, as shown above. Peaks observed at ~5.0 ppm and ~3.5 ppm represent solvent-related signal.

I. 2D ^{1}H-^{1}H TOCSY spectrum of product D

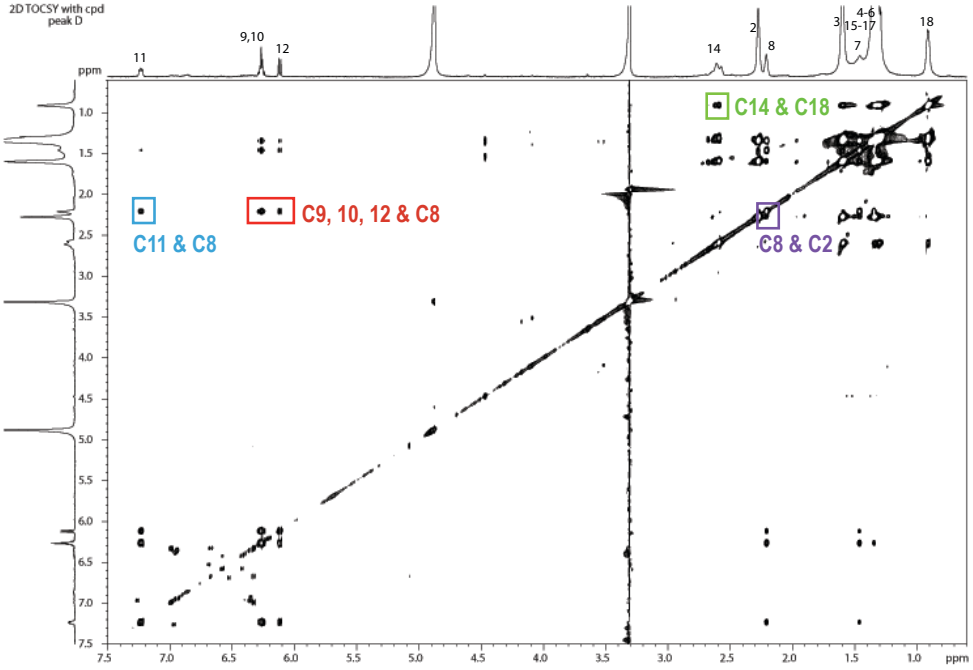

II. 2D ^{1}H-^{1}H COSY spectrum of product D

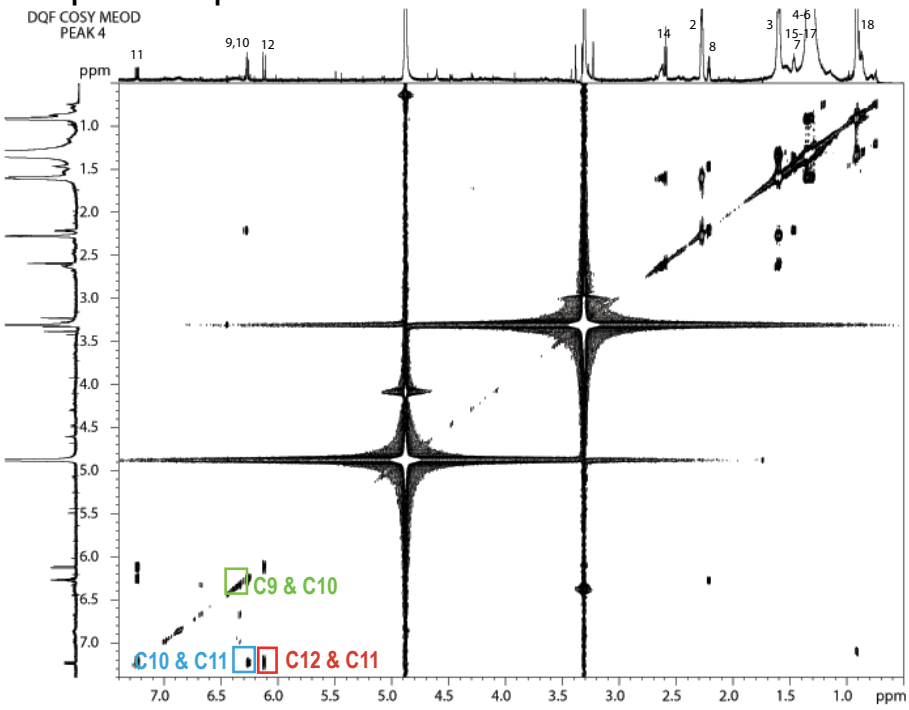

Figure 4-10. 2D ^{1}H-^{1}H TOCSY and COSY spectra for product D of the Ile553Trp SLO-1 reaction with LA. Consistent with ESI-MS, product D was identified as 13-oxo-9,11-octadecadienoic acid by NMR. (I) The 2D ^{1}H-^{1}H TOCSY spectrum shows a clear correlation between protons on C2 and C8, C9-C12 and C8, as well as C14 and C18, consistent with the localization of the ketone at C13. The C11 and C12 protons show no connectivity with the protons on C14, confirming the presence of a ketone moiety at C13. The relative cross peak intensities of the off-diagonal peaks corresponding to C14 at 2.59 ppm further support the localization of the ketone to C13. (II) The presence of the diene was confirmed by COSY, which shows connectivity between protons on C9-12.

I. 1D ^{1}H NMR spectrum of product D (zoom in on C12 and C11 protons)

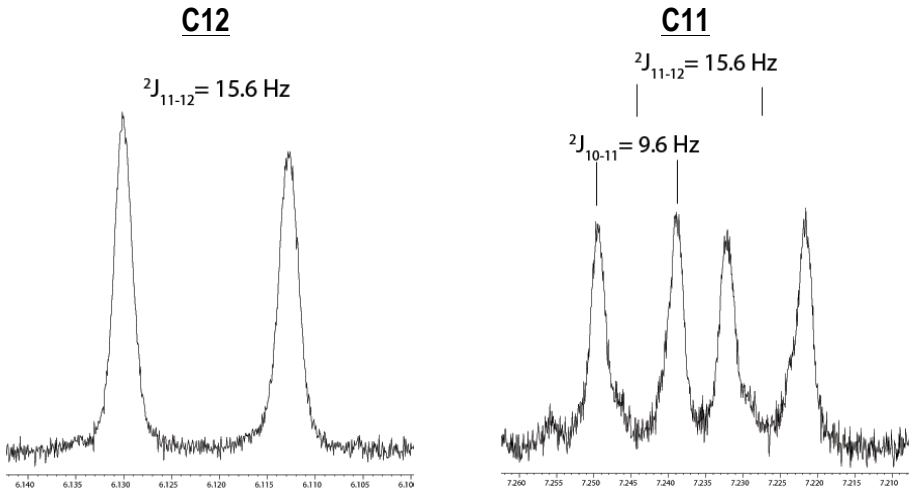

I. 2D ^{1}H-^{1}H COSY spectrum of product D (zoom in on C10-C11 cross peak)

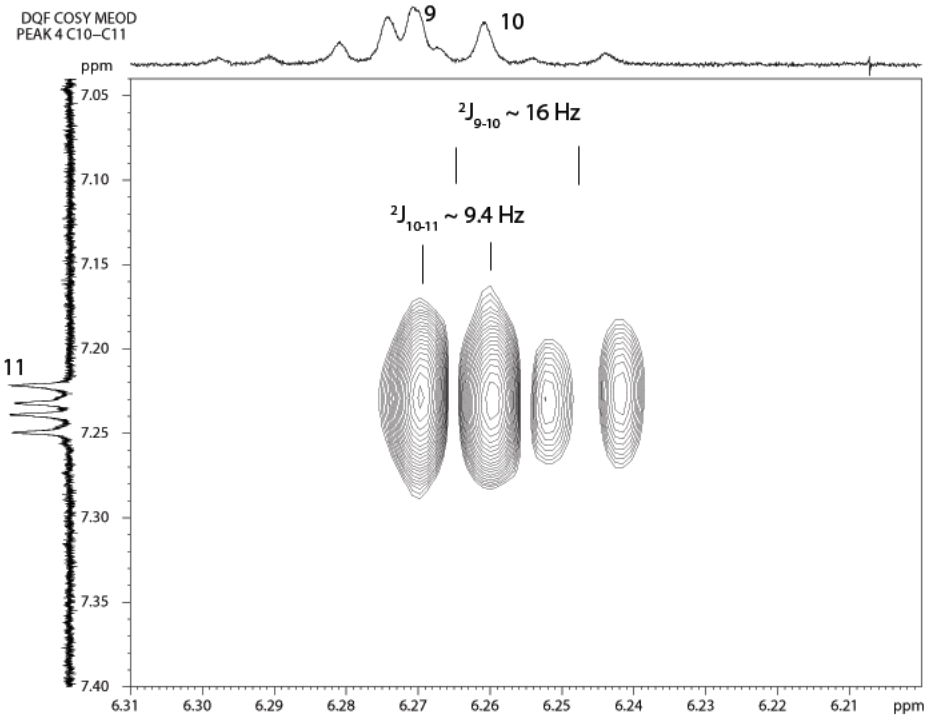

Figure 4-11. Establishing *trans-trans* diene stereochemistry for product D of the Ile553Trp SLO-1 reaction with LA. (I) The 1D ^{1}H NMR spectrum for the C12 proton shows a doublet pattern with ^{2}J= 15.6 Hz suggesting a *trans* arrangement between the protons of C11 and C12. Consistent with this observation, the 1D ^{1}H NMR spectrum for the C11 proton shows a double-doublet pattern with ^{2}J= 15.6 Hz (due to the *trans* arrangement between protons from C11 and C12) and ^{2}J= 9.6 Hz (J-coupling value of protons between C10 and C11). (*9*) (II) The C10-C11 cross peak in the 2D ^{1}H-^{1}H COSY spectrum for product D clearly discerns the double-doublet splitting pattern of the proton on C10. The $^{2}J_{9\text{-}10}$ ~16Hz coupling between protons on C9 and C10 suggests a *trans* arrangement between these two protons. (*9*) In summary, part I and part II of **Figure 4-11** confirm the *trans* arrangement of both the C11-C12 and C9-C10 double bonds, respectively.

I. Product C

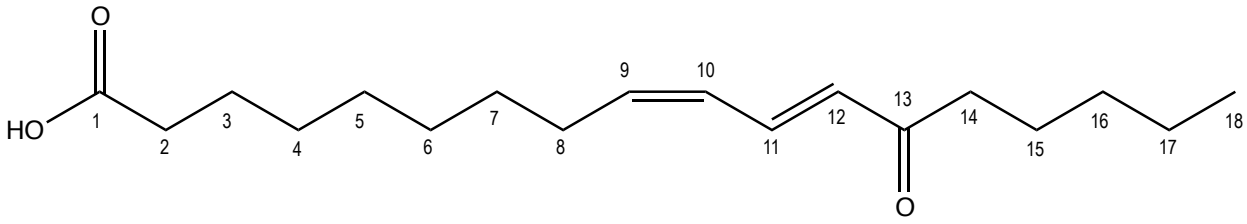

II. Product D

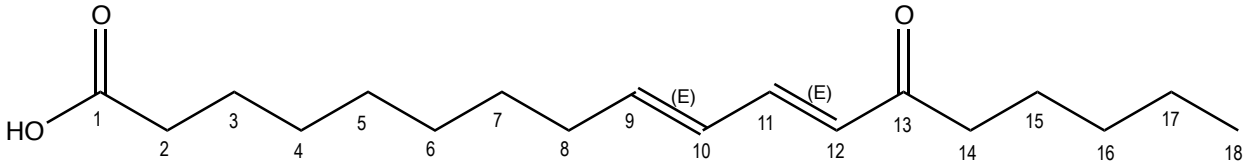

III. Product E

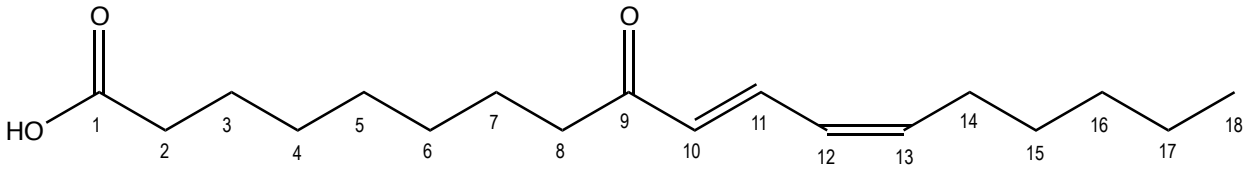

Figure 4-12. Identification of products C, D, and E of the Ile553Trp SLO-1 reaction with LA. Products C, D, and E were analyzed using a combination of mass spectrometry and NMR. The molecular mass of all three products was determined as 293 by ESI-MS, consistent with a chemical formula of $C_{18}H_{30}O_3$. Consistent with ESI-MS data and NMR analysis, products C, D, and E were identified as the following ketodienes—13-oxo-9Z,11E-octadecadienoic acid, 13-oxo-9E,11E-octadecadienoic acid, and 9-oxo-10E,12Z-octadecadienoic acid.

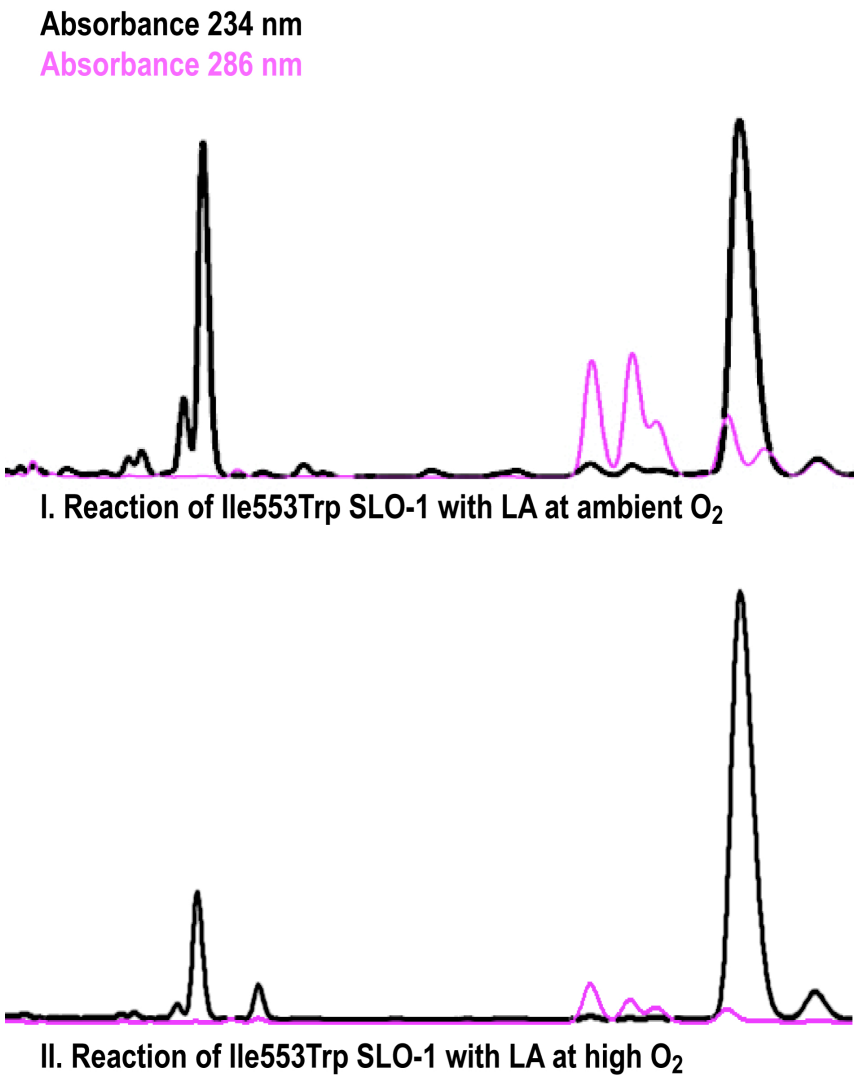

Figure 4-13. Reverse phase HPLC analysis of the reaction of Ile553Trp SLO-1 with LA at ambient O_2 (I) and high O_2 (II). Increased oxygen appears to decrease the amount of activation products—both epoxyallylic and ketodiene compounds—generated. Ambient oxygen reactions were performed at 284 μM O_2 and high oxygen reactions were performed at 1365 μM O_2.

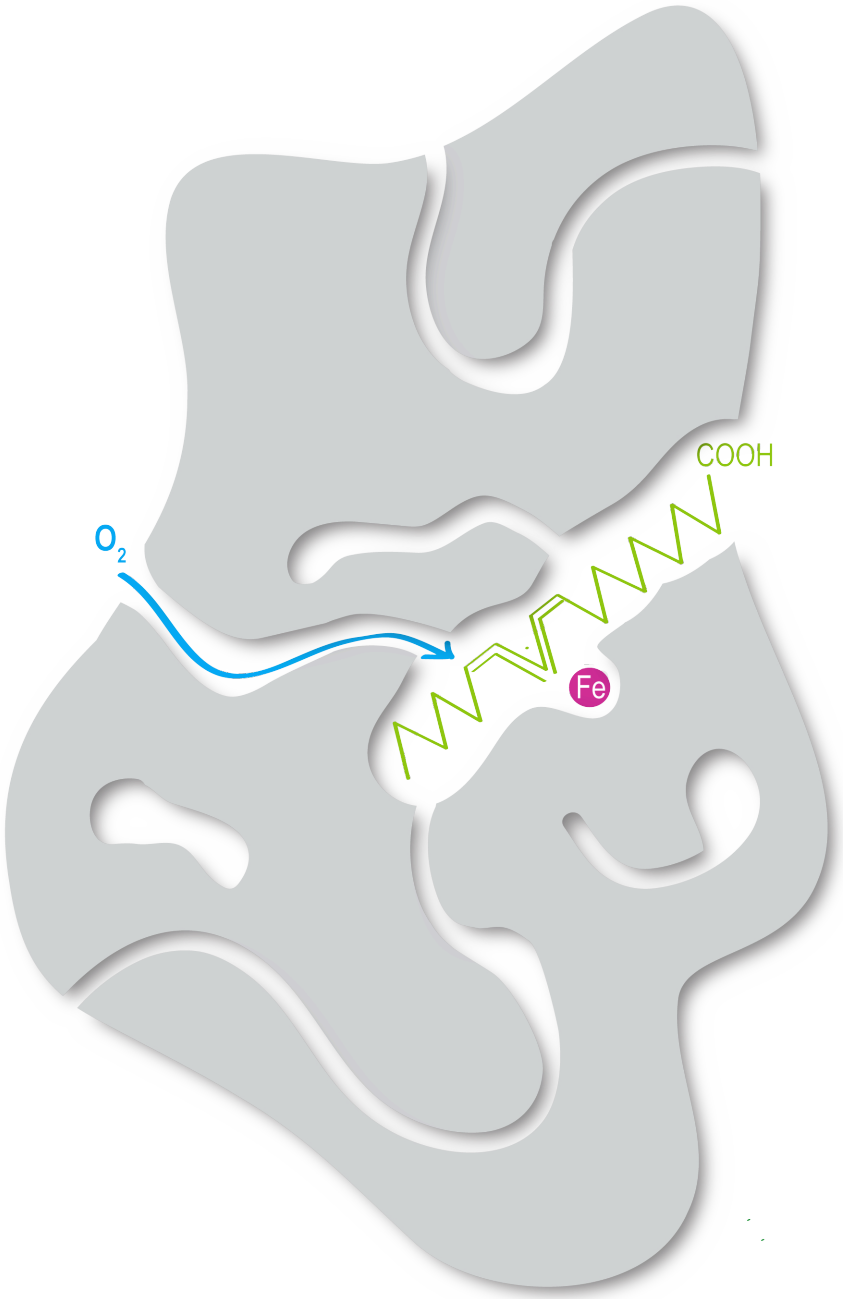

Figure 4-14. Model of gas migration in wild-type SLO-1 based on computational and experimental studies. While the SLO-1 protein matrix contains a variety of tunnels and cavities, one pathway (blue) is primarily utilized for oxygen delivery to the active site. Perturbation of this pathway can alter oxygen transport in the enzyme, in some cases diminishing oxygen access and, in some, opening up alternate pathways to the active site. The SLO-1 protein matrix is depicted in gray, LA in green, and the catalytic iron in magenta.

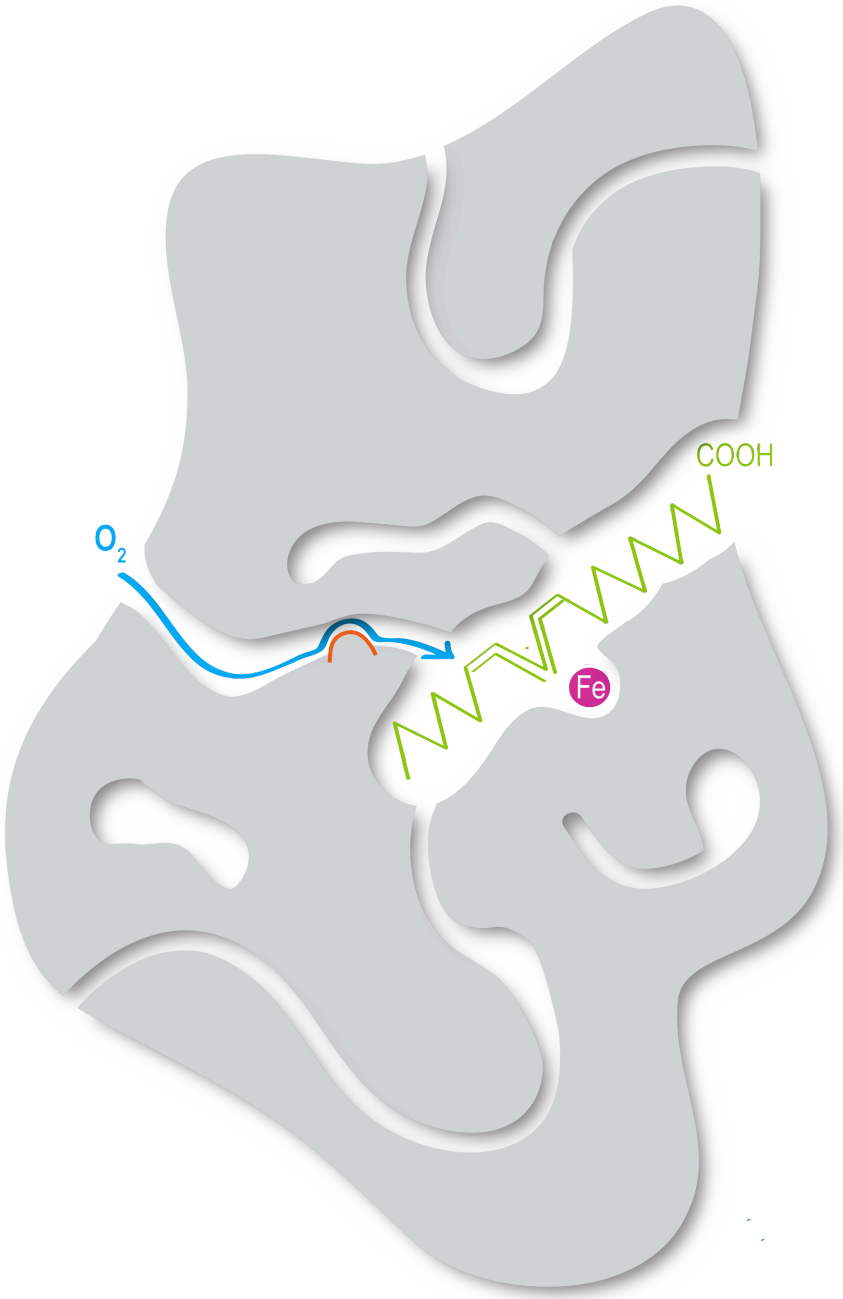

Figure 4-15. Model of gas migration in Ile553Trp SLO-1 based on computational and experimental studies. The oxygen delivery channel (blue) is occluded by the Ile553Trp mutation (outlined in orange). O_2 availability at the active site is diminished, as evidenced by an increased Michaelis constant for oxygen and an increased proportion of 13R, 9S and 9R HPOD produced in the peroxidation of LA. It is possible that O_2 access to the substrate radical in Ile553Trp SLO-1 requires transient protein motions that open up space around position 553 and allow O_2 passage to the active site. The SLO-1 protein matrix is depicted in gray, LA in green, and the catalytic iron in magenta.

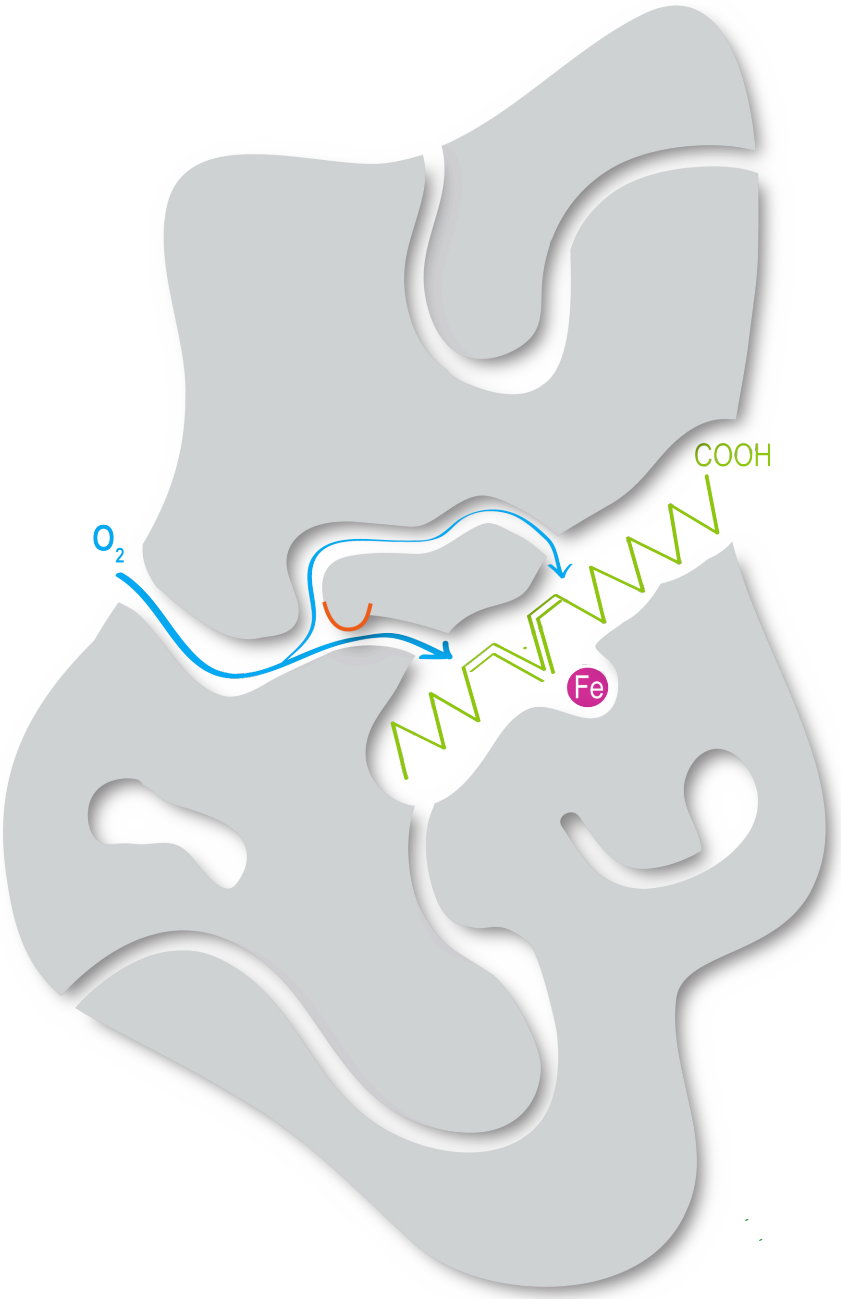

Figure 4-16. Model of gas migration in Leu496Trp SLO-1 based on computational and experimental studies. The Leu496Trp mutation (outlined in orange) ungates an alternate pathway to the active site, significantly increasing the proportion of 9S and 9R HPOD produced in the peroxidation of LA. Paths for oxygen transport are outlined in blue. The SLO-1 protein matrix is depicted in gray, LA in green, and the catalytic iron in magenta.

References

1. Schilstra, M. J., Veldink, G. A., Verhagen, J., and Vliegenthart, J. F. G. (1992) Effect of lipid hydroperoxide on lipoxygenase kinetics, *Biochemistry 31*, 7692–7699.
2. Schilstra, M. J., Veldink, G. A., and Vliegenthart, J. F. G. (1993) Kinetic analysis of the induction period in lipoxygenase catalysis, *Biochemistry 32*, 7686–7691.
3. Zheng, Y., and Brash, A. R. (2010) On the Role of Molecular Oxygen in Lipoxygenase Activation, *Journal of Biological Chemistry 285*, 39876–39887.
4. de Groot, J. J., Garssen, G. J., Veldink, G. A., Vliegenthart, J. F. G., and Boldingh, J. (1975) On the interaction of soybean lipoxygenase-1 and 13-L-hydroperoxylinoleic acid, involving yellow and purple coloured enzyme species., *FEBS Lett. 56*, 50–54.
5. Garssen, G. J., Vliegenthart, J. F. G., and Boldingh, J. (1971) An anaerobic reaction between lipoxygenase, linoleic acid and its hydroperoxides, *Biochemical Journal 122*, 327-332.
6. Garssen, G. J., Vliegenthart, J. F. G., and Boldingh, J. (1972) The origin and structures of dimeric fatty acids from the anaerobic reaction between soya-bean lipoxygenase, linoleic acid and its hydroperoxide, *Biochemical Journal 130*, 435-442.
7. Salzmann, U., Kuhn, H., Schewe, T., and Rapoport, S. M. (1984) Pentane formation during the anaerobic reactions of reticulocyte lipoxygenase, *Biochimica et Biophysica Acta (BBA) - Lipids and Lipid Metabolism 795*, 535–542.
8. Verhagen, J., Bouman, A. A., and Vliegenthart, J. F. G. (1977) Conversion of 9-d- and 13-l-hydroperoxylinoleic acids by soybean lipoxygenase-1 under anaerobic conditions, *Biochimica et Biophysica Acta (BBA) - Lipids and Lipid Metabolism 486,* 114-120.
9. Silverstein, R. M., Webster, F. X., and Kiemle, D. J. (2005) Spectrometric identification of organic compounds. *Wiley.*
10. Yu, Z., and Brash, A. R. (2003) The lipoxygenase gene ALOXE3 implicated in skin differentiation encodes a hydroperoxide isomerase, *Proceedings of the National Academy of Sciences 100*, 9162–9167.
11. Zheng, Y., and Brash, A. R. (2010) Dioxygenase Activity of Epidermal Lipoxygenase-3 Unveiled, *Journal of Biological Chemistry 285*, 39866–39875.
12. Chovancova, E., Pavelka, A., Benes, P., Strnad, O., Brezovsky, J., Kozlikova, B., Gora, A., Sustr, V., Klvana, M., Medek, P., Biedermannova, L., Sochor, J., and Damborský, J. (2012) CAVER 3.0: A Tool for the Analysis of Transport Pathways in Dynamic Protein Structures, *PLoS Comput. Biol. 8(10)*, e1002708.
13. Minor, W., Steczko, J., Boguslaw Stec, O., Otwinowski, Z., Bolin, J. T., Walter, R., and Axelrod, B. (1996) Crystal structure of soybean lipoxygenase L-1 at 1.4 Å resolution, *Biochemistry 35*, 10687–10701.
14. Knapp, M. J., Seebeck, F. P., and Klinman, J. P. (2001) Steric Control of Oxygenation Regiochemistry in Soybean Lipoxygenase-1, *J. Am. Chem. Soc. 123*, 2931–2932.
15. Knapp, M. J., and Klinman, J. P. (2003) Kinetic Studies of Oxygen Reactivity in Soybean Lipoxygenase-1, *Biochemistry 42*, 11466–11475.
16. Cohen, J., Olsen, K. W., and Schulten, K. (2008) Finding Gas Migration Pathways in Proteins Using Implicit Ligand Sampling, *Methods in Enzymology 437*, 439–457.